

Geometric Model Extraction from  
Magnetic Resonance Volume Data

Thesis by  
David H. Laidlaw

In Partial Fulfillment of the Requirements  
for the Degree of  
Doctor of Philosophy

California Institute of Technology  
Pasadena, California

1995

(Defended May 23, 1995)

Copyright © 1995  
David H. Laidlaw  
All Rights Reserved

# Acknowledgments

This work was supported in part by grants from Apple, DEC, Hewlett Packard, and IBM. Additional support was provided by NSF (ASC-89-20219) as part of the NSF/ARPA STC for Computer Graphics and Scientific Visualization, by the DOE (DE-FG03-92ER25134) as part of the Center for Research in Computational Biology, by the National Institute on Drug Abuse and the National Institute of Mental Health as part of the Human Brain Project, and by the Beckman Institute Foundation. All opinions, findings, conclusions, or recommendations expressed in this document are those of the author(s) and do not necessarily reflect the views of the sponsoring agencies.

Matthew Avalos has been instrumental in implementing large parts of this work. Without his dedication and incisive comments, this would have been smaller and taken a lot longer.

Thanks to Jose Jimenez for the late-night MR sessions and to Dr. Brian Ross for allowing scanning time at the Huntington Magnetic Resonance Center in Pasadena, where some of our data was collected.

I am grateful to Professor Alan Barr and his computer graphics group past and present: Cindy Ball, Ronen Barzel, Allen Corcoran, Carolyn Collins, Bena Currin, Dan Fain, Louise Foucher, Kurt Fleischer, Dave Kirk, Alf Mikula, Mark Montague, Preston Pfarner, John Snyder, Eric Winfree, Adam Woodbury, and Denis Zorin. The lab folks provided a great environment together with lots of collaborative help and advice.

My appreciation also goes to the MRI and Biology folks in the Beckman Institute at Caltech: Erik Ahrens, John Allman, Andres Collazo, Hanan Davidowitz, Dian De Sha, Michael Figdor, Mary Flowers, Scott Fraser, Pratik Ghosh, Russ Jacobs, Jim Narasimhan, Mark O'Dell, John Shih,

and Bill Trevarro. They provided me with many discussions of how MRI works and suggestions on how I ought to be doing things.

Thanks to the readers of early drafts for their patience, stamina and very helpful suggestions: Cindy Ball, Alan Barr, Ronen Barzel, Bena Currin, Dian De Sha, Dan Fain, David Kirk, Barbara Meier, and Preston Pfarner.

I also want to express my appreciation to Charles and Patricia Laidlaw, my parents, for their support and help throughout my time at Caltech.

And finally, thanks to my wife, Barbara Meier, for the moral and emotional support that helped me make it through this long and sometimes arduous journey.

# Abstract

This thesis presents a computational framework and new algorithms for creating geometric models and images of physical objects. Our framework combines magnetic resonance imaging (MRI) research with image processing and volume visualization. One focus is feedback of requirements from later stages of the framework to earlier ones.

Within the framework we measure physical objects yielding vector-valued MRI volume datasets. We process these datasets to identify different materials, and from the classified data we create images and geometric models. New algorithms developed within the framework include a goal-based technique for choosing MRI collection protocols and parameters and a family of Bayesian tissue-classification methods.

The goal-based data-collection technique chooses MRI protocols and parameters subject to specific goals for the collected data. Our goals are to make identification of different tissues possible with data collected in the shortest possible time. Our method compares results across different collection protocols, and is fast enough to use for steering the data-collection process.

Our new tissue-classification methods operate on small regions within a volume dataset, not directly on the sample points. We term these regions *voxels* and assume that each can contain a mixture of materials. The results of the classification step are tailored to make extraction of surface boundaries between solid object parts more accurate.

Another new algorithm directly renders deformed volume data produced, for example, by simulating the movement of a flexible body.

The computational framework for building geometric models allows computer graphics users

to more easily create models with internal structure and with a high level of detail. Applications exist in a variety of fields including computer graphics modeling, biological modeling, anatomical studies, medical diagnosis, CAD/CAM, robotics, and computer animation. We demonstrate the utility of the computational framework with a set of computer graphics images and models created from data.

# Contents

<i>Acknowledgments</i>	<i>iii</i>
<i>Abstract</i>	<i>v</i>
<i>Index of Figures</i>	<i>xi</i>
<i>Availability</i>	<i>xvi</i>
<b>1 Introduction</b>	<b>1</b>
1.1 Motivation . . . . .	1
1.2 Model-Building Framework . . . . .	2
1.2.1 Data Collection . . . . .	2
1.2.2 Tissue Classification . . . . .	5
1.2.3 Model Building and Visualization . . . . .	6
1.3 Overview . . . . .	7
<b>PART I. Data Collection</b>	<b>8</b>
<b>2 Goal-Based Data Collection</b>	<b>9</b>
2.1 Introduction . . . . .	11
2.1.1 Background and Motivation . . . . .	11
2.1.2 Related Work . . . . .	12
2.1.3 Terminology . . . . .	12
2.2 Conceptual Approach to Goal-Based Data Collection . . . . .	14
2.2.1 Optimization Framework . . . . .	15
2.2.2 Imaging Goals . . . . .	17
2.3 Mathematical Approach . . . . .	18
2.3.1 Model of the MRI Process . . . . .	19
2.3.2 Imaging Goals . . . . .	22
2.3.3 Solving the Constrained Optimization Problem . . . . .	24
2.4 Results . . . . .	25
2.4.1 Simulated Data . . . . .	25
2.4.2 Real Data: Mouse Embryo . . . . .	28
2.4.3 Real Data: Dungeness Crab . . . . .	31
2.5 Discussion . . . . .	35

2.5.1	Data Collected from Mouse Embryo . . . . .	36
2.5.2	Data Collected from Dungeness Crab . . . . .	37
2.5.3	MRI Material and Collection Model . . . . .	37
2.5.4	Choice of Protocol . . . . .	38
2.5.5	Choice of Contrast-to-Noise Ratio (CNR) . . . . .	39
2.5.6	Solver . . . . .	40
2.6	Conclusion . . . . .	41
<b>PART II. Bayesian Tissue Classification</b>		<b>42</b>
<b>3</b>	<b>Bayesian Tissue-Classification Framework</b>	<b>43</b>
3.1	Introduction . . . . .	45
3.1.1	Related Work . . . . .	45
3.1.2	Definitions . . . . .	45
3.2	A Framework for Solutions . . . . .	46
3.2.1	Bayesian Construction of Material Probabilities . . . . .	47
3.2.2	Classification . . . . .	51
3.2.3	Example of Classification Algorithm Construction . . . . .	51
3.3	A Family of Solutions . . . . .	53
3.3.1	Assumptions Common to New Algorithms . . . . .	53
3.3.2	Voxel-info: Histograms . . . . .	54
3.3.3	Overview of Algorithm A: Partial Volume Mixtures . . . . .	55
3.3.4	Overview of Algorithm B: Boundary Distance . . . . .	56
3.3.5	Overview of Algorithm C: Boundary Distance with Non-Uniform Material Signatures . . . . .	57
3.4	Summary . . . . .	58
<b>4</b>	<b>Bayesian Classification Algorithm A: Partial Volume Mixtures</b>	<b>59</b>
4.1	Construction . . . . .	60
4.1.1	Voxel-info . . . . .	61
4.1.2	Assumptions . . . . .	61
4.1.3	Sketch of Derivation . . . . .	62
4.2	Algorithm . . . . .	62
4.3	Normalized Histograms . . . . .	64
4.4	Histogram Basis Functions for Pure Materials and Mixtures . . . . .	66
4.5	Estimating Dataset Parameters . . . . .	67
4.6	Classification: Estimating Voxel Parameters . . . . .	68
4.7	Results . . . . .	69
4.8	Discussion . . . . .	71
4.9	Conclusion . . . . .	75
4.10	Derivation of Material PDFs . . . . .	75
4.10.1	Pure Materials . . . . .	76
4.10.2	Mixtures . . . . .	76
4.11	Derivation of Classification Parameter Estimation . . . . .	77
4.11.1	Definitions . . . . .	77
4.11.2	Optimization . . . . .	78



4.11.3	Derivation of the posterior probability $P(\alpha, c, s, \bar{N} h)$ . . . . .	78
<b>5</b>	<b>Bayesian Classification Algorithms B and C: Boundary Distance</b>	<b>82</b>
5.1	Assumptions . . . . .	83
5.2	Histogram Basis Functions . . . . .	84
5.3	Estimating Dataset Parameters . . . . .	86
5.3.1	Non-uniform Material Signatures . . . . .	87
5.4	Estimating Voxel Parameters . . . . .	87
5.5	Results . . . . .	88
5.6	Discussion . . . . .	90
5.7	Conclusion . . . . .	91
5.8	Detailed Derivations . . . . .	92
5.8.1	Pure Histogram Basis Function . . . . .	92
5.8.2	Mixture Histogram Basis Function . . . . .	92
5.8.3	Pure Material Parameter Estimation . . . . .	94
5.8.4	Material Mixture Parameter Estimation . . . . .	95
<b>PART III.</b>	<b>Applications</b>	<b>98</b>
<b>6</b>	<b>Model Building</b>	<b>99</b>
6.1	Taxonomy of Computer Graphics Models . . . . .	100
6.2	Modeling Examples . . . . .	101
6.2.1	Static Surface Models . . . . .	102
6.2.2	Static Volume Models . . . . .	105
6.2.3	Dynamic Models . . . . .	106
6.3	Conclusion . . . . .	109
<b>7</b>	<b>Deformed Volume Rendering</b>	<b>110</b>
7.1	Introduction . . . . .	110
7.1.1	Related Work . . . . .	111
7.1.2	Our Approach . . . . .	112
7.1.3	Overview . . . . .	113
7.2	Terms and Definitions . . . . .	113
7.2.1	Interval Methods . . . . .	113
7.2.2	Volume Rendering . . . . .	114
7.2.3	Deformations . . . . .	115
7.3	Algorithm . . . . .	116
7.3.1	Finding All Boundary Intersections . . . . .	118
7.3.2	Calculating the Path Through the Dataset . . . . .	120
7.3.3	Implementation Considerations . . . . .	120
7.4	Results . . . . .	122
7.5	Conclusion . . . . .	122
7.6	Derivation of Deformed Path . . . . .	123
<b>8</b>	<b>Conclusions and Future Work</b>	<b>125</b>
8.1	Conclusions . . . . .	125

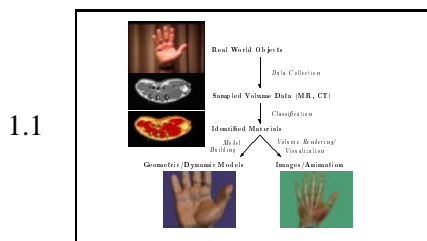
**Contents**

- 8.1.1 Goal-based Data Collection . . . . . 126
- 8.1.2 Bayesian Classification . . . . . 126
- 8.1.3 Model-Building and Visualization . . . . . 127
- 8.1.4 Interaction of Framework Stages . . . . . 127
- 8.2 Extensions . . . . . 128
  - 8.2.1 Goal-based Data Collection . . . . . 128
  - 8.2.2 Artifacts in MRI Data . . . . . 129
  - 8.2.3 Classification . . . . . 130
  - 8.2.4 Model Building and Simulation . . . . . 131
  - 8.2.5 Volume Rendering . . . . . 131
- 8.3 Summary . . . . . 132

**Bibliography**

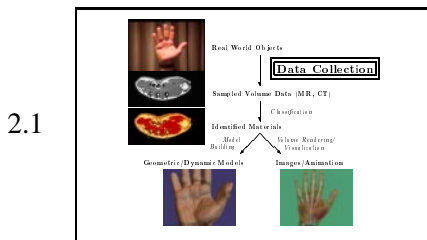
# Index of Figures

## Ch. 1. Introduction

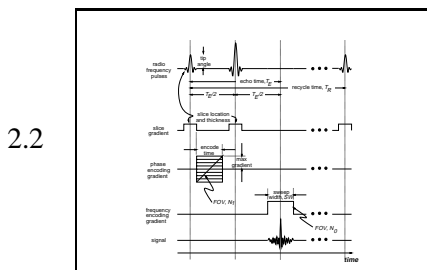


1.1 Geometric model building framework

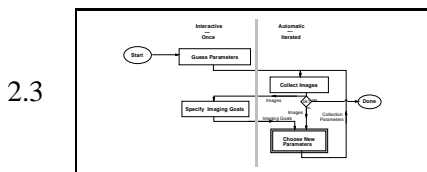
## Ch. 2. Goal-Based Data Collection



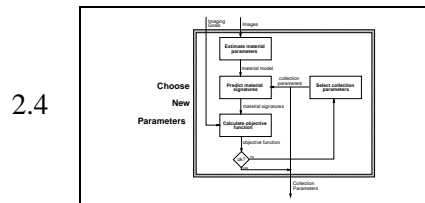
2.1 Goal-based collection context



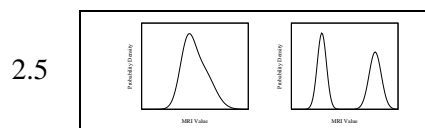
2.2 Pulse program



2.3 Data collection optimization process



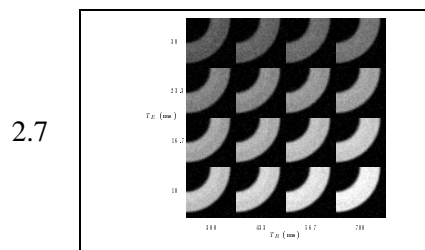
2.4 Data collection "inner loop"



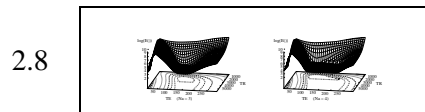
2.5 "Good enough" data



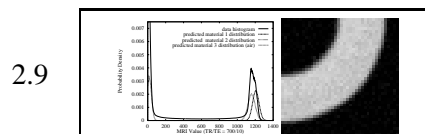
2.6 Shape of simulated data



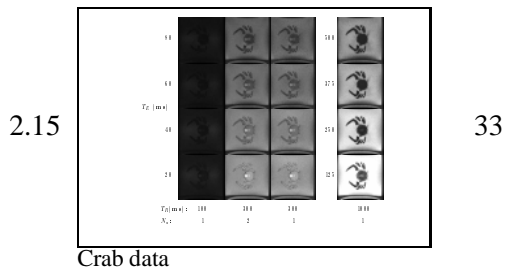
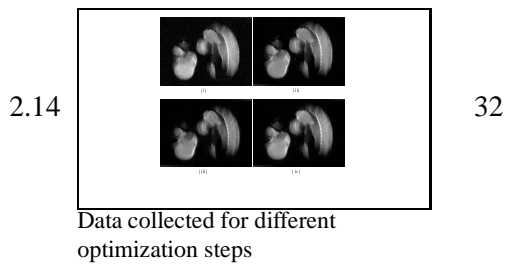
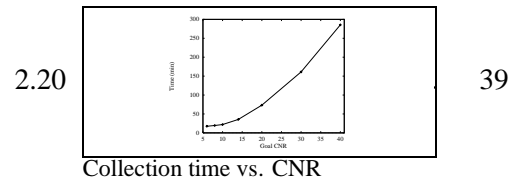
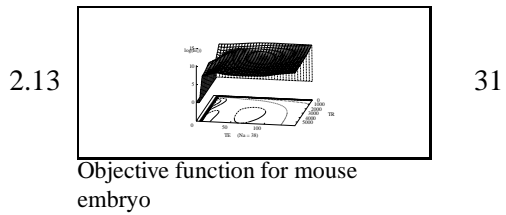
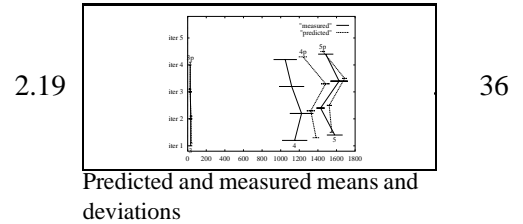
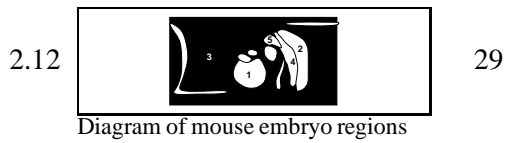
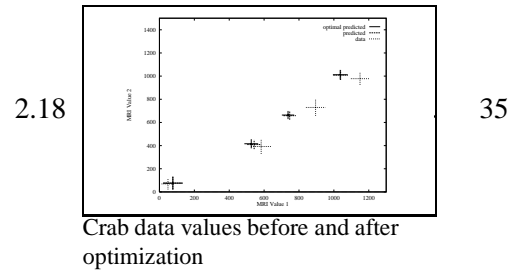
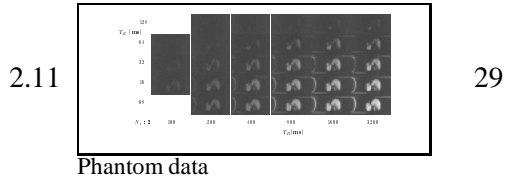
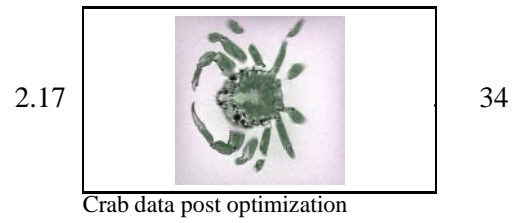
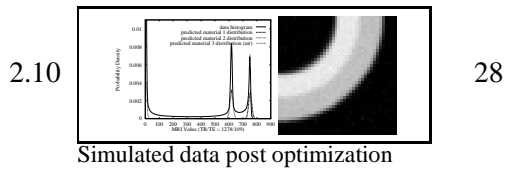
2.7 Simulated data



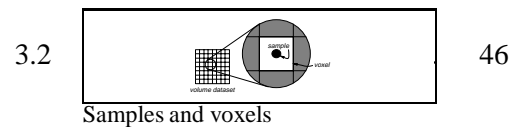
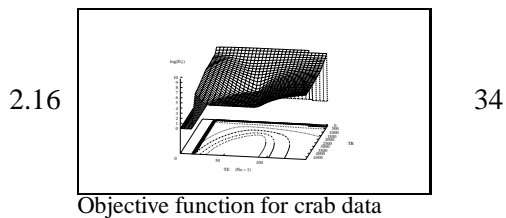
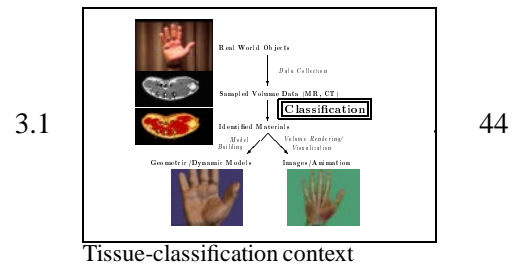
2.8 Objective function for simulated data

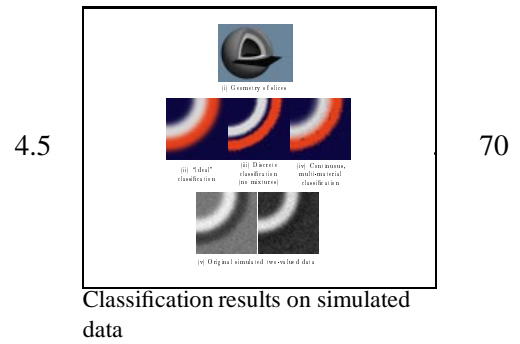
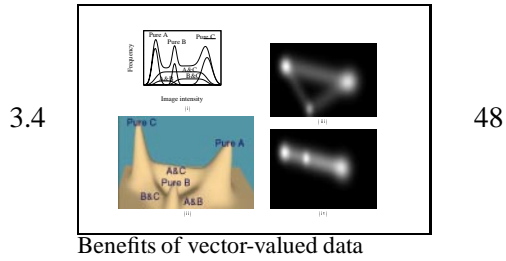
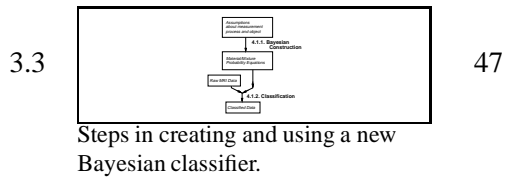


2.9 Simulated data before optimization

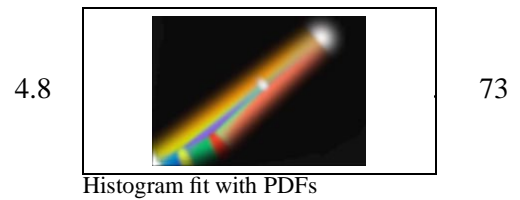
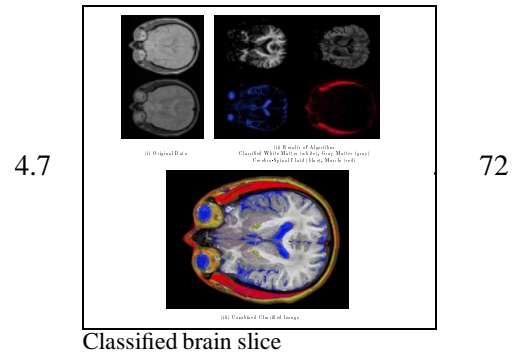
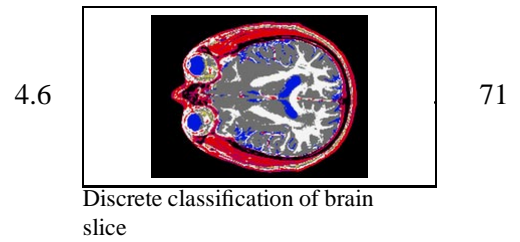
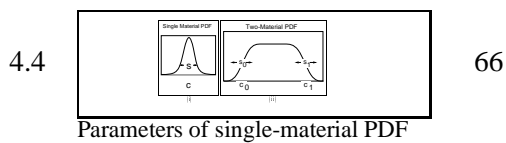
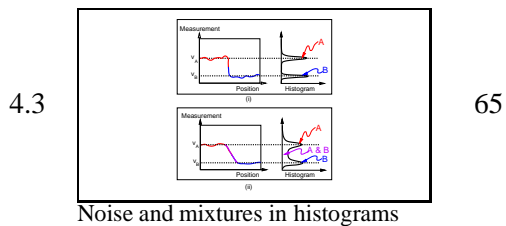
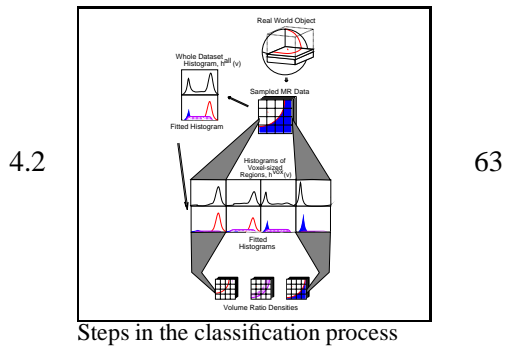
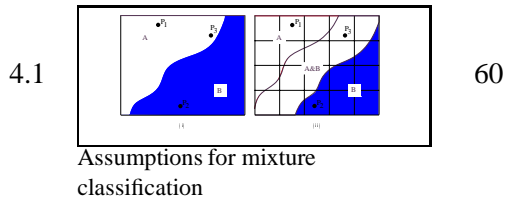


**Ch. 3. Bayesian Tissue-Classification Framework**

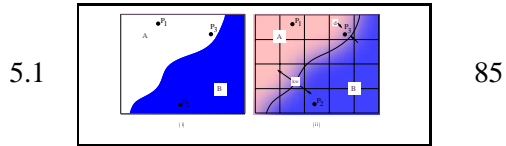




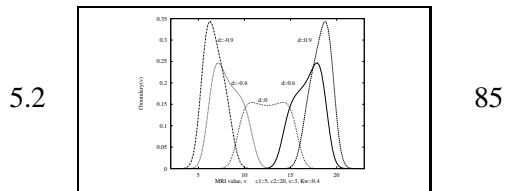
**Ch. 4. Bayesian Classification Algorithm A: Partial Volume Mixtures**



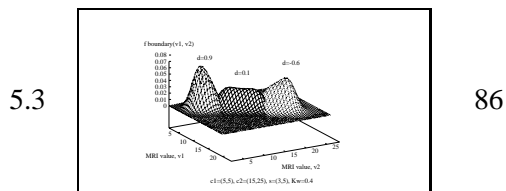
**Ch. 5. Bayesian Classification Algorithms B and C: Boundary Distance**



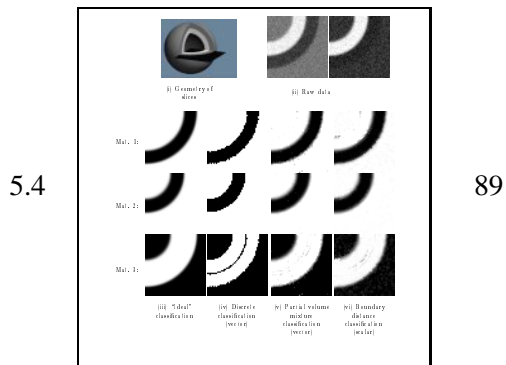
Assumptions for boundary distance classification



Boundary histogram basis functions

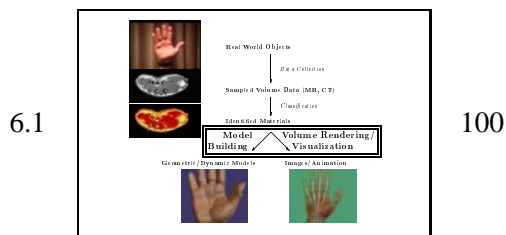


Boundary histogram basis function for vector-valued data

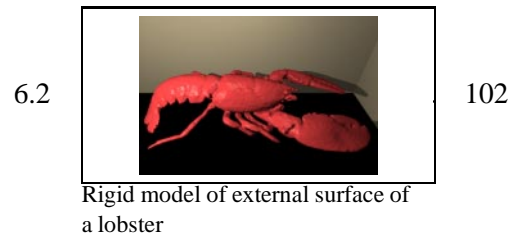


Classification results on simulated data

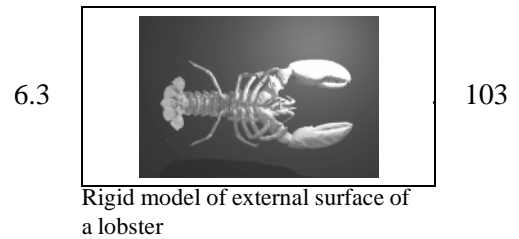
**Ch. 6. Model Building**



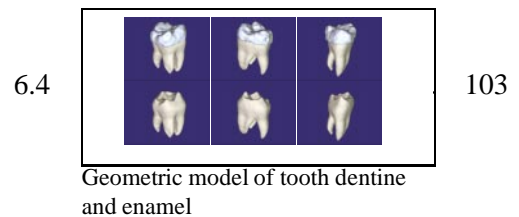
Model-building and visualization context



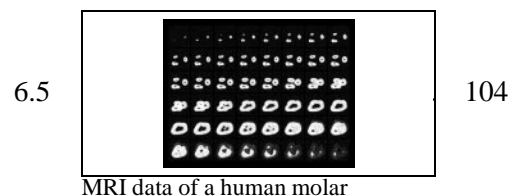
Rigid model of external surface of a lobster



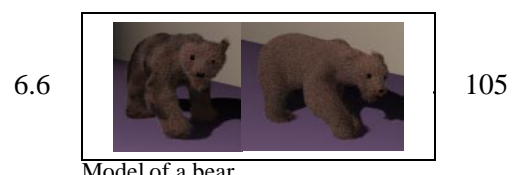
Rigid model of external surface of a lobster



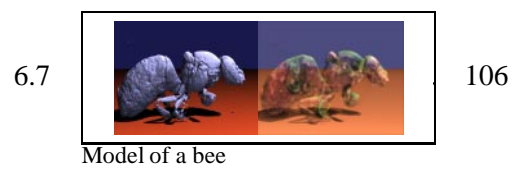
Geometric model of tooth dentine and enamel



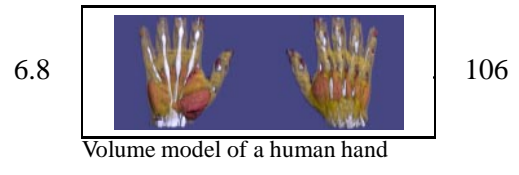
MRI data of a human molar



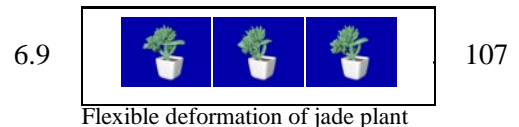
Model of a bear



Model of a bee




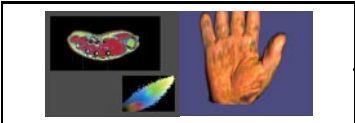
Volume model of a human hand




Flexible deformation of jade plant

6.10		107
	Flexible deformation of banana model	

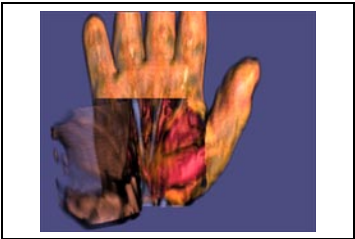
6.11		108
	Flexible deformation of human hand model	

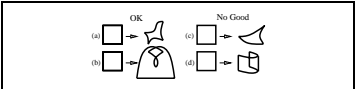
7.6		121
	Undeformed human hand	

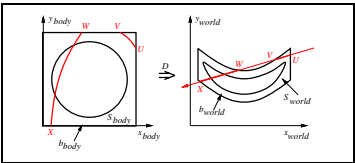
7.7		121
	Deformed jade plant	

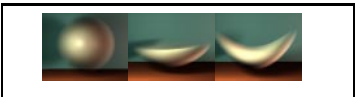
**Ch. 8. Conclusions and Future Work**

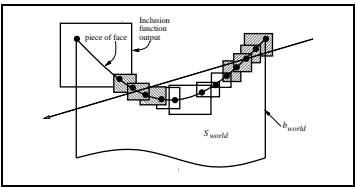
**Ch. 7. Deformed Volume Rendering**

7.1		111
	Skin-peeling deformation volume-rendered	

7.2		115
	Two-dimensional examples of deformations	

7.3		117
	Example of 2-D deformation	

7.4		117
	Three deformations of a sphere	

7.5		118
	Inclusion functions	

# Availability

Paper copies of this thesis are available by U.S. mail to:

Computer Science Library  
Caltech M/S 256-80  
Pasadena, CA 91125

The library also maintains an online version on the World Wide Web. The URL of the index of available technical reports is:

<file://cs.caltech.edu/tr/INDEX.html>

Many of the images are also online. Start at my home page:

<http://www.gg.caltech.edu/~dhl/phd.html>

I can be reached via e-mail to [dhl@druggist.gg.caltech.edu](mailto:dhl@druggist.gg.caltech.edu).



# Chapter 1

---

## Introduction

---

### 1.1 Motivation

Computer graphics is a broad field. Its practitioners gather within it any domain in which images are generated or enhanced by a computer. One thrust within computer graphics is the creation of models and images of objects such as plants or animals to further our understanding of them. The same types of models and images also have applications in entertainment and education.

Our work explores some new techniques for studying anatomy, development, and behavior through this modeling and rendering process. Given a locust, a human hand, or a frog embryo, how can we visualize and understand it? What new tools are needed to answer questions about it?

We present a computational framework for attacking some of the difficulties in making models and images. Our framework is centered around measuring objects, identifying different regions within the objects, and creating images and models using information about the regions and measurements.

The framework is not a one-way pipeline. Instead, each stage requires input with certain

characteristics; these required characteristics impact the output of earlier stages. The feedback assures that the output from each stage meets the requirements for input to the next.

In this chapter we present our computational framework, discuss some of the novel techniques that we have developed within the framework, and give an overview of the remaining chapters.

## 1.2 Model-Building Framework

Our framework consists of three main stages, illustrated in Figure 1.1. In the first stage, *data collection and processing*, real-world objects are measured and the resulting sampled volume data processed and stored for later stages. We describe some of the problems and our approaches to solving them in Section 1.2.1 and in Chapter 2.

The second stage of the framework, *classification*, identifies regions containing different materials within the objects we have measured. The sampled volume data is used as input. Section 1.2.2 and Chapter 3 describe our Bayesian methodology for generating classification algorithms, and Chapters 4 and 5 present three new algorithms.

The third stage of the framework, *model building and visualization*, generates models, images, and animations of our objects. We outline some of the challenges and show results of applying our techniques to classified MRI data in Section 1.2.3 and in Chapters 6 and 7.

### 1.2.1 Data Collection

In the first stage of our computational framework we measure the physical object we wish to model. The data we collect must distinguish different materials sufficiently for our classification and model-extraction processes to work. We have developed techniques that help us to collect data that satisfies our imaging goals in a minimal amount of time.

**Why MRI?** We have chosen to use magnetic resonance imaging (MRI) for a number of reasons. First, MRI measures information about both the inside and the outside of an object. The resulting

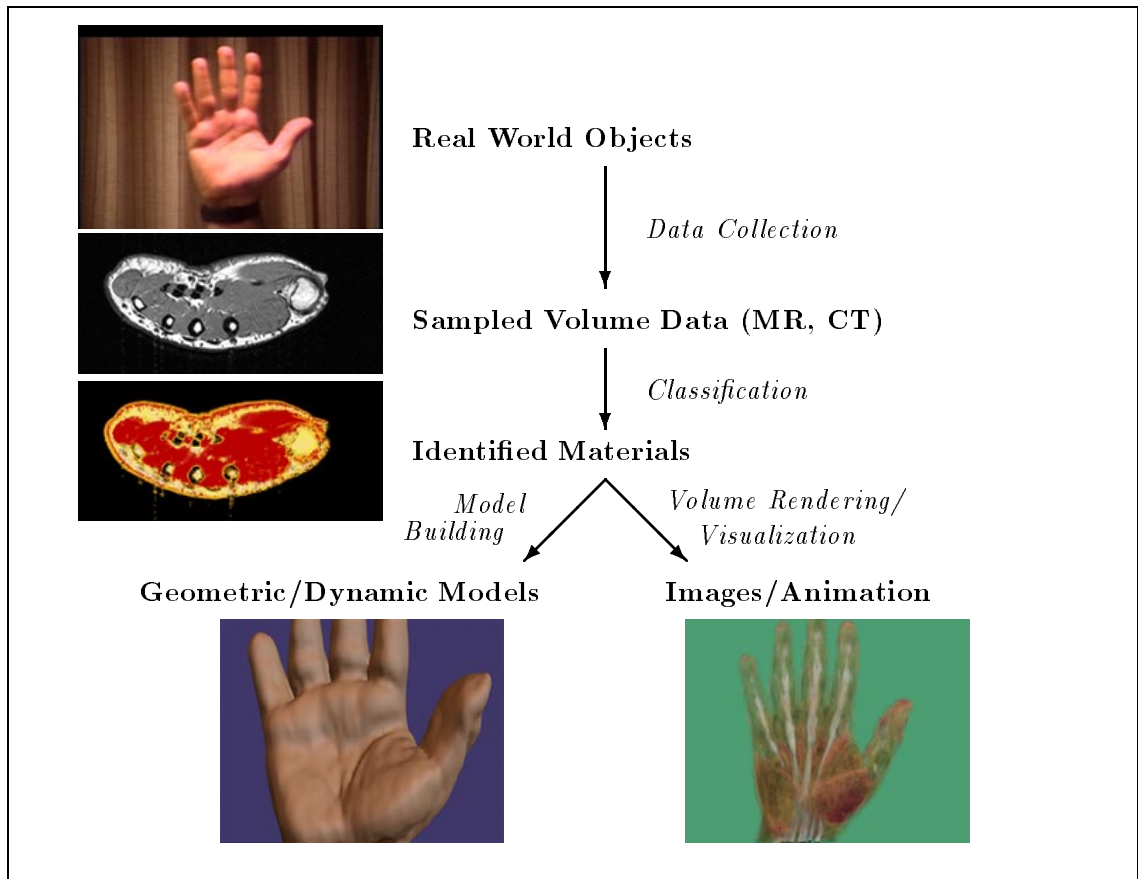


Figure 1.1: This figure shows the computational framework that we use for creating static and dynamic geometric models from MRI data. □

volume data identify internal structure, an important factor in the behavior of dynamic models. Second, MRI measures at least three independent parameters of each material, and so has the potential to distinguish more different materials than techniques that measure only a single parameter. Third, it is not invasive, so we can measure living plants and animals without damaging them. Fourth, although imaging time is expensive, MRI is accessible at most large hospitals and at imaging centers.

Other modalities have been used for creating models. Laser range-scanning is the most widespread [Turk and Levoy, 1994] primarily due to its low cost and high level of detail. It is, however, limited to line-of-sight surface measurements, which are sufficient for many static computer graphics applications, but not sufficient for applications requiring internal structure or for dynamic models where an initially invisible portion of the surface may become visible.

Computed tomography (CT) data have also been used for similar purposes [Drebin et al., 1988]. CT can produce higher-resolution data than MRI and measures internal structure, but suffers from two drawbacks. First, it uses ionizing x-radiation, which damages living tissues; and second, its measurements depend only on a single material parameter, and so cannot differentiate tissues as well as MRI.

**Limitations.** MRI datasets have a number of limitations. There are many different MRI methods or *protocols* for collecting data, each with a set of parameters that influence how different materials appear in the resulting images. Choosing a protocol and parameters from this panoply is a formidable task, often requiring years of experience and frequently only moderately successful. Further complicating the problem, MRI collections are time-limited by the physics of the spinning hydrogen nuclei; datasets with a large enough signal-to-noise ratio or contrast-to-noise ratio often require a prohibitive amount of time to collect.

There are also many distortions that can appear in MRI data. Broadly, the distortions can be categorized as geometry or intensity related. We avoid some of the distortions by constraining the data-collection process and reduce others through the parameter optimization process. In a post-collection step we reduce even more through image-processing techniques. We defer attending to some of the distortions until the tissue-classification stage where we diminish the artifacts through new classification algorithms.

Cost and accessibility are additional issues. While MRI machines exist in most large hospitals and in imaging centers in many large cities, they are expensive to use, currently costing around \$400-1000/hour, and often difficult to access.

**MRI Data Collection Parameter Setting.** As we describe in more detail in Section 2.1.2, others have attacked the MRI parameter-setting problem with techniques that optimize the contrast between two specific materials or that find closed-form solutions for a specific protocol. Some numerical techniques have also been used to optimize the contrast-to-noise ratio for a particular collection

algorithm.

In Chapter 2 we directly address the parameter-setting and collection-time problems by codifying the requirements of the classification, model-building, and visualization algorithms; the complex constraints of the MRI machines; and the desire to reduce collection time. From the requirements we construct a mathematical optimization problem that we solve numerically to find collection parameters that collect data satisfying our requirements in the shortest possible time.

### **1.2.2 Tissue Classification**

The second stage in our computational framework involves classifying or segmenting our sampled datasets to identify regions of different materials within the datasets. The main motivation for our classification work is to make computer graphics models and images using volume measurements of physical objects. Identifying different materials is a key step in the process, particularly when different materials have different behaviors or appearances. Computer graphics applications include volume-rendered images [Levoy, 1988], surface models [Lorensen and Cline, 1987], and volume models created from the data.

Applications of the models and images include surgical planning and assistance, conventional computer animation, anatomical studies, and predictive modeling of complex biological shapes and behavior. Some aspects of our classification techniques could also be applied to medical diagnosis. With further development, the concepts may also apply to computer vision problems or to extracting mattes for digital optical effects.

Sources of sampled volume data are becoming more numerous and accessible. In addition to MRI, they include Computed Tomography (CT), as well as astrophysical, meteorological, and geophysical measurements. The computational sciences frequently produce sampled output, e.g., the results of computational fluid dynamics (CFD) and finite element method (FEM) simulations. We have focused on classifying MRI data, but our techniques apply to other modalities as well.

We describe related classification work in Section 3.1.1. In some of this work classification is implemented via interactively selected mappings from data values to colors and opacities, which

are then rendered, or via interactively chosen threshold values for distinguishing regions. Many more rigorous classification algorithms have also been developed, but are of limited applicability to classifying sampled MRI data for extracting models.

**Bayesian Framework.** We have developed a methodology (see Chapter 3) for constructing a Bayesian classification algorithm from a set of assumptions about the underlying data. Our algorithms start with the premise that the sampled datasets satisfy the Nyquist sampling theorem, which allows us to reconstruct a continuous function  $\rho(x)$  over the entire dataset [Oppenheim et al., 1983]. We calculate histograms of  $\rho(x)$  over small regions of the dataset and classify those histograms by fitting histogram basis functions constructed from the set of assumptions.

**Classification Algorithms.** Using the Bayesian framework we have constructed three different classification algorithms, described in more detail in Chapters 4 and 5. The first algorithm models each voxel as a linear combination of pure materials and mixtures of two materials. The second algorithm models each voxel as either entirely composed of a single pure material, or composed of a mixture between two materials with a boundary between those two materials. The third algorithm is substantially similar to the second, but allows the expected value, or signature, of each material to vary over a dataset, a common characteristic of MRI data. These techniques classify MRI data better than previously available techniques because they use a more accurate model of the collected data. They are also tailored to produce accurate results near boundaries between materials where extracted model details are most visible.

### 1.2.3 Model Building and Visualization

The final stage in our computational framework involves extracting geometric and dynamic models and visualizing the results. We describe this work in Chapters 6 and 7. We have primarily experimented with applying existing techniques to the data that we have collected and classified. Using these techniques we have created a series of models and images of inanimate and animate

objects measured with MRI. These examples illustrate our taxonomy of model types and show the utility of classified MRI data as a method for creating models.

Many of the models that we have created are polygonal isosurfaces of sampled functions created by classifying collected datasets. In addition to creating static models of these regions of uniform materials, we have used the regions to define behaviors and calculated rudimentary simulations of the motion of these models. The behaviors are implemented as time-varying deformations. The classified datasets also comprise a model of the underlying object; we can directly visualize them, and, in some cases, directly simulate the behavior of the model.

Our visualizations take two basic forms, surface rendering and volume rendering. Most traditional computer graphics imagery is rendered as surfaces, although in the last decade volume rendering has emerged as a useful adjunct to the more traditional techniques. Unlike surface-rendering methods, volume rendering produces images that can show internal structure. The images of solid objects appear to consist of volumes of transparent or semi-transparent material.

We render static and moving images using both techniques. We have developed an extension to volume-rendering algorithms that are based on ray tracing. Our extension directly renders deformed volume data.

### **1.3 Overview**

We present the computational framework shown in Figure 1.1 from top to bottom. Chapter 2 describes the data collection stage. Chapter 3 explains the Bayesian methodology for creating classification algorithms, with the new algorithms described in Chapters 4 and 5. The third stage, model extraction and visualization, is illustrated in Chapters 6 and 7.

# **PART I**

## **Data Collection**

The following part of the thesis describes goal-based data collection, a technique for choosing a specific MRI collection technique and specific collection parameters from the myriad of possibilities. The choice is guided by a series of goals for the resulting volume data and the collection process.



## Chapter 2

---

# Goal-Based Data Collection

---

As shown in Figure 2.1, the first computational step in our framework is collecting data that measures an object that we wish to model. We have chosen to use Magnetic Resonance Imaging (MRI) as our measurement technique for reasons explained in Chapter 1. There are several challenges, however, that MRI presents in the context of creating models.

Two of the main challenges are choosing among the many collection techniques, or *protocols*, and selecting values for the collection parameters that control each protocol. Our approach is to define imaging goals for the collection process, translate them into a constrained optimization problem, and find the protocol and collection parameters that best satisfy the imaging goals.

The novel contributions of our work are in our goal-based framework, in the choice of imaging goals for the optimization procedure, in the use of the optimization step to steer the acquisition process, and in our two-level optimization process. The framework gives a methodology for adding new imaging goals and new collection techniques to the set that we have implemented. The imaging goals we implemented are motivated by our desire to distinguish adjacent materials sufficiently well to be able to produce geometric models from the data, but many of the objectives are generally

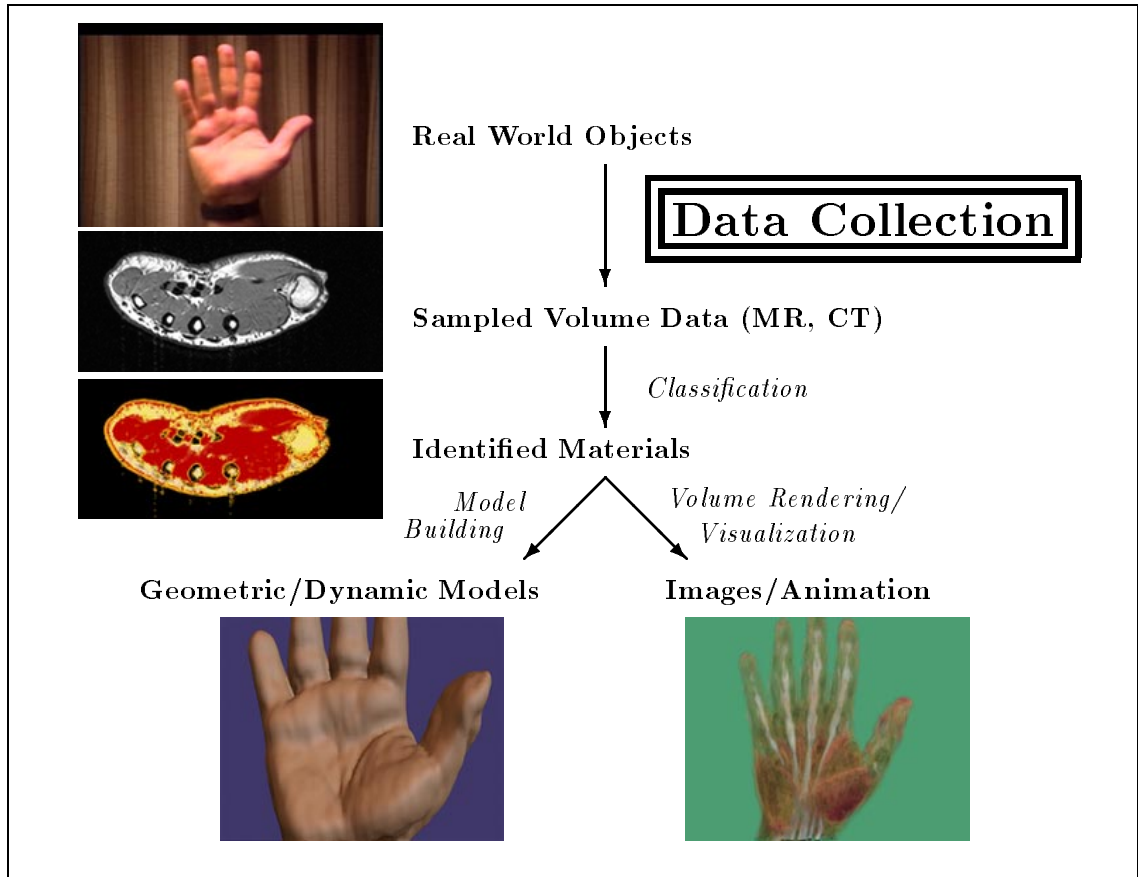


Figure 2.1: Our computational framework for creating geometric models, as shown earlier in Figure 1.1. In Chapter 2 we describe our goal-based data-collection process, emphasized in the diagram. Our new techniques help select an optimal collection technique and set of collection parameters given a set of imaging goals for the resulting volume data. □

applicable to imaging applications. These imaging goals differ from other work in that they do not find collection parameters yielding the most contrast or highest contrast-to-noise ratio (CNR), but rather find parameters yielding *sufficient* contrast in the least amount of time. Also, any number of materials can be specified by a user from a low-resolution dataset, and optimal parameters are generated taking into account inherent machine limitations and desired collection parameters such as resolution. Finally, because units of the function we optimize are consistent from protocol to protocol, we can choose the most appropriate technique or combination of techniques. We can even choose between collections that produce scalar or vector-valued data.

We validate our technique with results using simulated as well as real MRI data.

The chapter is organized as follows: Section 2.1.1 discusses the collection of MRI data and

motivates the need for goal-based collection techniques. Section 2.1.2 describes related work in the area and compares it to our work. We define terms in Section 2.1.3. In Section 2.2 we describe our imaging goals and give a conceptual description of the optimization process. A mathematical description follows in Section 2.3 with results, discussion, and conclusions in Sections 2.4–2.6.

## **2.1 Introduction**

### **2.1.1 Background and Motivation**

Collecting good MRI data is difficult because imaging systems are very sensitive to the many parameters of the various collection techniques, to the choice of technique, to subtle differences in the materials that are being imaged, and to the fine tuning of the machine being used. Many parts of the process are also inherently analog and difficult to calibrate.

MRI collection protocols are defined by a set of precisely timed electro-magnetic pulses applied to an object. A “pulse program” defines and controls the exact timing. Figure 2.2 shows an example. In these programs many operations occur simultaneously: different magnetic gradients are turned on and off, and radio frequency energy is transmitted into the subject and is measured as it is re-radiated. The timing of these operations changes the resulting images that are collected, and it is often difficult to choose appropriate parameter values to collect data that have the properties needed for a given application.

In most cases finding an appropriate set of parameters is a trial-and-error process. An experimenter typically collects datasets varying the parameters based on prior experience or published results of other experiments until the images appear reasonably good.

We have improved on this trial-and-error process by mathematically formulating a set of imaging goals and using constrained optimization to find an optimal set of collection parameters.

Collection Parameters, $P_c$		units	
$N_0, N_1, N_2$	samples	none	number of samples in each direction— $N_0$ is often called the read direction; $N_1$ , the phase-encode direction; and $N_2$ , the slice direction
$FOV_0, FOV_1, FOV_2$	field of view	[m]	size of imaged region in each of the above directions
$H$	slice thickness	[m]	
$N_a$	averages	none	number of acquisitions averaged together in each sample
$T_R$	recycle time	[s]	time between acquisitions of data for spins to realign with the static magnetic field
$T_E$	echo time	[s]	time within an acquisition for spins to de-phase due to $T_2$ effects
$T_I$	inversion time	[s]	time within an acquisition for spins to decay due to $T_1$ effects
$\alpha$	tip angle	degree	angle spins are tipped away from the static magnetic field
$DW$	dwelt time	[s]	time to collect a single data point

Table 2.1: The collection parameters in this table control collection protocols, describing the volume to be imaged, the number of samples within that volume, and the timing of the pulses that influence contrast between materials.  $\square$

### 2.1.2 Related Work

Many efforts to find effective MRI collection parameters have centered around finding optimal contrast between two specific materials, e.g., white matter and grey matter in the human brain [Dufour et al., 1993]. Other approaches have derived closed-form solutions for optimizing contrast, contrast-to-noise ratio, or sensitivity [Mitchell et al., 1984] [Fox and Henson, 1986] [Pelc, 1993] [Hendrick et al., 1984]. Numerical methods have also been employed successfully, most commonly to optimize the contrast-to-noise ratio, sometimes for a specific collection time [Dreher and Bornert, 1988] [Dufour et al., 1993] [Epstein et al., 1994].

### 2.1.3 Terminology

We define terms here that we will use throughout the chapter.

An *imaging goal* describes a desired property of collected data or of the collection process. An imaging goal can also be a *constraint* on a collection parameter or among several parameters. The

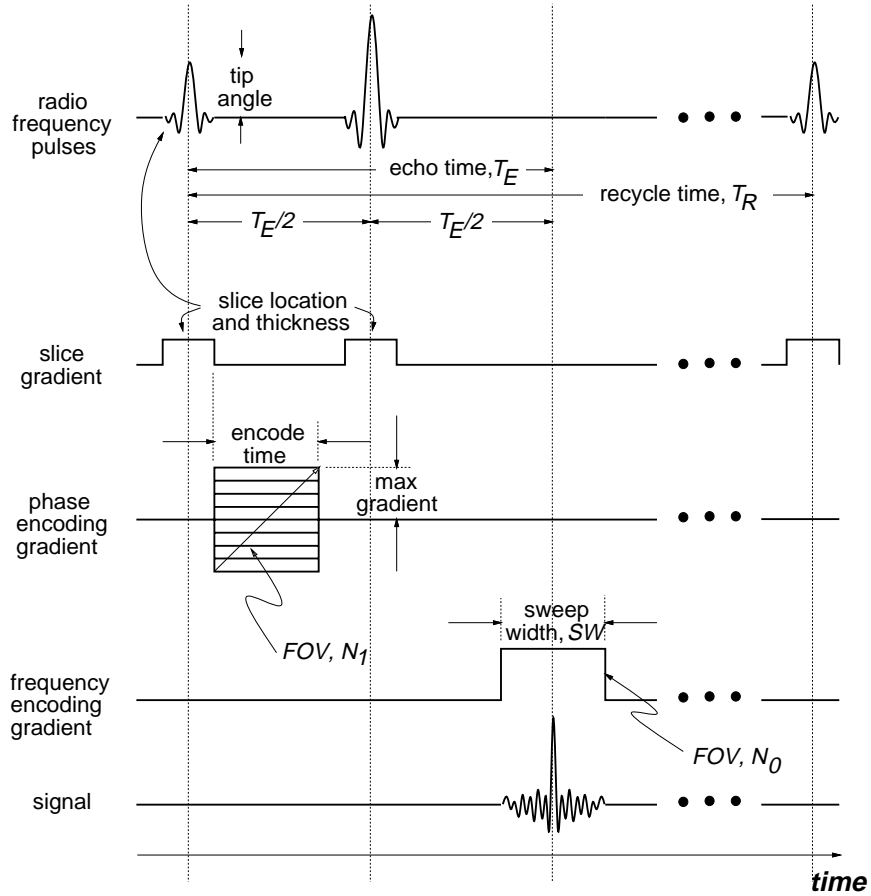


Figure 2.2: Pulse programs describe how various components of an MRI machine all execute in parallel. In this prototypical diagram of the *spin-echo* protocol, each horizontal plot represents the activity of one portion of the machine as time moves to the right. As the pulses execute they perturb spinning hydrogen nuclei, change their phase, and measure information about them. There are many parameters that control these programs; some control the spatial region to be imaged (slice location and thickness, and field of view,  $FOV$ ), the number of of samples over that region ( $N_0$  and  $N_1$ ), and the timing of the pulses that influence contrast between materials (echo time,  $T_E$ , and recycle time,  $T_R$ ). As long as certain relationships between parameters are maintained, other parameters, such as sweep width and encode time, can be varied to avoid machine settings that are not possible. Choosing appropriate values is a difficult process. The diagram shows pulses to acquire a single 1-D array of data; for a 2-D image or 3-D volume the acquisition is repeated.  $\square$

constraint may encode a hardware limitation or some relationship among parameters.

A *protocol* is an MRI collection technique. Each protocol is implemented by a *pulse program* with parameters that control the location and resolution of the data collected, as well as the timing of the pulses that influence contrast and noise within the collected data. The set of parameters is collectively known as *collection parameters*, or  $P_c$ .

Material Parameters, $P_m$		units	
$N(^1H)$	spin density	$[m^{-3}]$	number of hydrogen nuclei per volume
$T_1$	longitudinal relaxation time	[s]	time constant for perturbed spins to return to alignment with the static magnetic field
$T_2$	transverse relaxation time	[s]	time constant for a collection of spins to go out of phase

Table 2.2: The three material parameters describe how a region of uniform material will behave under the influence of an MRI collection protocol. The parameters are based on a model of the behavior known as the Bloch equations [Bloch, 1948]. □

*Spin-echo* is an example of a protocol with the contrast-related parameters  $T_R$ ,  $T_E$ , and  $\alpha$ .

Table 2.1 lists collection parameters; Figure 2.2 shows a prototypical diagram of a spin-echo pulse program.

A *machine* is an instance of an MRI machine. Because different MRI machines have hardware with different capabilities, imaging goals are sometimes implemented differently for different machines.

Table 2.2 lists *material parameters* for a model of the MRI process. Material parameters, sometimes referred to as  $P_m$ , describe how a region of homogeneous material behaves as a pulse program collects data. The parameters include the density of hydrogen nuclei,  $N(^1H)$ , and two exponential time-constants,  $T_1$  and  $T_2$ , that describe the behavior of the nuclei. The behavior is based on the Bloch equations [Bloch, 1948], a set of coupled differential equations describing the behavior of spinning nuclei in time-dependent magnetic fields. Each material has its own material parameters. The *signature* for a material is the expected value and standard deviation of measurements of that material for a given set of protocol parameters.

In many of our results we list the mean,  $\mu$ , and standard deviation,  $\sigma$ , of a normal distribution with the notation “ $\mu \pm \sigma$ .”

## 2.2 Conceptual Approach to Goal-Based Data Collection

Our approach builds on the related numerical optimization work (see Section 2.1.2), but uses a more general goal-based approach and a set of imaging goals that are applicable to more situations.

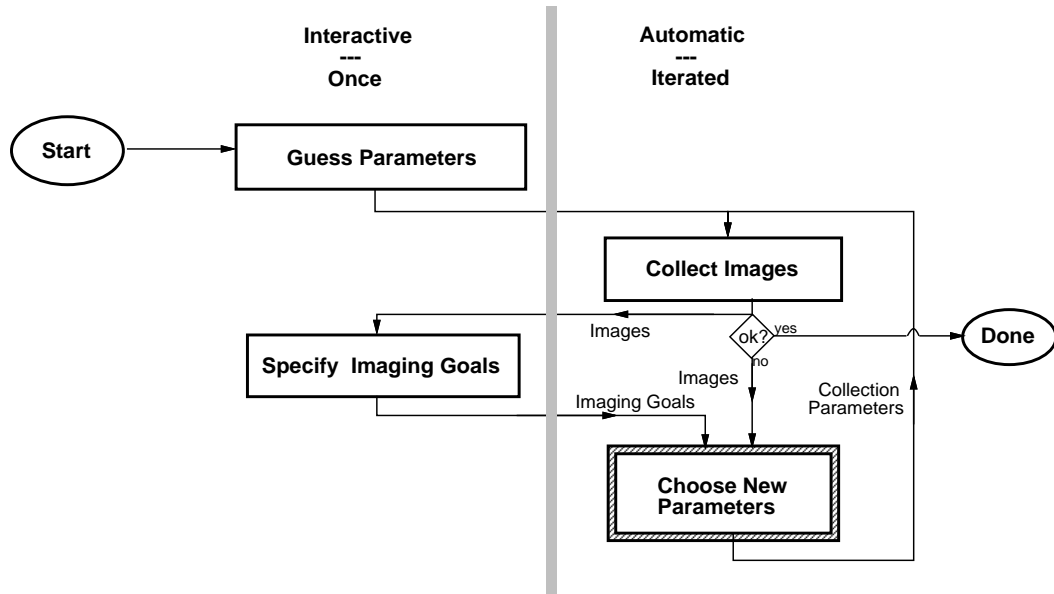


Figure 2.3: The outer-level optimization process in the data collection parameter optimization process. The process begins at the left with a guess at collection parameters. Datasets are collected with those parameters, and a set of imaging goals specified, some through interaction with the data. The algorithm then iteratively chooses parameters that satisfy the goals and collects new data. Figure 2.4 details the inner-level optimization process of choosing new parameters. □

New imaging goals and protocols can be added to our framework in an object-oriented manner, and optimal solutions for each protocol can be compared to optimal solutions for other protocols.

In this section we first describe the framework for our optimization process and then present the set of imaging goals implied by our modeling application.

### 2.2.1 Optimization Framework

The goal-based framework defines an objective function,  $E(p)$ , of the collection parameters and a set of constraints. Through evaluations of  $E(p)$  we can computationally find an optimal set of parameters.

Ideally, the constrained optimization process would collect a dataset each time it wanted to evaluate a new set of parameters. Unfortunately, the data-collection process is quite slow, and the constrained optimization process evaluates  $E(p)$  for many sets of parameters. To address this problem we have developed a two-level optimization process. At the outer level, datasets are collected, but at the inner level the data-collection process is simulated. Figure 2.3 shows the outer

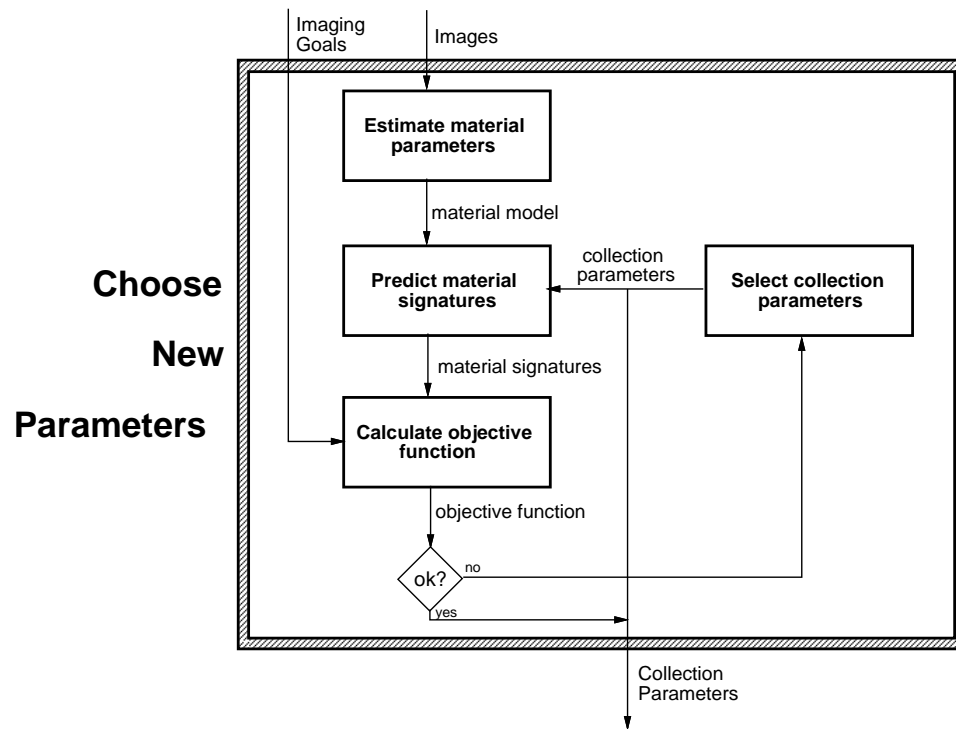


Figure 2.4: The data collection optimization “inner loop.” This process takes a set of imaging goals and a set of images and calculates collection parameters that satisfy the goals. A model for each material is first fit to the set of images, and then a constrained optimizer iteratively finds the optimal set of protocol parameters based on the material parameters. □

level. The “Choose New Parameters” step contains the inner level, which is shown in more detail in Figure 2.4.

In collecting optimized data we perform the steps shown in Figure 2.3. First, we choose an initial range of collection parameters for the optimization process to use as a starting point. We collect several datasets with these parameter settings, and then choose geometric locations within the images that represent different tissues. We then specify a set of imaging goals, e.g.,

- differentiate chosen materials
- acquire data at a particular resolution and size
- minimize collection time
- do not violate hardware limitations of the machine

As shown in Figure 2.4 the constrained optimizer finds an optimal set of parameters based on a



model of each material that we identified in the collected data. New datasets are collected near that optimal point. Frequently they satisfy the imaging goals, but when they do not, the outer level of the optimization process is repeated and more new data are collected.

### 2.2.2 Imaging Goals

We use several different types of imaging goals in our optimization process. Some are related to the ultimate use of the collected data, some are inferred from constraints of the collection protocol or machine, and some are practical.

#### **Goal: Good Tissue Discrimination**

Our first imaging goal is to be able to unambiguously identify different tissues within an image. The specific requirements from this goal arise from the tissue-classification algorithms that we present in Chapters 3–5.

There are two parts to the goal: the first is related to the contrast-to-noise ratio (CNR) [Kanal and Wehrli, 1986]. We assume that measurements of a particular material will be normally distributed. We can calculate the mean and standard deviation of the normal distribution for each material from the interactively selected points. From the selected points, the CNR, which is the ratio of the difference of their means to the average of their standard deviations, can be calculated for each pair of materials. For materials with a CNR of less than one, the normal distributions overlap and are difficult to distinguish. For larger CNR values the distributions overlap less and become easier to identify, as shown in Figure 2.5. The degree of overlap that is acceptable is determined by our tissue segmentation method.

The second part of the goal is to collect data at a particular resolution. As we formalize the imaging goals in a Section 2.3, we incorporate resolution. By fixing the desired resolution, we find collection parameters that achieve sufficient contrast to identify materials at that resolution.

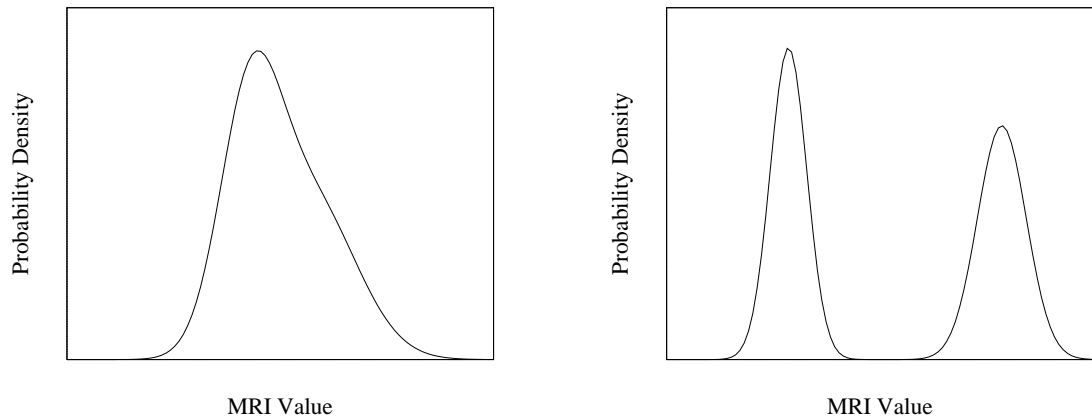


Figure 2.5: On the left two summed normal distributions are difficult to identify, and data values do not clearly lie under either, making them difficult to assign to a material. On the right the distributions are clearly separated. Note that this separation can be achieved either by moving the centers or by narrowing the widths of the distributions. Figures 2.9 and 2.10 show examples of data that illustrate this effect.  $\square$

### Goal: Observe Machine and Protocol Limitations

We also wish to avoid violating assumptions implied by an imaging protocol or by limitations of our collection hardware. For example, a given implementation of a spin-echo imaging protocol will have a maximum value for the parameter  $T_E$  that is dependent on the value for  $T_R$ . Similarly, a given implementation on a particular machine will have a minimum value for  $T_R$ . The minimum may be a function of other parameters, or may be an absolute value.

### Goal: Minimize Collection Time

We wish to achieve the imaging goals above with the smallest amount of collection time. Imaging time is expensive, so reducing it saves money. Shorter imaging times also tend to reduce the likelihood of motion artifacts from living subjects because they do not need to remain in the machine and motionless for as long.

## 2.3 Mathematical Approach

In this section we mathematically formulate our imaging goals and the MRI model, describe how we construct an optimization problem from them, and give some details about the numerical solution

technique that we use.

As shown in Figures 2.3 and 2.4, our algorithm iterates the following steps:

- collect data
- estimate material parameters from data
- optimize collection parameters from MRI model

### 2.3.1 Model of the MRI Process

The inner loop of our optimization process requires the prediction of material signatures for a given set of collection parameters. We model the MRI process to do this.

In the model we have chosen [Farrar and Becker, 1971], each material has three parameters,  $N(^1H)$ ,  $T_1$ , and  $T_2$ . These parameters are proton spin density, a longitudinal relaxation-time constant and a transverse relaxation time constant (see Table 2.2). The parameters are defined in the Bloch equations [Bloch, 1948].

We define three functions that characterize each protocol that we support. We describe them below. New protocols are added to our framework in an object-oriented manner by specifying these three functions. The first function,  $v(P_c, P_m)$ , specifies the data value expected for a given set of material parameters and collection parameters. The second function,  $\sigma(P_c, P_m)$ , gives a model of the standard deviation of the data value as a function of the material and collection parameters. The third function,  $t(P_c)$ , defines the collection time necessary to collect data using the collection parameters.

From data collected with a variety of collection parameters, we estimate the unknown material parameters for each material,  $N(^1H)$ ,  $T_1$ , and  $T_2$ , as well as any unknown collection parameters defined below.

In the estimation procedure we first interactively select locations representing a specific material within several datasets collected with different collection parameters. For each material in each dataset, we then calculate the standard deviation of the data values at the selected points and use it

to estimate the measurement error. With the data values and measurement error estimate, we use an implementation of Levenburg-Marquardt non-linear parameter estimation [Press et al., 1992] to find the parameters. The parameter-estimation algorithm returns a value,  $\chi^2$ , that measures how well our model fits the data;  $\chi^2 = 1.0$  is a “perfect” fit.

We next describe the equations for several collection protocols. The details of the protocols are not described here; we need only to know the expected signal, noise, and collection time for a given set of collection parameters.

### Spin-Echo 2-D Protocol

Spin-echo protocols can be designed for collecting 2-D slices or 3-D volumes. This section describes a protocol that collects a slice. The protocol has three collection parameters:  $T_R$ , the time between excitations;  $T_E$ , the time from excitation to collection of an echo; and  $\alpha$ , the excitation tip angle (see Table 2.1). The Bloch-equation-based MRI model [Rosen et al., 1984] predicts that the image value,  $v$ , for a particular material with materials parameters  $N(^1H)$ ,  $T_1$ , and  $T_2$  will be:

$$v_{se2}(P_c, P_m) = k_{v.se2} N(^1H) \left( 1 - 2e^{-\frac{T_R - T_E}{T_1}} + e^{-\frac{T_R}{T_1}} \right) e^{-\frac{T_E}{T_2}} \frac{\sin(\alpha)}{1 + \cos(\alpha)e^{-\frac{T_R}{T_1}}} H \frac{FOV_1}{N_1} \frac{FOV_0}{N_0} \quad (2.1)$$

We choose  $k_{v.se2}$  so that  $v_{se2}$  is unitless and measures the signal per voxel.

The deviation is

$$\sigma_{se2}(P_c, P_m) = \frac{k_{\sigma.se2}}{\sqrt{N_a}} \quad (2.2)$$

where  $N_0 N_1$  is the number of samples in a collected slice and  $N_a$  is the number of acquisitions averaged together.  $\sigma_{se2}(P_c, P_m)$  is unitless and measures noise per voxel.

The acquisition time for 2-D spin-echo protocol is calculated as follows:

$$t_{se2}(P_c) = N_a N_g N_1 T_R \quad (2.3)$$

where  $N_g$ , the number of groups of concurrently-acquired slices, is:

$$N_g = \frac{N_2}{\max\left(\left\lfloor \frac{T_R}{T_E + \frac{N_0}{2}} \right\rfloor, 1\right)} \quad (2.4)$$

### Spin-Echo 3-D Protocol

Equations for a 3-D spin-echo protocol are similar to the 2-D case. Expected signal per voxel is

$$v_{se3}(P_c, P_m) = k_{v.se3} N(^1H) \left(1 - 2e^{-\frac{T_R - \frac{T_E}{2}}{T_1}} + e^{-\frac{T_R}{T_1}}\right) e^{-\frac{T_E}{T_2}} \frac{\sin(\alpha)}{1 + \cos(\alpha)e^{-\frac{T_R}{T_1}}} \frac{FOV_2}{N_2} \frac{FOV_1}{N_1} \frac{FOV_0}{N_0} \quad (2.5)$$

Expected noise per voxel is

$$\sigma_{se3}(P_c, P_m) = \frac{k_{\sigma.se3}}{\sqrt{N_a}} \quad (2.6)$$

Collection time is

$$t_{se3}(P_c) = N_a N_2 N_1 T_R \quad (2.7)$$

### Inversion Recovery 2-D Protocol

Inversion-recovery is a different protocol. It incorporates an additional step where the  $T_1$  of a material can influence the resulting image values. As with spin-echo protocols, both slice and volume collections can be implemented. We show the equations for a slice-collecting version of the protocol [Hendrick et al., 1984]. Expected signal per voxel is

$$v_{ir2}(P_c, P_m) = k_{v.ir2} N(^1H) \left(1 - 2e^{-\frac{T_1}{T_1}} - 2e^{-\frac{T_R - \frac{T_E}{2}}{T_1}} + e^{-\frac{T_R}{T_1}}\right) e^{-\frac{T_E}{T_2}} \frac{\sin(\alpha)}{1 + \cos(\alpha)e^{-\frac{T_R}{T_1}}} H \frac{FOV_1}{N_1} \frac{FOV_0}{N_0} \quad (2.8)$$

Expected noise per voxel is

$$\sigma_{ir2}(P_c, P_m) = \frac{k_\sigma \cdot ir2}{\sqrt{N_a}} \quad (2.9)$$

Collection time is

$$t_{ir2}(P_c) = t_{se2}(T_R, T_E, N_a, N_2, N_1, N_0) \quad (2.10)$$

### 2.3.2 Imaging Goals

We next describe how our imaging goals are turned into a constrained optimization problem. We define an objective function,  $E(p)$ , that we want to minimize subject to a set of constraints,  $c_i$ . The constraints are all linear in the parameters that we optimize over, and must be inequalities.

Our objective function is

$$E(p) = \sum_I E_I(p) \quad (2.11)$$

subject to constraints  $c_J$

We decompose each imaging goal into one or more terms,  $E_I(p)$ , in our objective function and one or more constraints  $c_J$ .

#### Goal: Good Tissue Discrimination

This imaging goal is intended to provide sufficient contrast so that pairs of materials can be distinguished from one another. For each pair of materials we define a penalty,  $E_{dij}(p)$ , that is added to  $E(p)$ . This penalty is zero where the material data values,  $v_i$  and  $v_j$ , are sufficiently separated relative to their expected deviations,  $\sigma_i$  and  $\sigma_j$ .

$$E_{dij}(p) = \frac{\max(0, d_{ij}(p) - d_{gij})^2}{k_d} \quad (2.12)$$

where  $d_{gij}$  is the goal separation between the two materials and  $d_{ij}(p)$  is that actual separation.  $k_d$  is

a parameter that weights the relative importance of this penalty term with respect to other terms in  $E(p)$ . It is measured in units of standard deviation. For our optimizations we set

$$k_d = 0.1 \quad (2.13)$$

to indicate that we are concerned with overlaps on the order of 0.1 standard deviations.

For scalar data the separation between two materials,  $d_{ij}(p)$ , is defined as the ratio of the difference between their means and the average of their deviations

$$d_{ij}(p) = \left| \frac{2(v_i(p) - v_j(p))}{\sigma_i(p) + \sigma_j(p)} \right| \quad (2.14)$$

This definition differs from that of contrast-to-noise ratio (CNR) by incorporating a noise estimate for both signal values.

The definition for separation extends to vector-valued data in a straightforward manner under the assumption that the noise in each element of the vector is independent.

### Goal: Observe Machine and Protocol Limitations

Each protocol has certain limits for its parameters. We implement these as constraints on the optimization parameters. For the 2-D and 3-D spin-echo protocols, we define constraints for the minimum and maximum  $T_E$  values that can be used. They are

$$c_{se1} : T_E > k_{se1} + \frac{N_0}{2} DW \quad (2.15)$$

where  $k_{se1}$  is a constant defined for a given machine and  $DW$  is the time necessary to collect a single sample (dwell time).

$$c_{se2} : T_E < T_R - k_{se2} - \frac{N_0}{2} DW \quad (2.16)$$

For the double-spin-echo acquisition we add another constraint to prevent the acquisition times

for the echos from overlapping:

$$c_{d1} : T_{E1} + k_{d1} + N_0 DW < T_{E2} \quad (2.17)$$

### Goal: Minimize Collection Time

We formulate our time-minimization goal as a penalty term,  $E_t(p)$ , added to the objective functions  $E(p)$ .

$$E_t(p) = \frac{t_{protocol}(p)}{k_t} \quad (2.18)$$

Note that this term is linear in the collection time  $t_{protocol}(p)$ . This means that, in general, the overlap penalties, Equation 2.12, will be satisfied before this term has an effect on the optimization.  $k_t$  scales  $E_t$  relative to other terms in  $E(p)$ . We use

$$k_t = 20s \quad (2.19)$$

to indicate that the amount of collection time that we consider to be significant is 20 seconds.

### 2.3.3 Solving the Constrained Optimization Problem

We optimize  $E(p)$  in two steps: first, we search the space of parameters to find a somewhat inaccurate global minimum. With that as a starting point, we use a second solver to refine the accuracy of the minimum. The first search uses a simulated annealing method related to the simplex method [Press et al., 1992]. This optimizer does not have explicit support for constraints. We convert the constraints to a penalty that is very large where they are not satisfied, and zero where they are. Because all of the constraints are inequalities, this has the effect of ruling out infeasible solutions without changing the objective function in feasible regions. The simulated annealing solver evaluates  $E(p)$  many times while searching for a global minimum, and so does not converge very quickly. We use it to search the parameter space and to find an approximately optimal solution.



If there is no feasible solution, the constraints may not be satisfied.

The second optimizer uses a sequential quadratic programming method [NAG, 1993]. It has very good convergence and explicit support for constraints, but does not search the parameter space thoroughly, and so would not find the global minimum alone. We start it with the approximate solution from the first optimizer and it finds a local minimum near its initial solution.

## 2.4 Results

We tested our methods on simulated data, real data of a Dungeness crab collected in a 1.5 Tesla clinical machine, and real data of a mouse embryo collected on an 11.7 Tesla research machine.

### 2.4.1 Simulated Data

We first “collected” simulated data and applied our optimization to it. The “object” that we measured was a pair of concentric spherical shells, as shown in Figure 2.6. The simulated collection process used Gaussian sampling to calculate each sample in each dataset based on the geometry, the material of the “object,” the collection parameters, and Equation 2.1. Normally distributed noise derived from Equation 2.2 was added to each sample.

Figure 2.7 shows one image for each set of collection parameters used. Table 2.3 shows the material parameters used and the results of fitting material parameters to the collected data. A  $\chi^2$  of one would indicate that the model has matched the data exactly.

From the estimated material parameters and a set of imaging goals, we estimate collection parameters that will achieve the goals. Our goals are to achieve a contrast-to-noise ratio of eight between each of the three pairs of materials and to collect data at the same  $10 \times 40 \times 40$  resolution at which the calibration data was collected. We chose the resolution and CNR values to collect data that would work well with our classification algorithms. Figure 2.8 shows two objective functions for a spin-echo collection. In one  $N_a = 3$  and in the other  $N_a = 4$ . The shape of the objective function changes for different values of  $N_a$  with the minimum moving toward smaller  $T_R$  values on

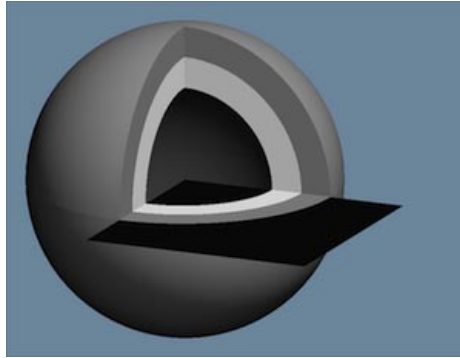


Figure 2.6: The shape of the object shown in the simulated datasets of Figures 2.7 and 2.9 is two concentric spherical shells around a hollow interior. The square shows one slice of collected data. □

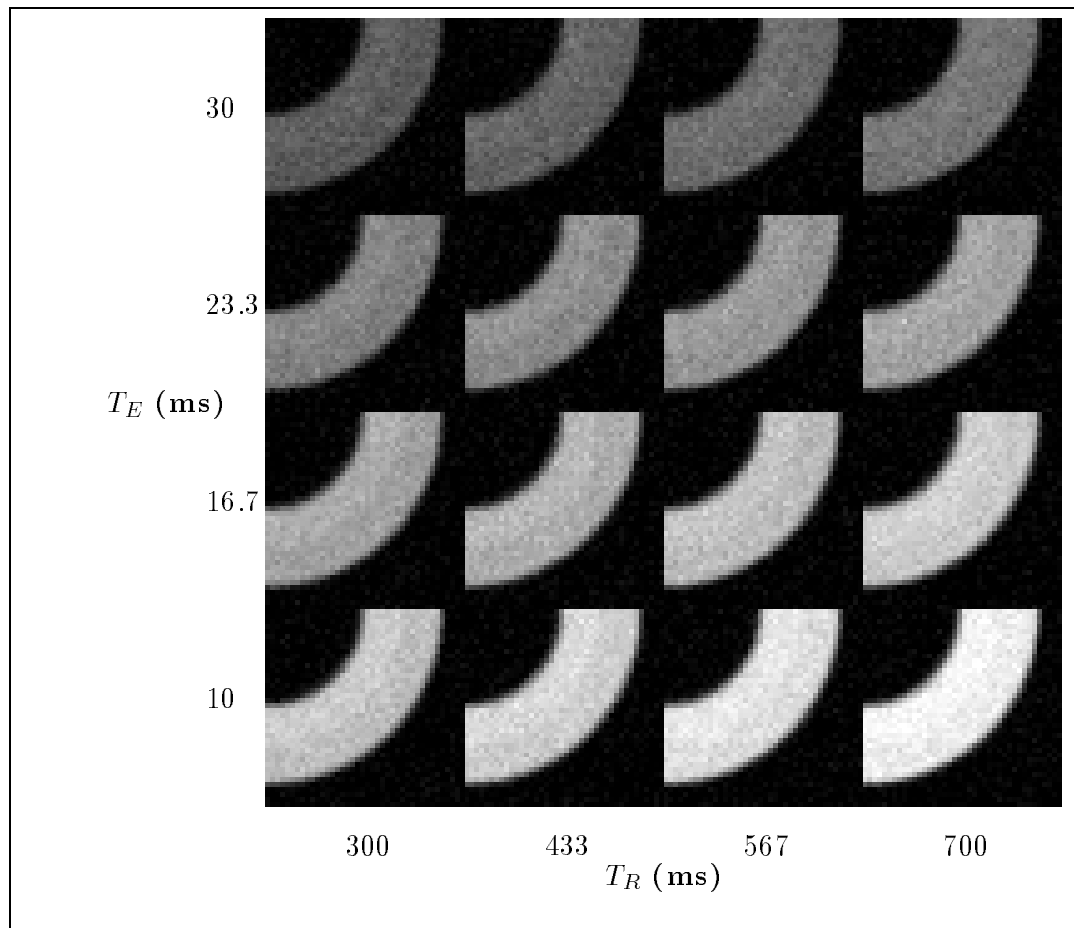


Figure 2.7: An array of simulated data “collected” with different  $T_R/T_E$  combinations. All images are displayed on the same intensity scale, so those with low signal are difficult to see, but still have useful information. The shape of the simulated object in this figure is shown in Figure 2.6. The brighter region is composed of two materials, although they are similar and not well differentiated by the collection parameters shown. □

material	material parameters			$\chi^2$
	$kN(^1H)$	$T_1$ [s]	$T_2$ [s]	
1	3000	1200	120	
fit	$2954 \pm 60$	$1183 \pm 30$	$123 \pm 2.5$	1.01
2	3100	1300	100	
fit	$3269 \pm 72$	$1379 \pm 37$	$97.1 \pm 1.4$	1.01
3	0			
fit	$17.2 \pm 2.1$	$50.6 \pm 222$	$122 \pm 87$	1.01

Table 2.3: Material parameters for simulated data example. The first row for each material shows the parameters used to generate the simulated data, and the second row shows the parameters fit to the data, along with a  $\chi^2$  value. A  $\chi^2$  value of 1.0 indicates that the model fits the data exactly. Values within 0.2 of 1.0 indicate a very good fit. Material 3 has no signal, so  $T_1$  and  $T_2$  are not meaningful.  $\square$

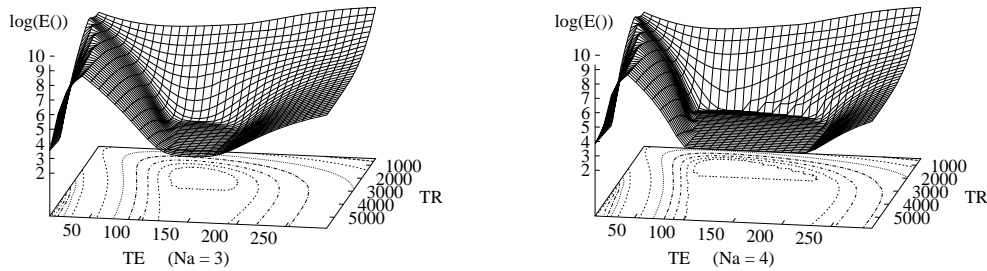


Figure 2.8: The objective function for the simulated example. We have asked for ten slices at 40x40 resolution, and a contrast-to-noise ratio of eight for each pair of materials. This graph shows two versions of the objective functions for a single spin-echo acquisition. On the left,  $N_a$  is fixed at 3, and on the right  $N_a$  is fixed at 4. The flatter region in the center is caused by the time minimization goal. It slopes downward toward the origin. The steeper sections are caused by the material separation goal. Note that the steep sections are less pronounced with a larger  $N_a$  because the expected noise in the dataset is reduced.  $\square$

protocol	$T_R$ [ms]	$T_E$ [ms]	$N_a$	$T_{R_2}$ [ms]	$T_{E_2}$ [ms]	$N_{A_2}$	objective	coll. time [m:s]
spin-echo	1278.9	109.1	4				10.25	3:25
spin-echo	1023.5	96.0	5				10.23	3:25
two spin-echos	1308	110.7	4	13.0	8.0	1	10.75	3:34
double spin-echo	1276.9	104.3	4		114.3		20.52	6:49

Table 2.4: Optimized collection parameters for simulated data using various protocols. Note the two spin-echos solutions have almost identical collection times but different collection parameters. Both solutions satisfy the imaging goals of 10x10x40 resolution and a contrast-to-noise ratio of eight. For the “two spin-echos” case, two independent spin-echo acquisitions are run sequentially.  $\square$

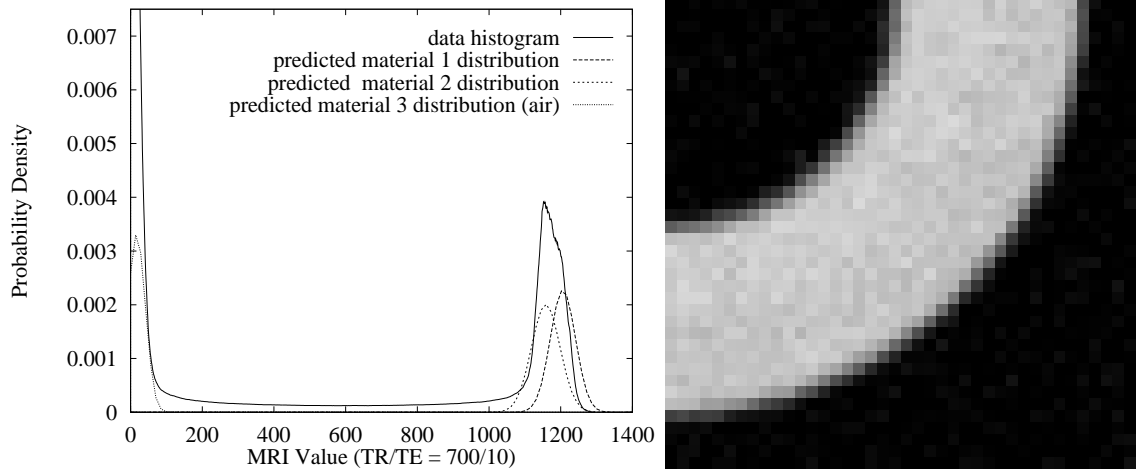


Figure 2.9: Histogram, predicted material distributions, and image from simulated dataset before optimization. There are two materials in this object, but the data values for both are very similar and difficult to distinguish in the image. The similarity is shown in the histogram by the two normal distributions that overlap significantly. The relative heights of the histogram and predicted material distributions are not meaningful.  $\square$

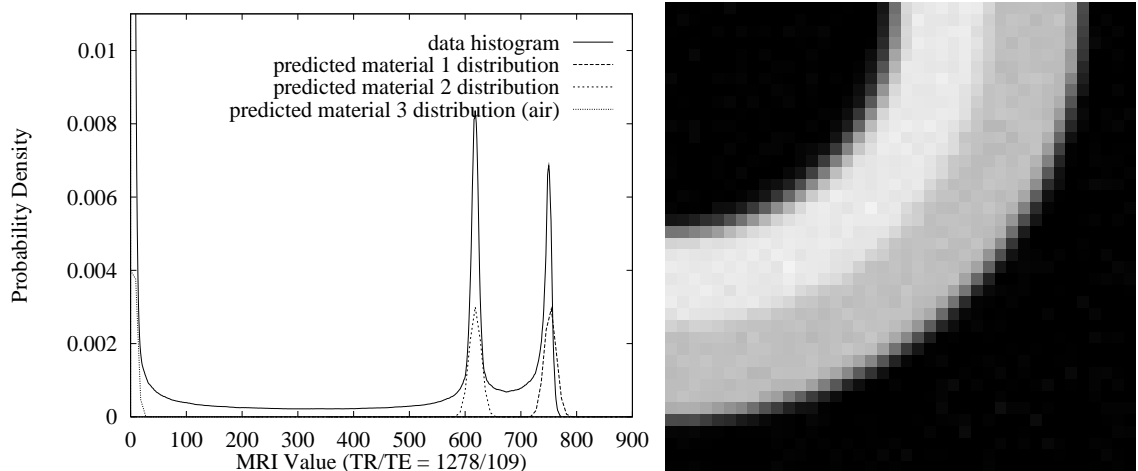


Figure 2.10: Histogram, predicted material distributions, and image of simulated data post optimization. The relative heights of the histogram and predicted material distributions are not meaningful. Note that materials are clearly distinguished in both the histogram and the corresponding slice, unlike in Figure 2.9. Finding equally good collection parameters by trial and error would be very difficult.  $\square$

the right. Table 2.4 shows the optimal objective function values calculated for different protocols. Figure 2.10 shows the results from the optimal protocol. Compare this to Figure 2.9, a trial run with arbitrary parameters. In Figure 2.10 the boundary between the materials is clearly shown.

## 2.4.2 Real Data: Mouse Embryo

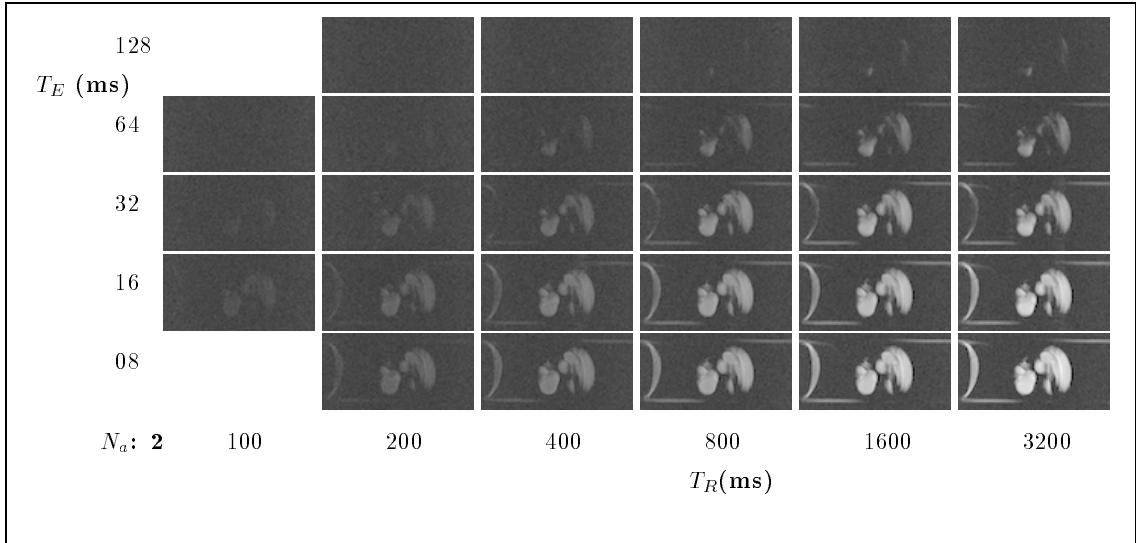


Figure 2.11: An array of datasets of a mouse embryo collected with different  $T_R/T_E$  combinations. The slices are  $500\mu\text{m}$  thick and each voxel  $40\mu\text{m} \times 40\mu\text{m}$ . All images are displayed on the same intensity scale, so those with low signal are difficult to see, but still have useful information.  $\square$

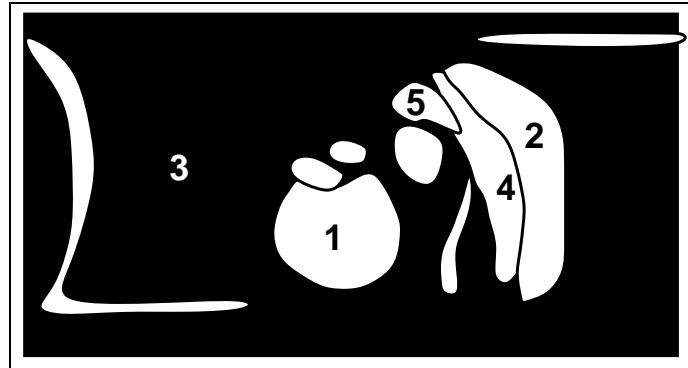


Figure 2.12: Diagram of the shapes shown within each slice of mouse embryo data. Each numbered region indicates an interactively chosen region in collected slice data.  $\square$

Our next example utilized slice data of a fixed mouse embryo collected in a 11.7 Tesla MRI microscope. The mouse was surrounded by agar containing a  $T_2$  contrast agent to nullify signal. We first collected data using a variety of collection parameters. The initial data was  $500\mu\text{m}$  slices with  $40\mu\text{m} \times 40\mu\text{m}$  voxels. Figure 2.11 shows one slice for each set of initial collection parameters used. Within that data we identified regions to treat as uniform materials and interactively picked points within each region from a display of the slices. We show a diagram of the regions in Figure 2.12.

From the chosen points within the datasets and the known collection parameters of the datasets,

material	estimated material parameters			initial data
	$kN(^1H)$	$T_1$ [s]	$T_2$ [s]	$\chi^2$
1	$3793 \pm 28.6$	$1999 \pm 25.6$	$53 \pm 0.4$	1.85
2	$3461 \pm 30.6$	$1369 \pm 20.5$	$44 \pm 0.5$	1.78
3	$45 \pm 1.0$	$8 \pm 135.6$	$5728 \pm 11133.1$	1.98
4	$2963 \pm 38.7$	$1507 \pm 28.8$	$35 \pm 0.3$	1.83
5	$3116 \pm 25.2$	$1374 \pm 19.4$	$32 \pm 0.3$	1.98
estimated material parameters final iteration				
1	$3468 \pm 21.3$	$1710 \pm 15.0$	$54 \pm 0.3$	3.21
2	$3373 \pm 29.4$	$1355 \pm 19.1$	$45 \pm 0.5$	2.05
3	$29 \pm 0.5$	$9 \pm 137.9$	$100000 \pm 649816029.7$	2.52
4	$2685 \pm 34.9$	$1490 \pm 29.0$	$38 \pm 0.3$	1.98
5	$3072 \pm 23.9$	$1328 \pm 16.6$	$32 \pm 0.2$	2.05

Table 2.5: Estimated material parameters for mouse embryo data. We show the parameters as estimated from the initial datasets, and as re-estimated after four steps of the outer level of the optimization process. Each row shows the material parameters for one region in the phantom. See Figure 2.12 for the regions corresponding to each row. Because material 3 has virtually no signal, the  $T_1$  and  $T_2$  parameters have almost no influence on Equation 2.1 and the fitted values are arbitrary.  $\square$

iter.	protocol	$T_R$	$T_E$	$N_a$	$T_{R_2}$	$T_{E_2}$	$N_{A_2}$	objective	coll. time
		[ms]	[ms]		[ms]	[ms]			
1	spin-echo	1272.08	7	28	na	na	na	238.442	1:15:59
	two spin-echos	14.2555	9.26	2	1272.12	7	28	238.763	1:16:03
2	spin-echo	1317.62	8.28	30	na	na	na	258.747	1:24:20
	two spin-echos	1318.64	8.27	30	12	7	2	259.177	1:24:27
3	spin-echo	1524.26	7	30	na	na	na	310.623	1:37:33
	two spin-echos	1126.71	7	16	1738.63	7	16	310.715	1:37:48
4	spin-echo	1343.72	9.40	38	na	na	na	336.161	1:48:56
	two spin-echos	1344.3	9.39	38	19.483	14.48	2	336.653	1:49:04

Table 2.6: Optimized collection parameters for phantom data using two protocols.  $\square$

we estimated material parameters for each of the materials as outlined in Section 2.3.1. The estimated material parameters for this example are shown in the top half of Table 2.5. Because material 3 produces virtually no signal in the datasets we collected, the  $T_1$  and  $T_2$  values are not meaningful.

From the estimated material parameters and a set of imaging goals we estimate collection parameters that achieve the goals. Our collection goals are to achieve a contrast-to-noise ratio of six between each pair of materials, and to collect data at the same  $256 \times 128$  resolution as the

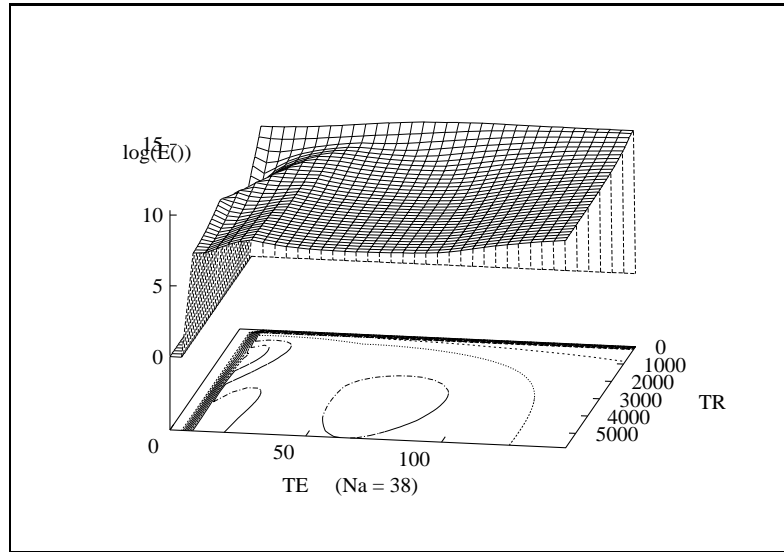


Figure 2.13: An example of the objective function for the mouse embryo. We have asked for one slice at  $256 \times 128$  resolution, and a contrast-to-noise ratio of six for each pair of adjacent materials. This graph shows the objective function for single spin-echo acquisition with  $N_a$  fixed at 38.  $\square$

initial data. We iterated the outer loop of the optimization process four times collecting data at the suggested optimum after each iteration. The results of each step of the outer-level optimization are shown in Table 2.6. For each step we estimated new material parameters from both the initial datasets and all new ones. The results of the material parameter estimation for the fourth and final iteration are shown in the bottom half of Table 2.5.

Figure 2.13 shows the objective function for the fourth iteration of the outer level optimization, a spin-echo collection with a fixed  $N_a = 38$ .

Figure 2.14(i) shows a larger image of one of the initial datasets, and Figures 2.14(ii)–(iv) show data collected using the optimal protocol and parameters from the last three outer-level optimization steps. The results of the outer-level optimization are discussed in Section 2.5.1.

### 2.4.3 Real Data: Dungeness Crab

Our next example utilized Dungeness crab embedded in gelatin. The crab was dispatched with an overdose of anesthetic; the gelatin prevented motion and provided contrast between the crab shell and the surrounding space.

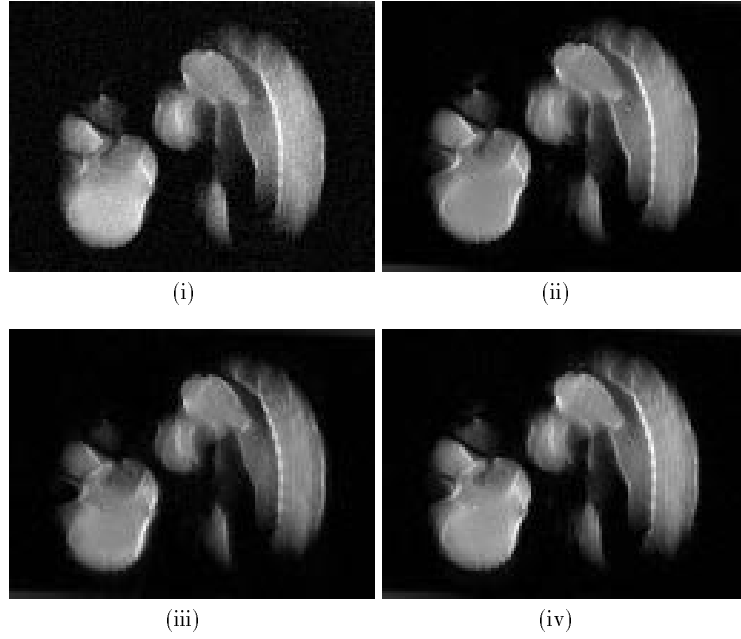


Figure 2.14: Data collected: (i) initially and (ii)–(iv) during the last three outer-level optimization steps. Table 2.6 shows the collection parameters for (ii)–(iv) optimization. See Section 2.5.1 for a discussion of the outer-level optimization process.  $\square$

material	material parameters			$\chi^2$
	$kN(^1H)$	$T_1$ [ms]	$T_2$ [ms]	
gelatin	$1477 \pm 3.8$	$1782 \pm 10.1$	$701 \pm 9.1$	1.49
muscle	$1410 \pm 10.4$	$1193 \pm 15.6$	$64 \pm 0.8$	2.38
water	$1420 \pm 20.6$	$1803 \pm 42.2$	$147 \pm 3.3$	1.93
shell	$80 \pm 6.3$	$141 \pm 15.9$	$1424 \pm 528.7$	1.33

Table 2.7: Material parameters for crab data example. Each row shows the material parameters for one material in the crab. A set of points representing each material is chosen interactively.  $\square$

We first collected data using a variety of collection parameters. Figure 2.15 shows one slice for each set of collection parameters used, and Table 2.7 shows the results of estimating parameters for each material we have chosen within the crab.

From the estimated material parameters and a set of imaging goals, we estimate collection parameters that achieve the goals, which were a contrast-to-noise ratio of ten between each pair of materials and a collection resolution of  $512 \times 512 \times 34$  identical to the initial data. Table 2.8 shows



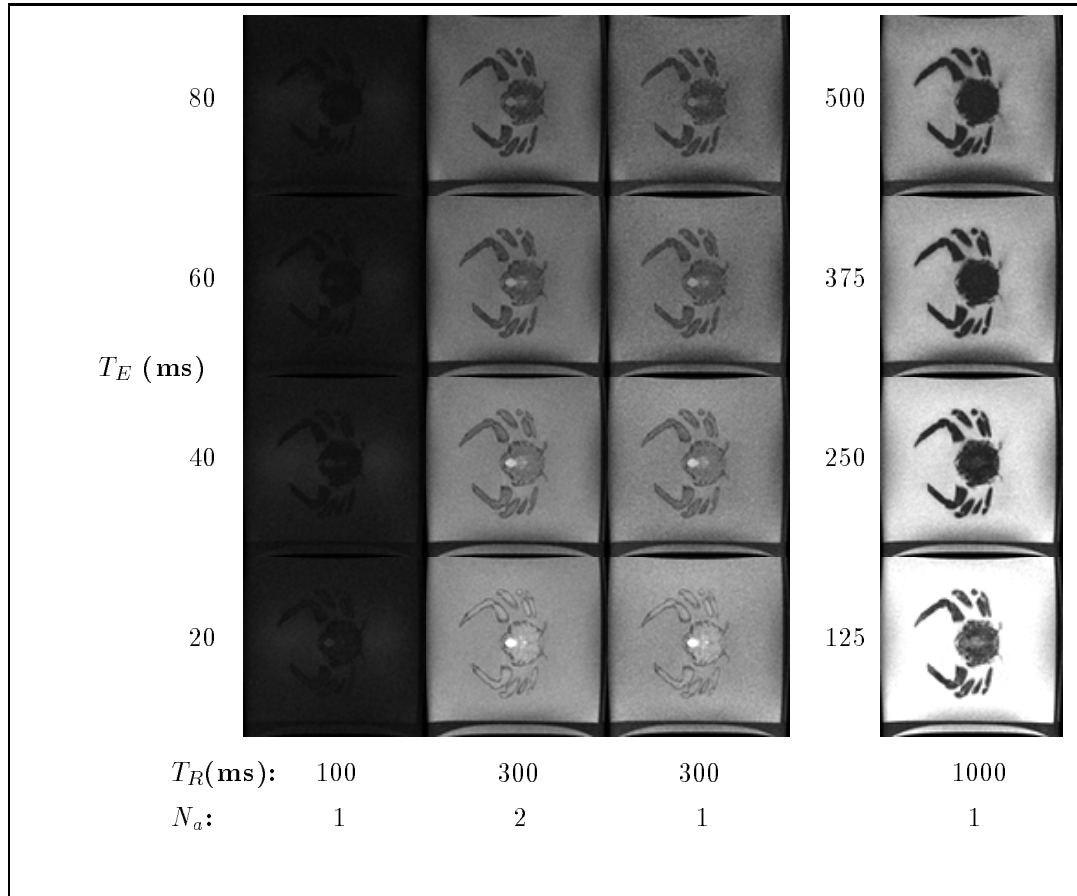


Figure 2.15: An array of datasets collected with different  $T_R/T_E$  combinations. All images are displayed on the same intensity scale, so those with low signal are difficult to see, but still have useful information.  $\square$

protocol	$T_R$ [ms]	$T_E$ [ms]	$N_a$	$T_{R_2}$ [ms]	$T_{E_2}$ [ms]	$N_{A_2}$	objective	collection time [m:s]
double spin-echo	2589	55	1		70		66.314	22:05
two spin-echos	3246	89.5	1	714	15	1	101.376	33:48
spin-echo	4232	63.7	1				109.515	36:07

Table 2.8: Optimized collection parameters for crab data using three protocols. The collection time value is for thirty-four 3-mm slices of resolution 512x512 with no inter-slice spacing. The goal contrast-to-noise ratio was ten.  $\square$

the optimal objective function values calculated for different protocols and Figure 2.16 the objective function for a fixed  $N_a = 1$ . Figure 2.17 shows data collected using the optimal protocol and parameters.

Figure 2.18 compares the predicted data and noise values from the optimization process with the data and noise values collected on the machine. Each cross is centered at the mean value for

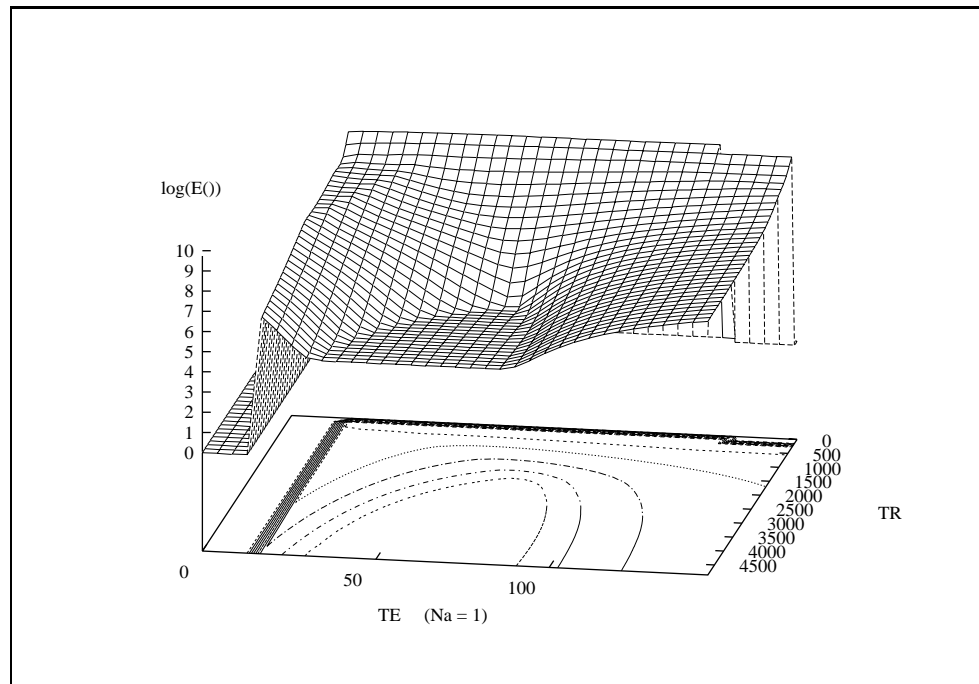


Figure 2.16: Objective function for the crab datasets. We have asked for 34 slices at  $512 \times 512$  resolution, and a contrast-to-noise ratio of ten for each pair of materials. This graph shows the objective function for a single spin-echo acquisition with  $N_a$  fixed at 1. As in Figure 2.8, the flat area is due to the time-minimization goal and the steep areas surrounding it to the material separation goal. The objective function is shown as zero where constraints preclude solutions, primarily around the left and back edges. □

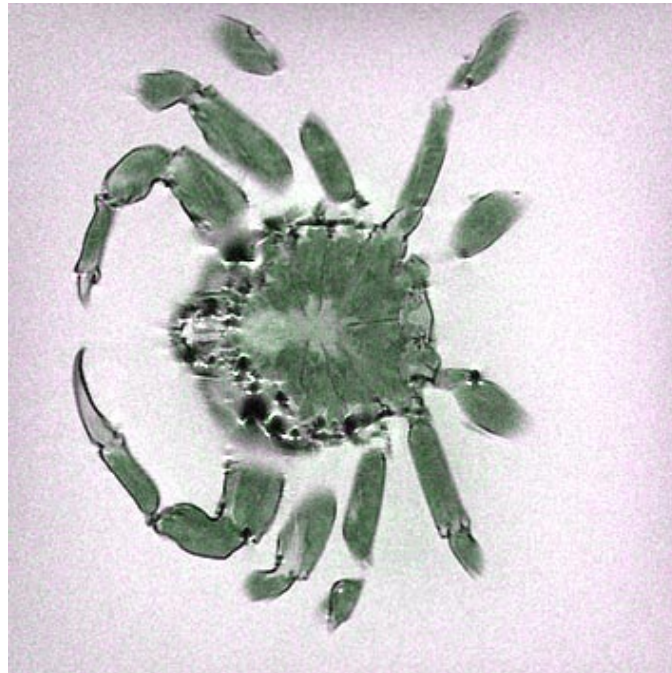


Figure 2.17: One slice of crab data collected using the optimized parameters. Note the contrast between gelatin, shell, muscle, and water. The muscle and water are distinct materials within the claws. □

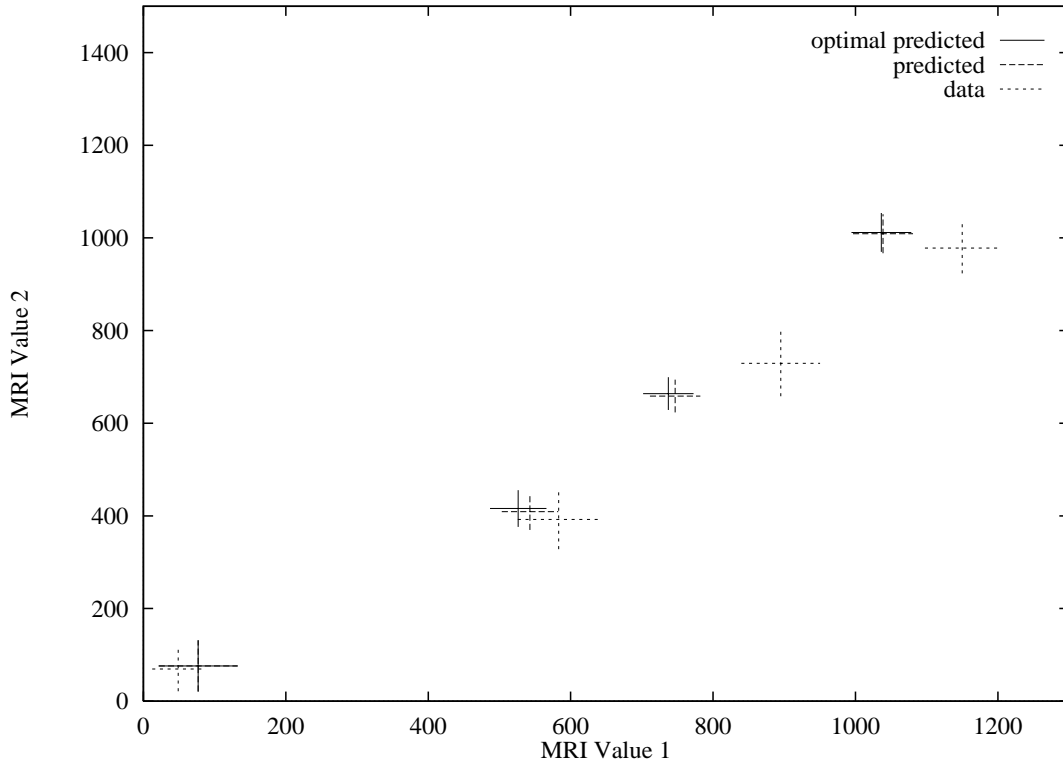


Figure 2.18: Mean and deviation values predicted by the optimization process and collected on the machine. Each cross represents one material and is centered at the mean value for the material. The cross extends one standard deviation away from the mean in each direction. The four solid crosses show the predicted values for the optimal collection parameters. The dashed crosses nearest the solid ones show predicted values for the collection parameters we actually used. The other set of dashed crosses shows the measured mean and deviation in data collected from a real crab. See Section 2.5.2 for more discussion. Data was collected on a GE Signa 1.5 Tesla MRI machine. □

a material and extends one standard deviation away from the mean in each direction. The crosses labeled “optimum predicted” are the expected mean and deviation for the optimal protocol listed in Table 2.8. Due to changes in the size of the crab and surrounding gelatin and due to inaccuracies in the machine protocol limitations, the optimal parameters were not possible. Instead of collecting data at  $T_R/T_{E_1}/T_{E_2} = 2589/55/70$ , we used  $T_R/T_{E_1}/T_{E_2} = 2583/53/71$ . The “predicted” and “data” crosses show the expected and measured mean and deviation for the parameters we collected.

## 2.5 Discussion

In this section we explain how our results show the tradeoffs between different protocols, speculate on some characteristics of our MRI material model, reflect on the impact of various choices for

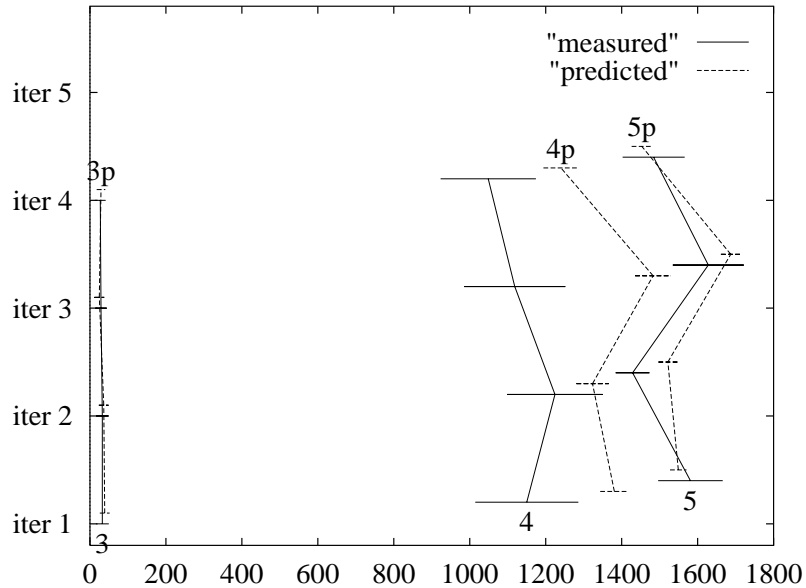


Figure 2.19: Predicted and measured mean values and standard deviations for each material/iteration combination in the mouse embryo optimization process. The dashed lines represent predicted values and the solid lines measured values. Each mean/deviation is shown as a line segment extending one deviation to the left and right of the mean value, and mean values for the same material are connected together. □

the contrast-to-noise imaging goal, and discuss some issues surrounding the simulated annealing solver.

### 2.5.1 Data Collected from Mouse Embryo

The outer-level optimization process did not converge well in four steps. With each step, the algorithm discovered a new predicted optimal solution, but the predictions did not match the data collected with the suggested parameters.

Figure 2.19 shows the predicted and measured mean and deviation for each of the materials for each of the optimization steps. Each mean/deviation pair is represented by a line segment centered at the mean and extending for one deviation to the right and left. Mean values for a single material are connected, with iterations running from the bottom to the top. The solid lines are predicted values and dashed lines measurements.

We believe that the prediction inaccuracies are due to inaccuracies in the MRI material and collection model, which we discuss further in Section 2.5.3. In particular, for the slices we

collected, the slice thickness was over ten times larger than the other voxel dimensions, and so voxels containing a pure material were difficult to find.

### 2.5.2 Data Collected from Dungeness Crab

We collected data from one crab and used it to optimize parameters for another. The signal and noise values in the datasets from the second crab did not exactly match the predicted values generated using the datasets from the first crab. There are a number of possible explanations for this. First, the sample was different, although the species in both cases were the same and the preparation as similar as possible. Second, in addition to regular calibration changes, the MRI machine was serviced between the initial and final collections, and parts of the gradient amplifiers were replaced. Third, the temperature of the sample was different between the initial collections and the final collection. Any of these changes could have affected the data values.

A solution to this problem is to collect initial data, run the optimization while the sample remains in the machine, and then immediately collect optimized data. The reduced lag time has the advantage of providing immediate improvement to the collection process and avoiding any changes that are likely to impact the results. The time to run the optimization is only a few minutes with the current implementation, and could be sped up significantly.

Our MRI material and collection model also impacts the accuracy of the predictions. See Section 2.5.3 for more detail.

### 2.5.3 MRI Material and Collection Model

For a model that matches a set of data values with known normally distributed noise,  $\chi^2$  should be 1. Our simulated data, which is generated with the same model used to fit it, has  $\chi^2 = 1.01$  for all materials. Within the Dungeness crab and mouse embryo datasets, however,  $\chi^2$  ranges from 1.33 to 3.2. A model that does not fit well creates less-accurate predictions, and data collected at the predicted points will not satisfy our goals.

We speculate on a number of reasons for the large  $\chi^2$  values. First, in materials with very little

signal, such as gasses, hard solids, or the agar/contrast-agent combination used around the mouse embryo, there is virtually no decay of the signal values. The  $T_1$  and  $T_2$  parameters, therefore, provide unused degrees of freedom to the fitting process. In addition, because data values in MR images are magnitudes of complex numbers, the values will not be normally distributed. For values where the mean is far from zero relative to the standard deviation, the distribution is very close to normal. When the mean is close to zero relative to the standard deviation, the distribution can be quite different from a normal distribution. Our current implementation treats the distribution as normal, and so gets inaccurate estimates for the signal and noise measurements. It should be possible to identify both of these cases and correct for them in fitting the model and predicting results.

A second reason for the large  $\chi^2$  values is that each sample value is an integral over a region of space. The value incorporates effects from each material within that region, and may not be representable with a single  $N(^1H)$ ,  $T_1$ , and  $T_2$  value. This effect can occur in regions where materials are mixed together at a scale much smaller than a single voxel. It should be possible to identify cases where this is happening and address them either by choosing points where materials are not mixed or by fitting multiple parameter sets to each material to take this small-scale mixing into account. Chapters 3 and 4 illustrated work in classification of voxels containing mixtures of materials, and this work may be applicable to the material parameter fitting problem as well.

Finally, the MRI model may fit collected data well, and yet not predict data values accurately. In particular, when predicting values for collection parameters far from the collection parameters used to estimate material parameters, material signatures are less accurate. Iterating the outer loop of the optimization procedure to collect data near the predicted optimal point addresses this problem.

#### 2.5.4 Choice of Protocol

We observe from our experiments that optimizations on machines that support a double spin-echo collection protocol generally achieve the requested imaging goals with a shorter collection time than either one or two single spin-echo acquisitions. The double spin-echo protocol collects twice the

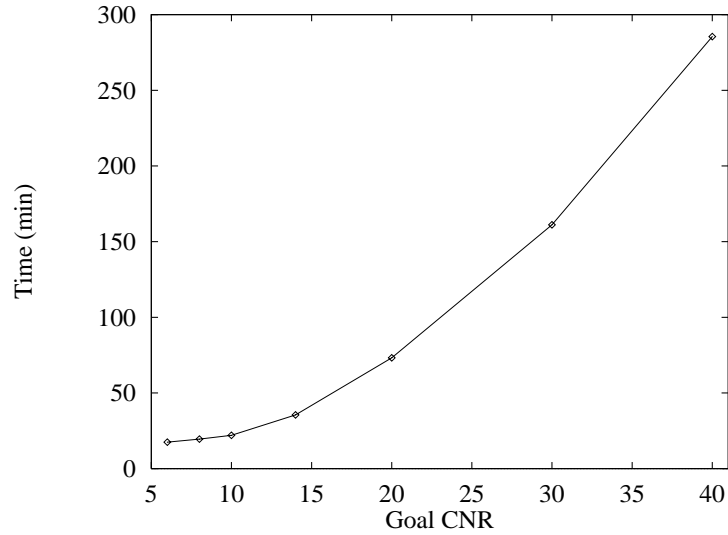


Figure 2.20: Optimal collection time as a function of contrast-to-noise ratio (CNR). □

data in the same amount of time, improving the signal-to-noise ratio by a factor of  $\sqrt{2}$ , an advantage that almost always overshadows the advantage of two single-echo acquisitions, despite their two different  $T_R$  values. In addition to the increase in the signal-to-noise ratio over one single-echo dataset, the second data value collected by a double spin-echo acquisition has a second echo time and so can achieve contrast between materials not distinguished by the first echo alone.

### 2.5.5 Choice of Contrast-to-Noise Ratio (CNR)

The choice of contrast-to-noise ratio between pairs of materials has a significant impact on the resulting collection time. Figure 2.20 shows optimal collection times for the Dungeness crab dataset for a selection of CNR values. For CNR goals less than about 10, the CNR can be achieved without increasing the number of averages,  $N_a$ . As the goal goes above 10,  $N_a$  must be increased. Each factor of  $n$  CNR gain, then, requires a factor of  $n^2$  increase in  $N_a$ , and a correspondingly quadratic increase in collection time.

### 2.5.6 Solver

**Simulated Annealing.** Simulated annealing is essential for finding good solutions to the optimization problem we have constructed. The objective function has multiple local minima, some comparable in magnitude, and some not. Most non-stochastic solvers will find only a nearby local minima, which may not be adequate. The objective function can also have discontinuities, particularly for the spin-echo 2-D protocol, where the collection time depends on the number of slices that can be simultaneously collected during a single  $T_R$ . Many solvers assume continuity and fail when that assumption is violated.

**Annealing Schedule.** We have implemented the annealing schedule suggested in [Press et al., 1992]. The initial annealing temperature is dependent on the CNR imaging goal that we set because a higher CNR goal creates higher ridges in the objective function. For a CNR goal,  $g$ , the maximum contribution along a ridge created by the goal is  $\left(\frac{g}{2k_d}\right)^2$ . Taking into account overlapping ridges and the collection-time component of the objective function, we have used an initial temperature of 5000 for CNR goals up to 10.

The annealing schedule must be sufficiently long to explore the space of possible parameters to find the optimum. The number of function evaluations depends on the number of parameters a protocol has. For three parameters (2-D spin-echo), 7000 evaluations have been sufficient; for four parameters (2-D double spin-echo), 12000; and for six parameters (two 2-D spin-echos), 18000.

**Speed.** Simulated annealing is slow, but for our problems the algorithm has been fast enough, requiring on the order of 2–15 minutes on an HP9000/700 workstation to find an optimal solution among two or three protocols. This is fast enough for an object to remain in a scanner while a new set of parameters is calculated.



## **2.6 Conclusion**

We have presented a goal-based framework for setting up and solving an optimization problem to find the best protocol and set of parameters for collecting MRI data. Within this framework we have shown how to implement imaging goals that encode resolution and contrast-to-noise-ratio requirements of the resulting data, limitations of the MRI machine and collection protocol, and other goals such as the desire to minimize collection time. The optimization process is independent of protocol, and we have incorporated a selection of protocols into our implementation.

We have used our implementation to find an optimal protocol and set of parameters for samples in two MRI machines, as well as for simulated data. The results indicate that an accurate model of the MRI process improves the accuracy of the optimization process and support our hypothesis that constrained optimization can be used to select good MRI collection protocols and parameters.

## **PART II**

# **Bayesian Tissue Classification**

The following three chapters describe a Bayesian framework for classifying MRI data and two algorithms developed within the framework. Chapter 3 gives an introduction to the problem, describes a new Bayesian framework for creating algorithms to solve the problem, and summarizes a family of new algorithms we have created within the framework. The algorithms are described in detail in Chapters 4 and 5.

## Chapter 3

---

# Bayesian Tissue-Classification Framework

---

Material classification is a key step in creating computer graphics models and images from volume data (see Figure 3.1). We present a new Bayesian framework for constructing classification algorithms and several new algorithms constructed within the framework.

The new algorithms identify the distribution of different material types in volume data such as those produced with Magnetic Resonance Imaging (MRI) or Computed Tomography (CT). We apply them to MRI data because MRI measures spatial information about the chemical structure of an object. Our algorithms treat a voxel as a volume, not as a single point. We reconstruct a continuous function from the sampled data and use all of the values within each voxel volume to identify materials within the voxel using a probabilistic approach. The algorithms further assume that voxels can contain more than one material, e.g., muscle, fat and bone; we compute the relative quantity of the constituent materials within each voxel.

Other classification methods, as discussed in Section 3.1.1, have utilized Gaussian probability density functions to model the distribution of values within a dataset. Gaussian basis functions work well for voxels containing unmixed materials. They do not work well where the materials are mixed

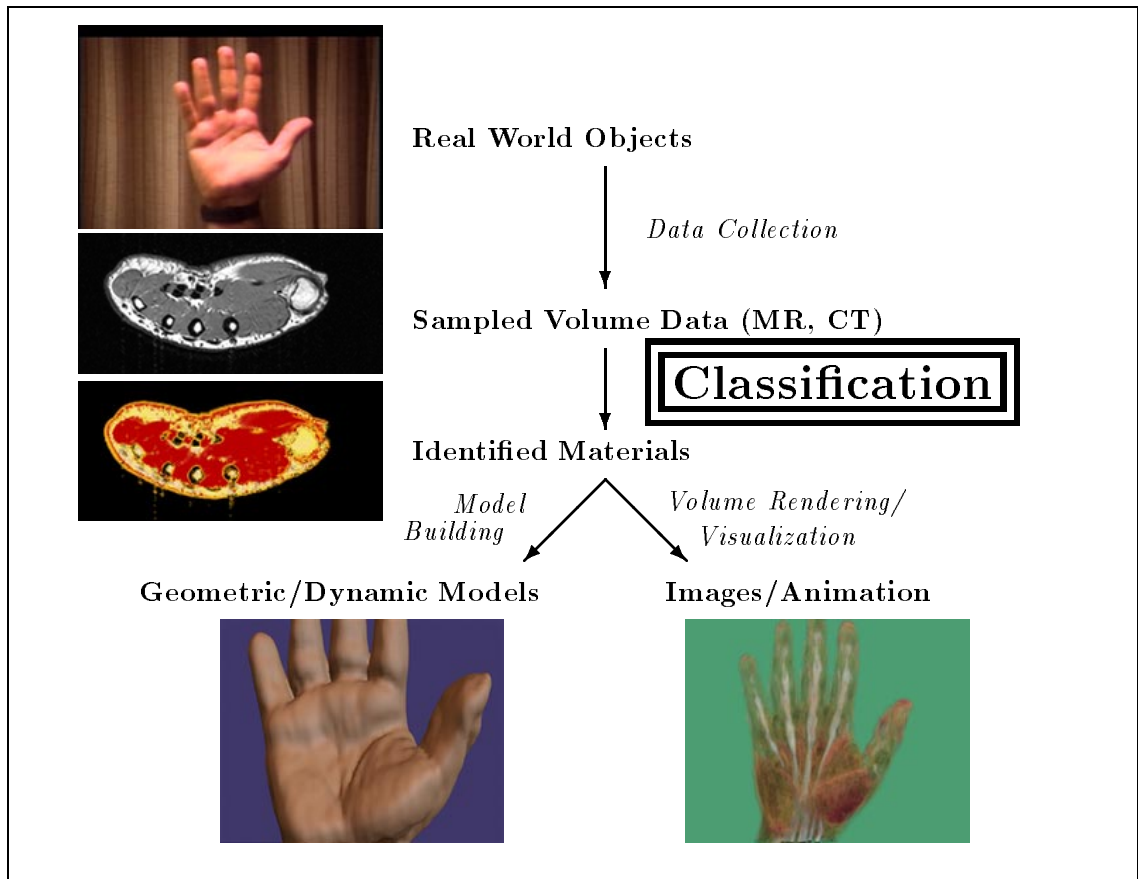


Figure 3.1: Our computational framework for creating geometric models, as shown earlier in Figure 1.1. In Chapters 3–5 we describe the classification step, emphasized in the diagram. Our new techniques identify materials in sampled volume data to produce a new sampled volume dataset for each material. □

together because measurements combine characteristics of their component materials and are not normally distributed. We extend the approach by deriving non-Gaussian “mixture” basis functions.

Because we model mixtures of materials and treat voxels as volumes, our techniques reduce the classification artifacts that occur along boundaries between materials. The techniques are useful for making higher quality geometric models and renderings from volume data, and have the potential to make calculations of tissue volumes within a dataset more accurate. They also classify noisy, low-resolution data well.

## 3.1 Introduction

We begin by describing related work and defining terms. We then present the Bayesian framework we have developed to create classification algorithms and work through a simple example to illustrate the process. Section 3.3 gives an overview of the family of new algorithms that we have developed, deferring their detailed descriptions to Chapters 4 and 5.

### 3.1.1 Related Work

Much previous work is devoted to material classification in sampled datasets such as those produced by MRI or CT [Duda and Hart, 1973]. [Clarke et al., 1995] presents a review of classification methods applied to MRI data. Many of the techniques introduce classification artifacts, particularly on boundaries between different materials. The artifacts, which tend to appear as jaggy stair steps or as additional surfaces, are particularly detrimental to computer graphics images and models.

Discrete statistical classification techniques are often used to identify a single class for each sample within a dataset [Vannier et al., 1985], [Vannier et al., 1988], [Cline et al., 1990]. Each class contains samples representing a particular material. These techniques work well in regions where only one material is present, as in the interiors of single-material regions, but tend to fail where voxels contain boundaries between regions, since a given sample does not represent a single material there (see Figure 4.1).

[Choi et al., 1991] presents a method that models each sample as representing a mixture of materials. The technique, like many others, classifies a region based on a single measurement within the region, effectively treating each voxel as a single point.

### 3.1.2 Definitions

We refer to the coordinate system of the space of the object we are measuring as *spatial coordinates* and generally use  $x \in X$  to refer to points.  $X$  is  $n_x$ -dimensional, where  $n_x$  is 3 for volume data, but can be 2 for slices.

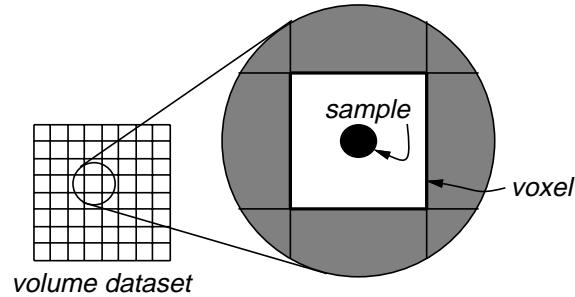


Figure 3.2: We define a sample as a scalar or vector valued element of a multi-dimensional dataset. A voxel is the region surrounding a sample.  $\square$

Each measurement, or *sample* (see Figure 3.2), may be a scalar or vector and lies in *feature space* (see Figure 4.3), with points frequently denoted as  $v \in V$ . Feature space is  $n_v$ -dimensional, where  $n_v$  is one for scalar-valued data, two for two-element vector data, etc.

From the samples we reconstruct a continuous function  $\rho(x)$  over  $X$  by interpolating sample values. We use tricubic interpolation and so incorporate information from 64 nearby samples into each interpolated measurement. A *voxel*, *voxel volume*, or *voxel region* (see Figure 3.2) is the volume surrounding a sample. The terms are interchangeable. We use voxel volumes that exactly cover the volume, but overlapping or non-adjacent voxels are also possible. We are frequently interested in the behavior of  $\rho(x)$  over the region defined by the volume of a voxel.

Classification algorithms classify a voxel based on information derived from the raw data in or near the voxel. We refer to the information as *voxel-info*, and label it  $h$ .

### 3.2 A Framework for Solutions

We define a new statistical framework (see Figure 3.3), using Bayesian probability theory [Loredo, 1989] and approximations of conditional and prior probabilities, for creating classification algorithms. Within that framework we have created a family of new algorithms that calculate the probability of a particular combination of materials given the histogram over a small region. We then find the most likely combination for the region.

In contrast with other work, we treat each voxel as a volume. Ideally, we would like to measure

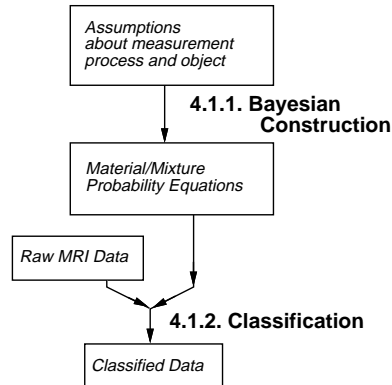


Figure 3.3: Steps in creating and using a new Bayesian classifier. In the first step we construct classification probabilities, which estimate the probabilities of different combinations of materials within a voxel. The second step, classification, iterates over each voxel applying the classifier to determine the most likely materials. □

the exact material at each point within the volume. The data-collection process does not sample the volume at every point; however, based on an assumption about the process, we can reconstruct from the samples a band-limited function  $\rho(x)$  that is defined over the volume [Oppenheim et al., 1983]. With the distribution of values from  $\rho(x)$  over the volume of a voxel, we identify materials within the voxel probabilistically. By using the reconstructed continuous measurement function  $\rho(x)$  and not just a single measurement, we incorporate more information into the classification process and therefore increase its accuracy.

In this section we outline how to construct a new classification algorithm within our framework, illustrating the process with an existing algorithm.

### 3.2.1 Bayesian Construction of Material Probabilities

The construction involves four steps: choosing voxel-info to represent the information in a voxel, selecting a set of assumptions about the collection process, defining a parameterized model of the voxel-info, and deriving material probability estimates.

**Choose voxel-info.** Our new algorithms use histograms calculated over the region of a voxel as voxel-info; other choices are possible, as we explore in Section 8.2.3. We have chosen histograms for a number of reasons. First, they generalize single measurements to measurements over a region,

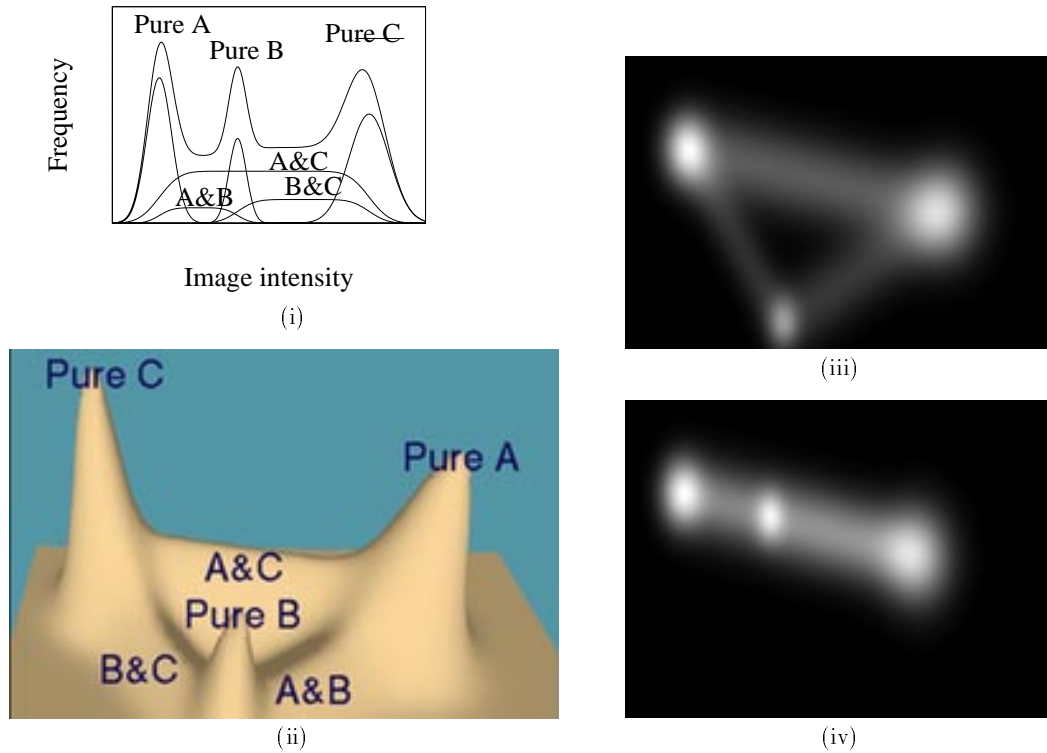


Figure 3.4: Benefits of histograms of vector-valued data. We show histograms of an object with three materials. (i) is a histogram of scalar data and shows that material mean values are collinear; therefore, distinguishing among more than two materials is often ambiguous. (ii) represent a histogram of vector-valued data, with one MRI value along the axes at the bottom of the figure and one along the left side. Brighter points represent larger values of the histogram. The histogram shows that mean values often move away from collinearity in higher dimensions. (iii) is another representation of the same histogram. (iv) shows a different histogram demonstrating that the collinearity problem can occur with vector-valued data. □

so classification concepts that apply to single measurements generalize. Second, the histograms can be calculated easily. Third, the histograms capture information about neighboring voxels, which increases the information content of the voxel-info and improves the classification results. Fourth, histograms are orientation independent; orientation independence reduces the number of parameters in the classification process hence simplifying and accelerating it.

As with many other techniques, ours works on vector-valued volume data, in which each material has a characteristic vector value rather than a characteristic scalar value. Vector-valued datasets have a number of advantages and generally give better classification results. First, they have an improved



signal-to-noise ratio. Second, they frequently distinguish similar materials more effectively (see Figure 3.4).

In particular, the jump from scalar to two-element vector data is very important. In scalar-valued datasets it is difficult to distinguish a mixture of two pure materials with values  $v_A$  and  $v_B$  from a pure material with some intermediate value such as  $v_C = (v_A + v_B)/2$ . This is because all three material values are collinear, as they must be for such a dataset.

With more measurement dimensions in the dataset, collinearity is less frequent for most combinations of three or more materials, although Figure 3.4(iv) illustrates that it can still occur. When it does occur, classification works as for scalar-valued data.

We assume different scalar-valued datasets are spatially aligned so that we can build vector-valued datasets from them.

**Codify collection assumptions.** In the second step we codify a set of assumptions about the data-collection process. The assumptions embody information about:

- how sampling works on the machine we are using,
- the responses of materials or combinations of materials to the measurement process,
- the spatial uniformity of the measurements, and
- geometric restrictions in our objects.

For our example we will assume that there is a known discrete set of materials, that measurements for a single material are distributed normally, and that each voxel consists of exactly one material. Section 3.3 lists the assumptions for our new algorithms, some of which are illustrated in Figures 4.1 and 5.1.

**Model voxel-info.** From our choice of voxel-info and the set of assumptions about the data-collection process, we define a parameterized model of the voxel-info,  $f(\alpha)$ . The parameters for the voxel-info model are divided into two classes. The first, *dataset parameters*, consists of those that

Dataset parameters		
$\mu_i$	continuous	mean value for material $i$
$\sigma_i$	continuous	standard deviation for material $i$
Voxel parameter		
$\alpha$	discrete	material

Table 3.1: Parameters for the example classification algorithm. Dataset parameters are constant within a given dataset, while the voxel parameter varies for each voxel.  $\square$

are known before the voxel classification process. The second, *voxel parameters*, can vary from voxel to voxel.

For our example the dataset parameters are shown in Table 3.1.

**Estimate material probabilities.** Given voxel-info,  $h$ , which encodes information from a single voxel and a parameterized model of the voxel-info,  $f(\alpha)$ , we want to find the most likely set of parameters  $\alpha$ . The *posterior probability* defines how likely a set of parameters  $\alpha$  is given an observed voxel-info  $h$ :

$$P(\alpha|h) \tag{3.1}$$

By maximizing the posterior probability we find the most likely set of parameters. Equation 3.1 cannot, in general, be calculated directly, so we use Bayes' Theorem to decompose it into pieces that we can either calculate directly or estimate.

$$P(\alpha|h) = \frac{P(\alpha)P(h|\alpha)}{P(h)} \tag{3.2}$$

$P(h|\alpha)$  is the *likelihood* of a particular instance of voxel-info for a given set of voxel parameters. We calculate it by comparing the parameterized model of the voxel-info to the actual voxel-info and quantifying the difference.

$P(\alpha)$  is the *prior probability* and tells us how likely each set of parameters is. We estimate the prior probability from the model of the voxel-info and from the assumptions that we make about

the data-collection process.

$P(h)$  is the *global likelihood* of a particular instance of voxel-info. We assume that it is a constant function of  $h$ . It becomes a normalization factor for Equation 3.2.

The specific estimates for each of our algorithms are described in subsequent chapters. In the following section we work through the derivation for an example.

The posterior probability calculation is used within the classifier. For our example, the classifier calculates the probability of each material for a given measurement and chooses the most likely material. See Section 4.11 for the detailed derivation of a classifier.

### 3.2.2 Classification

**Estimate dataset parameters.** The dataset parameters must be estimated before the classifier can be used. We estimate them by calculating their values for a training set of voxel-info with known voxel parameters. In our example we would calculate the mean and variance of a set of measurements known to be from each discrete material.

**Classify voxels.** Finally, we calculate the voxel-info for each voxel and use the classifier to estimate the voxel parameters.

### 3.2.3 Example of Classification Algorithm Construction

In this section we construct the Bayesian classifier for the example we introduced in Section 3.2. This classifier is not new [Duda and Hart, 1973], but its construction within our framework illustrates how to create a classifier.

**Example voxel-info.** For our example we define voxel-info  $h_e$  as the single data measurement at the center of a voxel.

**Example assumptions.**

- $e_1$ : Each measurement comes from exactly one material.
- $e_2$ : The measurements from each material are normally distributed.
- $e_3$ : We know the number of materials and can identify samples from each material within the data.
- $e_4$ : All materials are equally likely.

**Example model of voxel-info.** Our model of the voxel data,  $f_e(\alpha_e)$ , has a single discrete voxel parameter,  $\alpha_e$ , that specifies the material within the voxel.

$$f_e(\alpha_e) = \mu_{\alpha_e} \quad (3.3)$$

For each material  $i$ , our model has two dataset parameters,  $\mu_i$  and  $\sigma_i$ , defining the expected value and the standard deviation of measurements.

**Example material probabilities.** From assumptions  $e_1$  and  $e_2$ , the likelihood,  $P(h_e|\alpha_e)$ , can be calculated by evaluating a normal distribution with mean  $\mu_{\alpha_e}$  and variance  $\sigma_{\alpha_e}^2$ :

$$P_e(h_e|\alpha_e) = \frac{1}{\sigma_{\alpha_e}\sqrt{2\pi}} \exp\left(-\frac{1}{2}\left(\frac{\alpha_e - \mu_{\alpha_e}}{\sigma_{\alpha_e}}\right)^2\right) \quad (3.4)$$

From assumption  $e_4$ , the prior probability,  $P_e(\alpha_e)$ , is  $\frac{1}{n_m}$  where  $n_m$  is the number of materials.

**Example dataset parameters.** The dataset parameters consist of the mean and variance of measurements of each discrete material.

We can calculate the posterior probability,  $P(\alpha_e|h_e)$ , for an instance of voxel-info,  $h_e$ , and a value of  $\alpha_e$  given values for the dataset parameters. From assumption  $e_3$  we find the dataset parameters by interactively selecting a set of points in the dataset for each material. We define each set as

measurements of the single material they represent; from them we calculate the mean and variance for each material.

**Example classification.** We iterate over each voxel calculating the most likely value for the single voxel parameter  $\alpha_e$ ; for each voxel we measure  $h_e$ , the value at the center of the voxel. For each possible material we calculate the corresponding posterior probability,  $P(\alpha_e|h_e)$ , and choose the largest of these values. This gives us the most likely material.

### 3.3 A Family of Solutions

In this section we give an overview of three new classification algorithms constructed within our framework to compare and contrast them with one another. The algorithms are described in detail in Chapters 4 and 5. We first list the assumptions that are common to all three algorithms and the dataset parameters that these assumptions imply. We then present the assumptions unique to each algorithm and summarize both the dataset and voxel parameters.

#### 3.3.1 Assumptions Common to New Algorithms

We make several assumptions that are consistent among the new algorithms that we have developed. Each algorithm also makes additional assumptions detailed in Sections 3.3.3–3.3.5.

$e_{c1}$ : **Discrete materials.** The first assumption is that materials within the objects that we measure are discrete at the resolution that we are sampling, but not necessarily aligned with the sampling grid. We make this assumption because we are generally looking for boundaries between materials, and because we are starting from sampled data, which loses information about detail that is finer than the sampling rate.

This assumption does not preclude homogeneous combinations of sub-materials that can be treated as a single material at our sampling resolution. For example, muscle may contain some water, and yet be treated as a separate material from water. This assumption is not

satisfied where materials gradually transition from one to another over many samples or are not relatively uniformly mixed. Section 4.8 discusses cases where this assumption is not satisfied.

$e_{c2}$ : **Normally distributed noise.** The second assumption is that noise is added to each discrete sample and that noise is normally distributed. We assume a different variance in the noise for each material. This assumption is not strictly satisfied for MRI data in some cases, but seems to be satisfied sufficiently to classify data well.

$e_{c3}$ : **Nyquist sampling theorem is satisfied.** The third assumption we make is that the sampled datasets we classify satisfy the Nyquist sampling theorem [Oppenheim et al., 1983]. The sampling theorem states that if we sample a sufficiently band-limited function, we can exactly reconstruct that function from the samples.

From assumption  $e_{c1}$  the underlying physical object has discontinuous boundaries between materials, and an infinite-precision MRI machine would generate a dataset with discontinuities at material boundaries. At finite resolutions, the measurement function must be band limited so that it can be reconstructed from the samples.

MRI slice data generally satisfies this assumption or can be pre-processed to satisfy it [Laidlaw, 1992b] within the slice. Without data that satisfy the Nyquist sampling theorem, we cannot reconstruct a continuous function, and without a continuous function, we cannot extract geometric models as described in Chapter 6.

### 3.3.2 Voxel-info: Histograms

For each of our classification techniques we use a histogram over the small region defined by a voxel to encode the information contained in the voxel. We first reconstruct a continuous function over the entire dataset from the samples and then use Equation. 4.1 to calculate a histogram over each voxel.

### 3.3.3 Overview of Algorithm A: Partial Volume Mixtures

Our new partial volume mixtures algorithm, described in more detail in Chapter 4, was developed to create classified data with fewer boundary artifacts so that we could produce better geometric models. The choice of voxel-info, the model of the voxel-info, and some of the assumptions are formulated to capture and identify information about the boundaries. The remainder of the assumptions help make some of the probability calculations more tractable.

#### Additions to common assumptions.

$e_{m4}$ : **Linear mixtures.** Each voxel measurement is a linear combination of pure material measurements and measurements of their pair-wise mixtures.

$e_{m5}$ : **Uniform tissue measurements.** Measurements for the same material have the same expected value throughout a dataset.

$e_{m6}$ : **Box filtering.** The spatial measurement process can be approximated by a box filter. This assumption contradicts  $e_{c3}$ , but helps us derive a tractable calculation for the histogram basis function for mixtures which appears to be accurate enough to classify data well.

$e_{m7}$ : **Materials identifiable in histogram of entire dataset.** The signatures for each material and mixture must be identifiable in a histogram of the entire dataset.

**Description.** The parameters for each voxel in this algorithm are density values for each pure material and for each pair-wise combination of materials and an estimate of the low-frequency noise within the voxel. The densities sum to one, and each density weights a histogram basis function for either a pure material or a mixture. The basis function for pure materials is a normal distribution. The basis function for a mixture is derived in Section 4.10. Both are shown in Figure 4.4.

The dataset parameters are the mean and variance values for each pure material, as well as an expected deviation of the model histogram from actual histograms. The parameters are estimated

by analyzing a histogram taken over the entire dataset and fitting a combination of materials to that histogram. See Chapter 4 for a complete description.

### 3.3.4 Overview of Algorithm B: Boundary Distance

Our new boundary distance algorithm, further described in Chapter 5, addresses some of the limitations we discovered in the partial volume mixtures algorithm. The voxel-info and most of the assumptions are the same, but the histogram basis functions are new. The main change is that the distance from a boundary is explicitly incorporated into the histogram basis function for mixtures. The explicit model better fits histograms of voxels near boundaries. A secondary change is that the histogram basis functions are derived with the more-accurate assumption of Gaussian filtering.

#### **Addition to common assumptions.**

$e_{b4}$ : **Only pair-wise mixtures.** Each voxel measurement is either a pure material or a mixture of exactly two materials near a boundary.

$e_{b5}$ : **Uniform tissue measurements.** Measurements for the same material have the same expected value throughout a dataset.

$e_{b6}$ : **Gaussian filtering.** The measurement process can be approximated by a Gaussian filter. This assumption helps us derive a tractable calculation for the new histogram model of boundary-parameterized mixtures and also models the actual collection process better than box filtering.

$e_{b7}$ : **Known materials.** We know the number of materials and can identify samples from each material and mixture within the data.

**Description.** The voxel parameters for this algorithm are a discrete parameter that determines the material or mixture, a signed distance from a boundary for mixtures, and an estimate of the low-frequency noise within the voxel. Once again, the histogram basis functions for pure materials



are normal distributions. The basis functions for mixtures are derived in Section 5.8.2 and are shown in Figures 5.2 and 5.3.

The dataset parameters are the mean and variance values for each pure material, as well as an expected deviation of the model histogram from actual histograms. They are estimated from a training set of points interactively chosen for each material and mixture. See Chapter 5 for a complete description.

### 3.3.5 Overview of Algorithm C: Boundary Distance with Non-Uniform Material Signatures

Our third new algorithm, further described in Chapter 5, augments the boundary distance algorithm to handle a common characteristic of MRI data that often complicates classification: MRI measurements of the same material that are different at different spatial locations. There are a number of factors that can cause these intensity distortions, from antenna coils that produce spatially dependent RF radiation to different amounts of absorption of the RF energy in different parts of the object. The algorithm relaxes the assumption that the expected value for a material is constant. Instead, the expected value is a function of spatial location.

**Additions to common assumptions.** Only  $e_{v5}$  differs from the assumptions for the boundary distance algorithm.

$e_{v4}$ : **Only pair-wise mixtures.** Each voxel measurement is either a pure material or a mixture of exactly two materials.

$e_{v5}$ : **Predictable tissue measurements.** Measurements for the same material have an expected value that can be modeled with a small number of parameters across a dataset.

$e_{v6}$ : **Gaussian filtering.** The measurement process can be approximated by a Gaussian filter. This assumption helps us derive a tractable calculation for the histogram model.

$e_{v7}$ : **Known materials.** We know the number of materials and can identify samples from each material and mixture within the data.

**Description.** This algorithm is very similar to the boundary distance algorithm. The basis functions and voxel parameters are the same. Only the dataset parameters that determine the expected value for a tissue measurement are different. In this case, the expected value is a parameterized function of space. Its parameters are calculated from a set of interactively-specified points for each material. The calculation is similar to calculating a mean and variance from a set of points, but the mean is now a function of spatial location.

### 3.4 Summary

We have presented a Bayesian framework for developing classification algorithms and have outlined three instances of algorithms. We describe the three algorithms in more detail in the following two chapters. Chapter 4 discusses the partial volume mixtures algorithm, provides more detail about the assumptions that it makes, describes the implementation, and presents the results. Chapter 5 does the same for the two boundary distance algorithms.

## Chapter 4

---

# Bayesian Classification Algorithm A: Partial Volume Mixtures

---

In this chapter we describe a new classification technique. We follow the framework presented in Chapter 3, first describing the construction of the classification technique and then describing the implementation that classifies each voxel.

The algorithm uses the probability estimates to classify each voxel in a sampled dataset. The first step estimates basis-function parameters applicable to the entire dataset. The second step estimates basis-function parameters for each voxel using the dataset parameters and the probability estimates and then classifies each voxel based on the estimates.

The input to our process is sampled measurement data, from which we reconstruct a continuous, band-limited function  $\rho(x)$  that measures distinguishing properties of the underlying materials. Our unit of voxel-info is a histogram of  $\rho(x)$  taken over a small region. The output is sampled data measuring the relative volume of each material. We call the output “material volume ratio densities” (see Figure 4.2).

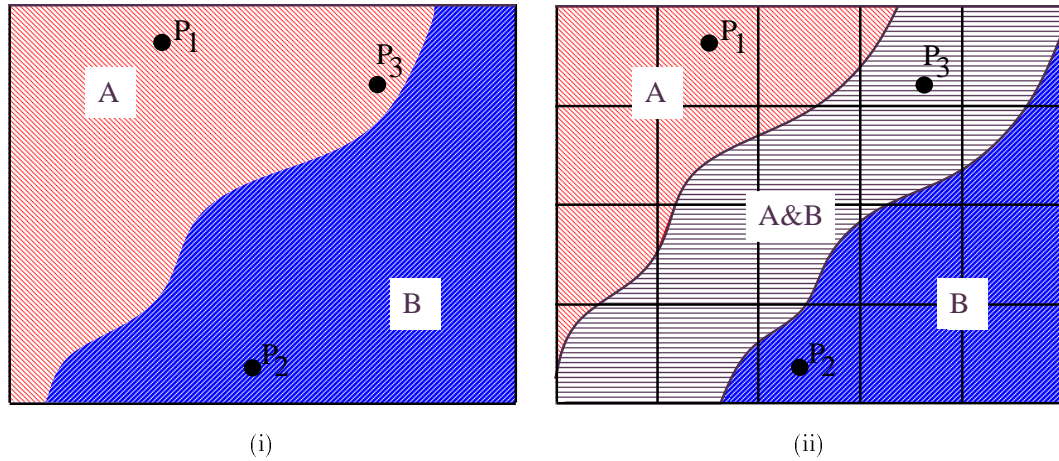


Figure 4.1: We start from the assumption that in a real-world object each point is exactly one material, as in (i). The measurement process creates samples that mix materials together, from which we reconstruct a continuous, band-limited measurement function  $\rho(x)$ . For some values of  $x$ , e.g.,  $P_1$  and  $P_2$ ,  $\rho(x)$  returns the signature of a pure material. For other values of  $x$ , e.g.,  $P_3$ ,  $\rho(x)$  returns a combination of the pure material signatures. (ii) shows regions A and B where  $\rho(x)$  returns pure material signatures and region A&B, where  $\rho(x)$  returns a combination. The grid lines show how the material regions may span voxels.  $\square$

We assume, as in Figure 4.1, that each voxel is a mixture of materials, with mixtures like A & B occurring where the band-limiting effects of the data collection process blur pure materials together. From this assumption we derive basis functions that model histograms for pure materials and for mixtures of two materials.

We give an overview of the construction of the algorithm in Section 4.1 and of the implementation in Section 4.2. Sections 4.3 and 4.4 give more details on histograms and the basis functions for modeling them, and Sections 4.5 and 4.6 describe estimating dataset and voxel parameters. We present results in Section 4.7 and discuss the results and algorithm in Section 4.8. Detailed derivations follow in Sections 4.10 and 4.11.

## 4.1 Construction

The construction of the algorithm starts with a choice of voxel data and a set of assumptions and proceeds through a derivation of basis functions to match a model to the voxel data. This section describes the construction process.

### 4.1.1 Voxel-info

As we described in Section 3.2.1, our algorithm uses histograms over voxel regions to represent the information contained in a voxel.

### 4.1.2 Assumptions

**A sample measures a combination of materials.** A simplifying assumption of some previous techniques is that each sample represents a measurement of one material, rather than a combination of materials. Because the data-collection process blends measurements of more than one material at points near boundaries, this assumption is not always satisfied (see Figure 4.1).

[Drebin et al., 1988] mention the need for mixture classification. They approximate the relative volume of a material represented by a sample with the probability that the sample is the material. As they point out, this works reasonably well for differentiating air, soft tissue, and bone in CT data, but not in general. In MRI data the expected data value for one material may often be identical to the expected value for a mixture of two other, different materials. We address this problem below.

We make the following assumptions about the measurement function,  $\rho(x) : \mathbf{R}^3 \rightarrow \mathbf{R}^{n_v}$ , and about the collection process.  $n_v$  is the dimensionality of our data. The assumptions are described in detail in Sections 3.3.1 and 3.3.3.

$e_{c1}$ : **Discrete materials.**

$e_{c2}$ : **Normally distributed noise.**

$e_{c3}$ : **Nyquist sampling theorem is satisfied.**

$e_{m4}$ : **Linear mixtures.**

$e_{m5}$ : **Uniform tissue measurements.**

$e_{m6}$ : **Box filtering.**

$e_{m7}$ : **Materials identifiable in histogram of entire dataset.**

For many types of medical imaging data, including MRI and CT, these assumptions hold reasonably well, or can be satisfied sufficiently with preprocessing [Laidlaw, 1992a]. Other types of sampled data, e.g., ultrasound and sequences of video or film images with lighting and shading, violate these assumptions, and our technique does not apply directly.

### **4.1.3 Sketch of Derivation**

As shown in Figure 4.1 we start with the assumption that each spatial location in the real world object is exactly one material, and that the measurement process mixes materials together as it band limits the measurements to the Nyquist frequency of the sampling rate. From that assumption we will derive (in Section 4.3) an equation for a normalized histogram of data values within a region. This histogram function is a probability density function (PDF) that tells us the probability that a measurement will lie within a range of values in that region.

In Section 4.10 we create basis functions to model histograms. These basis functions are parameterized probability density functions for regions consisting of single materials and for regions consisting of mixtures of two materials. These mixtures are assumed to have been created by the band-limiting process accompanying sampling. The parameters represent the mean value,  $c$ , and variance,  $s$ , of a measurement.

Using Bayes' Theorem, the histogram of the entire dataset, our model basis functions, and a series of approximations, we derive an estimate of the most likely set of materials within an entire dataset (Section 4.11). Similarly, given the histogram of a voxel region, we derive an estimate of the most likely density for each material in that region (Section 4.6).

## **4.2 Algorithm**

The algorithm produces, as its end result, a sampled dataset containing estimates of material volume ratio densities. The process is illustrated in Figure 4.2.

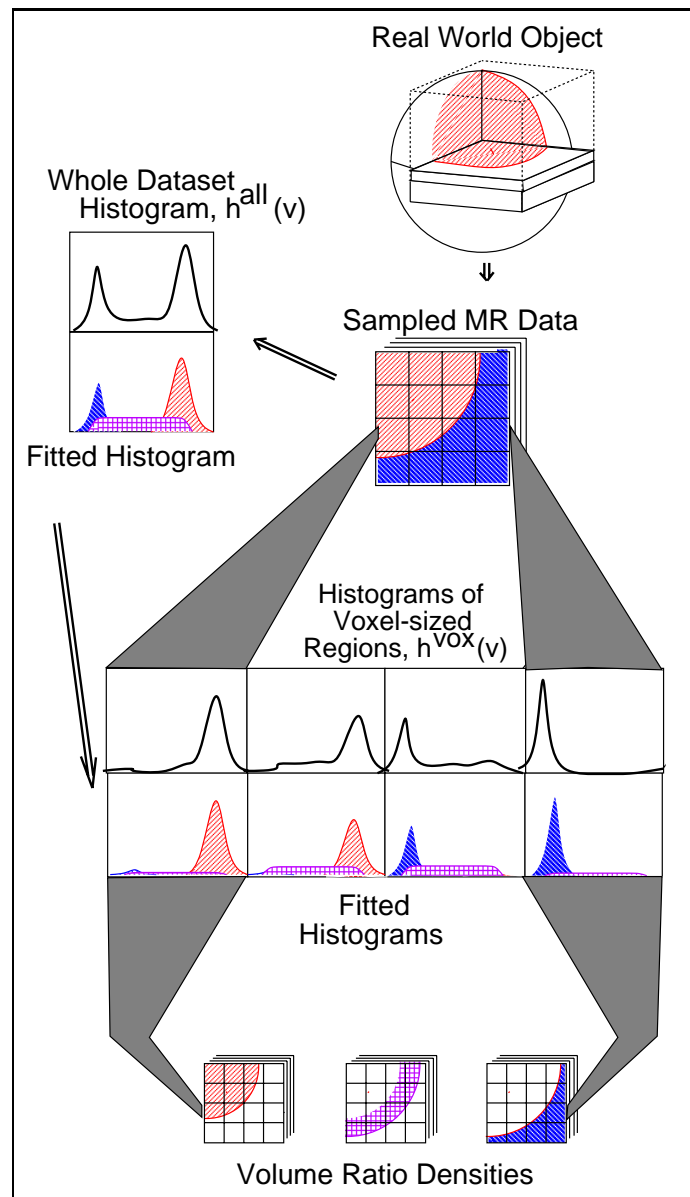


Figure 4.2: Steps in the classification process. We collect MR data, calculate a histogram of the entire dataset,  $h^{\text{all}}(v)$ , and use that to determine parameters of histogram-fitting basis functions. We then calculate histograms of each voxel region,  $h^{\text{VOX}}(v)$ , and identify the most likely mixture of materials for that region. The result is a sampled dataset of volume ratio densities.  $\square$

**Estimating dataset parameters.** First, we collect and preprocess data to satisfy the assumptions listed above. Second, we calculate a histogram of the entire dataset, and fit parameterized material probability density functions to the histogram to get an estimate of basis function parameters that are constant throughout the dataset.

**Estimating voxel parameters.** Using the fitted parameters, we process the region for each voxel in the dataset as follows. We first calculate a histogram for the small region and find the combination of materials most closely fitting the histogram. Using the estimated parameters, we calculate material volume ratio densities for that small region.

### 4.3 Normalized Histograms

In this section we present the equation for a normalized histogram of a sampled dataset over a region. We will use this equation as a building block in several later sections, with regions that vary from the size of a single voxel to regions covering the entire dataset. We will also use this equation to derive basis functions that model histograms over regions containing single materials and regions containing mixtures of materials. Figure 4.3 shows an example of calculating a normalized histogram from a continuous function.

For a given region in spatial coordinates, specified by  $\mathcal{R}$ , the histogram  $h^{\mathcal{R}}(v)$  specifies the relative portion of that region where  $\rho(x) = v$ . We define histograms,  $h^{\mathcal{R}}(v) : \mathbf{R}^{nv} \rightarrow \mathbf{R}$ , as probability density functions (PDFs). These histograms over regions are also continuous functions:

$$h^{\mathcal{R}}(v) = \int \mathcal{R}(x)\delta(\rho(x) - v)dx \quad (4.1)$$

This equation is the continuous analog of a discrete histogram.  $\mathcal{R}(x)$  is non-zero within the region of interest, and integrates to 1. We define  $\mathcal{R}(x)$  to be constant in the region of interest making every spatial point contribute equally to the histogram  $h^{\mathcal{R}}(v)$ . Note also that  $h^{\mathcal{R}}(v)$  integrates to 1, which is important for our interpretation as a PDF.  $\delta$  is the Dirac-delta function.

We use this equation both as a starting point for deriving material intensity PDFs, and also as a basis for calculating histograms of regions of our datasets. The derivations are outlined in the following two sections and detailed in Section 4.10. We will now discuss a few implementation considerations for calculating histograms.



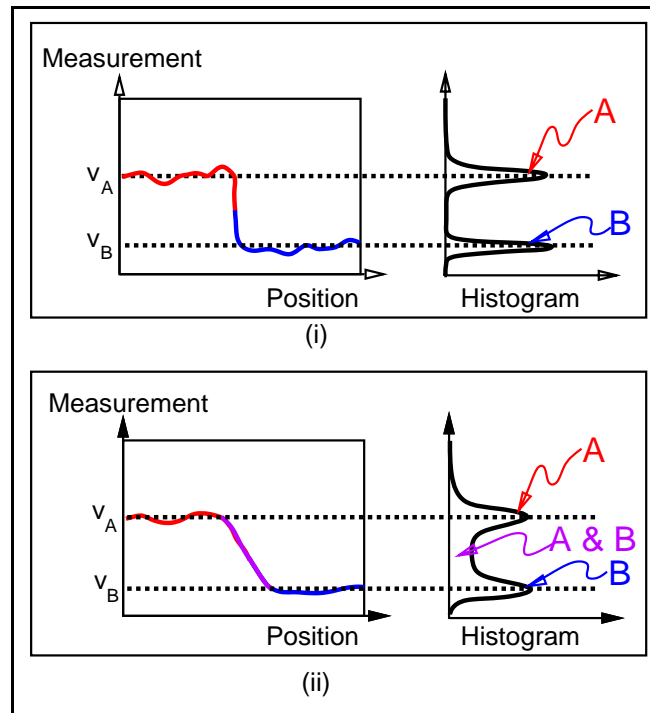


Figure 4.3: Noise and mixtures in histograms. The scalar data on the left represent measurements from a dataset containing two materials,  $A$  and  $B$ , such as that shown in Figure 4.1. One material has measurement values near  $v_A$  and the other near  $v_B$ . These values correspond to the Gaussian-shaped peaks centered around  $v_A$  and  $v_B$  in the histograms, which are shown on their sides to emphasize the axis that they share. *Feature space* lies along this axis. In (i) we show a histogram of a function that has not been band limited, but does have noise. In (ii) the function has been band limited, and the measurement transition between  $v_A$  to  $v_B$  now appears in the histogram as the flat region between feature space values  $v_A$  and  $v_B$ . The process extends to higher dimensions.  $\square$

**Implementation Considerations.** For each voxel we calculate a histogram during the classification process. We describe the histogram calculation briefly. We calculate histograms in rectangular *bins*, sized such that the width of a bin is smaller than the standard deviation of the noise within the dataset. This ensures that we do not lose significant features in the histogram.

We calculate a histogram iteratively, first initializing the bins to zero. For the region of each voxel in the dataset we use the first terms of the Taylor series of  $\rho(x)$  to create a linear approximation of  $\rho(x)$  over the region. We then calculate a piecewise-constant approximation of the histogram over that region, and add that to the bins. The histogram approximation is obtained by substituting the linearized version of  $\rho(x)$  into Equation 4.1 and integrating that over the small regions. This takes into account correlation of values between different elements of vector data.

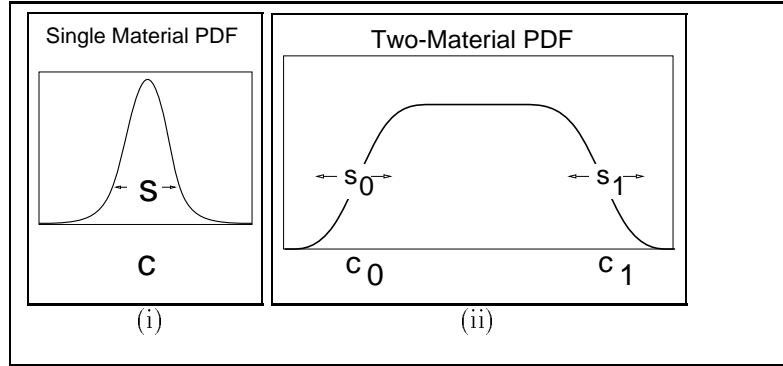


Figure 4.4: Dataset parameters for a single material PDF, shown in (i) include  $c$ , the mean value for the material, and  $s$ , which measures the variance of the noise (see Equation 4.2). (ii) shows corresponding parameters for a two-material mixture basis function.  $s_0$  and  $s_1$  affect the slopes of the two-material PDF at either end. For vector-valued data  $c$  and  $s$  are vectors and are the mean values and variances of the noise for the two constituent materials (see Equation 4.3).  $\square$

#### 4.4 Histogram Basis Functions for Pure Materials and Mixtures

In this section we present definitions of basis functions that model histograms of pure materials and of material mixtures. These basis functions are PDFs that specify the probability that a sample lies within a range of values given that it is a particular material or mixture. The parameters of the basis functions specify the expected value,  $c$ , and variance,  $s$ , of each material's measurements (see Figure 4.4).

We use Equation 4.1 to derive these basis functions, which we fit to the data. We then verify that the equations provide reasonable fits to typical MRI data, which gives us confidence that our assumptions about the measurement function  $\rho(x)$  were reasonable. The details of the derivations are in Section 4.10.

For a single material, the PDF is a normal distribution:

$$f_{\text{single}}(v; c, s) = \prod_{i=1}^{n_v} \frac{1}{s_i \sqrt{2\pi}} \exp\left(-\frac{1}{2} \left(\frac{v_i - c_i}{s_i}\right)^2\right) \quad (4.2)$$

We derive this equation by manipulating Equation 4.1 evaluated over a region of constant material, where the measurement function  $\rho(x)$  is a constant value plus additive, normally distributed noise.

For mixtures along a boundary between two materials, we derive another equation similarly. As with the single material, this derivation follows from Equation 4.1 evaluated over a region where two

materials mix. In this case, we approximate the band-limiting filter of the data-collection process with a box filter, and make the assumption that the variance of the additive noise is constant across the region. This basis function is a superposition of normal distributions representing different amounts of the two constituent mixtures:

$$f_{\text{double}}(v; c, s) = \int_0^1 f_{\text{single}}(v; (1-t)c_1 + tc_2, s) dt \quad (4.3)$$

where  $c_1$  and  $c_2$  are the expected values of the two materials, and  $s$  the variance of measurements.

The assumption of a box filter affects the shape of the resulting PDF. We derived similar equations for different filters (triangle, Gaussian, and Hamming), but chose the box filter derivation because we found it sufficiently accurate in practice and because the numerical tractability of the PDF in this case saved computation.

## 4.5 Estimating Dataset Parameters

In this section we describe the parameter estimation procedure for fitting material intensity PDFs to a dataset. For a given dataset we first calculate the histogram,  $h^{\text{all}}(v)$ , of the entire dataset.

We then combine an interactive process of specifying the number of materials and approximate feature-space locations for them with an automated optimization to estimate the parameters. Under some circumstances, users may wish to group materials with similar measurements into a single “material,” whereas in other cases they may wish the materials to be separate. The result of this process is a set of PDFs that describe the various materials and mixtures of interest in the dataset.

The optimization process estimates the relative volume of each material (vector  $\alpha^{\text{all}}$ ), the mean value (vector  $c$ ), and the variance (vector  $s$ ) of measurements of each material. The process is derived from the assumption that all values were produced by pure materials and two-material mixtures. We define  $n_m$  as the number of pure materials in a dataset and  $n_f$  as the number of material intensity PDFs.  $n_f \geq n_m$ , since  $n_f$  includes any material intensity PDF’s for mixtures, as well as those for pure materials.

The optimization minimizes the function

$$\mathcal{E}(\alpha^{\text{all}}, c, s) = \int \left( \frac{q(v; \alpha^{\text{all}}, c, s)}{w(v)} \right)^2 dv \quad (4.4)$$

where:

$$q(v; \alpha^{\text{all}}, c, s) = h^{\text{all}}(v) - \sum_{j=1}^{n_f} \alpha_j^{\text{all}} f_j(v; c_j, s_j) \quad (4.5)$$

The function  $q(v)$  is analogous to the difference between the expected histogram and the measured histogram. The function  $w(v)$  is analogous to a deviation at each point  $v$  in feature space, and gives the expected value of  $|q(v)|$ . We approximate  $w(v)$  as a constant, and discuss it further in Section 4.8.

These equations are derived in Section 4.11, using Bayesian probability theory with estimates of prior and conditional probabilities.

## 4.6 Classification: Estimating Voxel Parameters

In this section we describe the process of classifying each voxel. This process is similar to that described in Section 4.11 for fitting the material PDFs to the entire dataset, but now we operate on each voxel region. We use the previously computed material PDFs as fixed basis functions and no longer vary the mean vector  $c$  and variance  $s$ . The only voxel parameters are the relative material volumes (vector  $\alpha_j^{\text{vox}}$ ) and an estimate of the local noise in the local region (vector  $\bar{N}$ ) (see Equations 4.6 and 4.7).

Over large regions the noise is normally distributed with zero mean. However, for small regions the mean noise is generally non-zero due to the band limiting introduced in the data-collection process. We label this local mean voxel noise value  $\bar{N}$ . As derived in Section 4.11 the equation that we minimize is:

$$\mathcal{E}(\alpha^{\text{vox}}, \bar{N}) = \sum_{i=1}^{n_v} \left( \frac{\bar{N}_i}{\sigma_i} \right)^2 + \int \left( \frac{q(v; \alpha^{\text{vox}}, \bar{N})}{w(v)} \right)^2 dv \quad (4.6)$$

Object	Source	Voxel Size	Figures
spherical shells	simulated	1x1x10 mm	Figure 4.5
human hand	GE 1.5T	0.7x0.7x3 mm	Figure 3.1, Figure 4.9
human brain	GE 1.5T	0.8x0.8x3 mm	Figure 4.6, Figure 4.7

Table 4.1: Dataset shown in examples with some collection parameters.  $\square$

where

$$q(v; \alpha^{\text{vox}}, \bar{N}) = h^{\text{vox}}(v - \bar{N}) - \sum_{j=1}^{n_f} \alpha_j^{\text{vox}} f_j(v) \quad (4.7)$$

and subject to the constraints

$$0 \leq \alpha_j^{\text{vox}} \leq 1, \text{ and } \sum_{j=1}^{n_f} \alpha_j^{\text{vox}} = 1.$$

Vector  $\sigma$  is the expected variance of the noise over the entire dataset. We estimate this as an average of the variances of the material intensity PDFs.

With vector  $\alpha^{\text{vox}}$  for a given voxel region and the mean value, vector  $\bar{v}$ , within that region, we solve for the amount of each pure material contributed by each mixture to the voxel. This is our output, the estimates of the amount of each pure material in the voxel region.

## 4.7 Results

We have applied our new technique to several datasets. Table 4.1 lists the datasets, their sources, the voxel size, and the figures in which each dataset appears. All datasets were collected with a spin-echo or fast spin-echo protocol, with one proton-weighted and one  $T_2$ -weighted acquisition.

In Figs. 4.5, 4.6, and 4.7 we compare our technique with a probabilistic approach that uses pure materials only and only a single measurement value per voxel. The new technique produces many fewer misclassified voxels, particularly in regions where materials are mixed due to filtering. In Figure 4.5(iii) and (iv) the difference is particularly noticeable where an incorrect layer of background material has been introduced between the white and red regions, where multiple materials are present in the same voxel. Figures 4.6 and 4.7(iii) also show comparative results between the

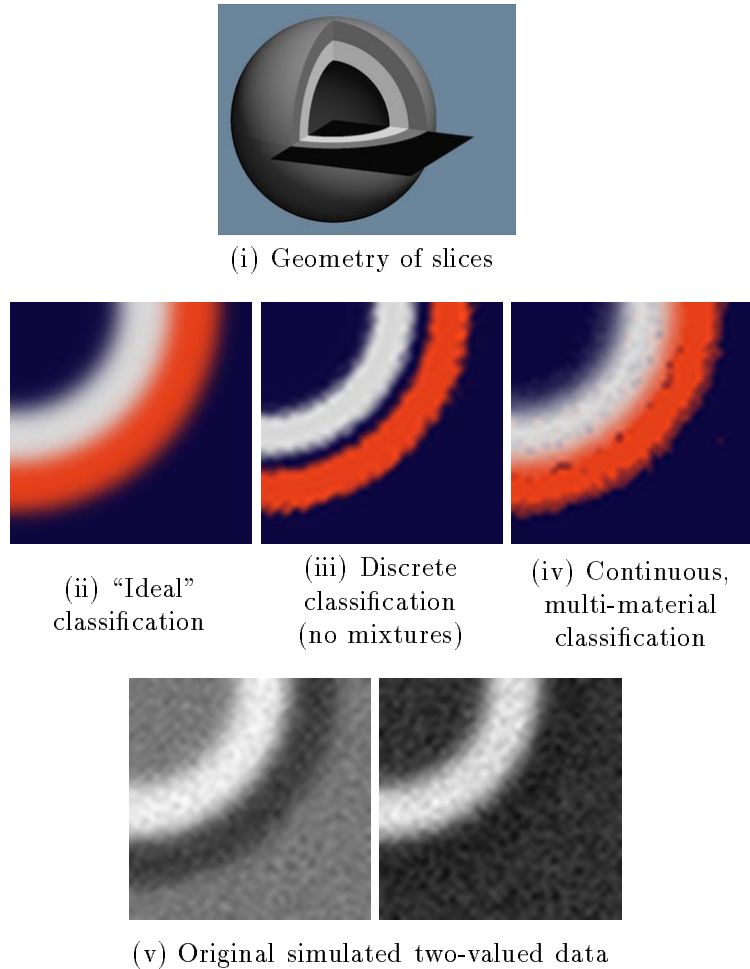


Figure 4.5: Comparison of discrete, single-material classification (iii), and the new classification (iv). (ii) is a reference for what "ideal" classification should produce. Note the band of background material in (iii) between the two curved regions. This band is incorrectly classified and could lead to errors in models or images produced from the classified data. The original dataset, (v), is simulated, two-valued data of two concentric shells as diagramed in (i). □

two methods.

Models and volume rendered images, as shown in Figure 4.9, also benefit because less incorrect information is introduced into the classified datasets, and so the images and models more accurately depict the objects they are representing. With other classification techniques, models and images contain jaggy artifacts along surfaces where materials meet.

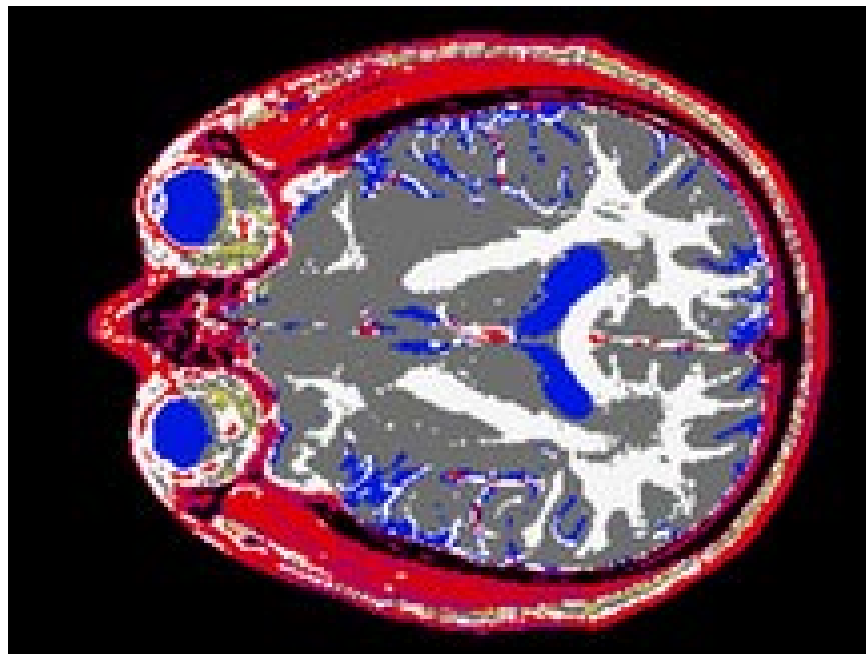


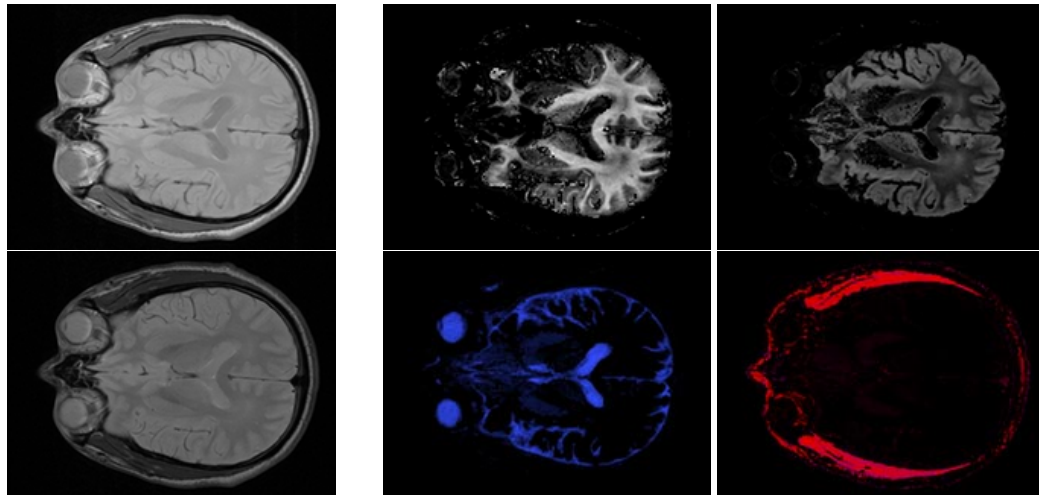
Figure 4.6: Discrete, single-material classification of the same slice shown in Figure 4.7. □

**Implementation.** Our implementation is written in C and C++ on Unix workstations. We use a sequential quadratic programming constrained optimization algorithm [NAG, 1993] to fit  $h^{\text{vox}}$  for each voxel region, and a quasi-Newton optimization algorithm for fitting  $h^{\text{all}}$ . The algorithm classifies approximately 10 voxels per second on a single HP9000/730, IBM RS6000/550E, or DEC Alpha AXP 3000 Model 500 workstation. We have implemented this algorithm in parallel on these machines, and get a corresponding speedup on multiple machines.

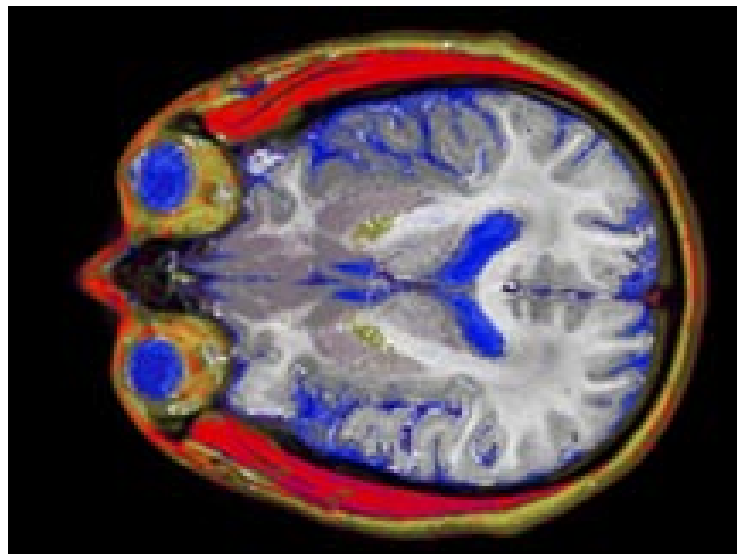
## 4.8 Discussion

We have made several assumptions and approximations while developing and implementing this algorithm. This section will discuss some of the tradeoffs and suggest some possible directions for future work.

**Mixtures of Three or More Materials.** We assume that each measurement contains values from at most two materials, although our approach easily extends to mixtures with more materials.



(i) Original Data

(ii) Results of Algorithm  
Classified White Matter (white), Gray Matter (gray)  
Cerebro-Spinal Fluid (blue), Muscle (red)

(iii) Combined Classified Image

Figure 4.7: One slice of data from a human brain. (i) shows the original two-valued data, (ii) shows four of the identified materials, white matter, gray matter, cerebro-spinal fluid, and muscle, separated out into different images, and (iii) shows the results of the new classification mapped to different colors. Note the smooth boundaries where materials meet and the much lower incidence of misclassified samples than in Figure 4.6.  $\square$



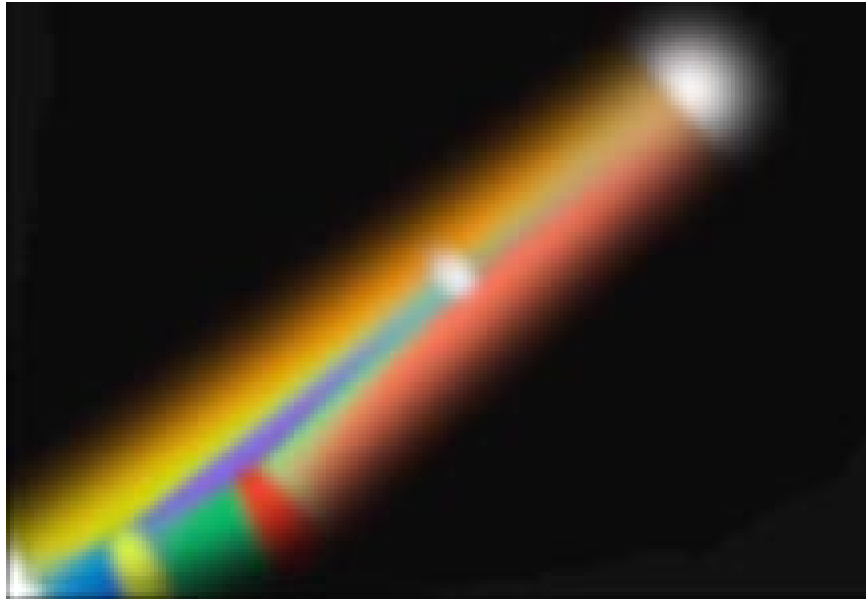


Figure 4.8: Basis functions fit to histogram of human hand dataset. The bottom and left edges of the image are axes for each MRI value, with the intensity of the image representing the height of the histogram function. Bright spots are pure materials, while the lines connecting the dots are mixtures. The rightmost two white dots are pure fat and bone marrow in the hand. The lower yellow and red dot are pure skin and muscle, respectively. The mixture between muscle (red) and fat (white) is a salmon colored streak. The green streak between the red and yellow dots is a mixture of skin and muscle. These fitted basis functions were used to produce the classified data used in Figure 4.9 □



Figure 4.9: A volume-rendering image of a human hand dataset. The opacity of different materials is decreased above cutting planes to show details of the classification process within the hand. □

We chose two-material mixtures because surfaces between boundaries of pure materials are one of the most important parts of computer graphics models. Voxels containing three-material mixtures happen near lines where three materials meet, and are generally much less common, because the dimensionality of the lines is smaller than the dimensionality of surfaces where two materials meet.

Our algorithm chooses a classification for voxels containing more than two materials from the set of 2-material mixtures. Generally, the two largest materials in the voxel influence the choice, producing a dataset with small artifacts where three or more materials come together.

**Partial Mixtures.** We note that the histograms  $h^{\text{vox}}(v)$  for some voxel regions are not ideally matched by a linear sum of basis functions. We address two problems here.

The first problem is that, within a small region, the assumption that we still have normally distributed noise is no longer valid.  $\bar{N}$  models the fact that the noise no longer averages to zero, but we do not attempt to model the change in the shape of the distribution as the region size shrinks.

The second problem is related. A small region may not contain the full range of values that the mixture of materials can produce. As a result, the histogram over that small region is not modeled ideally by a linear combination of pure material and mixture distributions. We investigate an additional parameter to address this problem in Chapter 5.

We postulate that these two effects weight the optimization process such that it tends to make  $\bar{N}$  much larger than we expect. As a result, we have found that setting the normalization factor,  $w(v)$ , to approximately 30 times the maximum value in  $h^{\text{vox}}(v)$  gives good classification results. Smaller values tend to allow  $\bar{N}$  to move too much, and larger values hold it constant. Without these problems we would expect the algorithm to work best for values of  $w(v)$  equal to some small percentage of the maximum of  $h^{\text{vox}}(v)$ . Once again, we address this problem more effectively in Chapter 5.

## 4.9 Conclusion

We have developed a new classification algorithm within the Bayesian framework described in Chapter 3. The new algorithm uses histograms taken over small voxel regions to represent the information within a voxel, and models these histograms as a linear combination of basis functions for pure materials and for mixtures of materials. The pure material basis function is a normal distribution, but the mixture basis function is new and is derived in Section 4.10. The new algorithm classifies MRI data better than previous algorithms, especially near boundaries between materials, because the histogram incorporates more information about the voxel than a single measurement and because the histogram model explicitly incorporates boundaries between materials.

---

## 4.10 Derivation of Material PDFs

In this section we derive material PDFs that we use as basis functions ( $f_i$ ) for fitting histograms. We derive two forms of basis functions: one for single, pure materials and another for two-material mixtures (which arise due to sampling). Here is Equation 4.1, the histogram equation:

$$h^{\mathcal{R}}(v) = \int \mathcal{R}(x)\delta(\rho(x) - v)dx \quad (4.8)$$

Note that if  $\rho(x)$  contains additive noise  $n(x; s)$  with a particular distribution  $k_n(v; s)$ , then the histogram of  $\rho$  with noise is the convolution in  $v$  of the normal distribution  $k_n(v; s)$  with  $\rho(x) - n(x; s)$  (i.e,  $\rho(x)$  without noise). We represent the convolution in  $v$  with the operator  $*_v$ . Thus

$$\begin{aligned} h^{\mathcal{R}}(v) &= \int \mathcal{R}(x)\delta(\rho(x) - v)dx \\ h^{\mathcal{R}}(v) &= k_n(v; s) *_v \int \mathcal{R}(x)\delta((\rho(x) - n(x; s)) - v)dx \end{aligned} \quad (4.9)$$

### 4.10.1 Pure Materials

For a single pure material we assume that the measurement function has the form:

$$\rho_{\text{single}}(x) = c + n(x; s), \quad (4.10)$$

where  $c$  is the constant expected value of a measurement of the pure material, and  $n(x; s)$  is the normally distributed noise at  $x$  with variance  $s$ .

The basis function we use to fit the histogram of the measurements of a pure material is

$$\begin{aligned} f_{\text{single}}(v; c, s) &= \int \mathcal{R}(x) \delta(\rho_{\text{single}}(x) - v) dx \\ &= \int \mathcal{R}(x) \delta(c + n(x; s) - v) dx \\ &= k_n(v; s) * \int \mathcal{R}(x) \delta(c - v) dx \\ &= \prod_{i=1}^{n_v} \frac{1}{s_i \sqrt{2\pi}} \exp\left(-\frac{1}{2} \left(\frac{v_i - c_i}{s_i}\right)^2\right) \end{aligned} \quad (4.11)$$

Thus  $f_{\text{single}}(v; c, s)$  is a normal distribution with mean  $c$  and variance  $s$ . We assume the noise is independent in each element of vector-valued data, which for MRI appears to be reasonable.

### 4.10.2 Mixtures

For a mixture of two pure materials, we assume the measurement function has the form:

$$\rho_{\text{double}}(x) = \ell_{\text{double}}(x; c_1, c_2) + n(x; s) \quad (4.12)$$

where  $\ell_{\text{double}}$  approximates the band-limiting filtering process, a convolution with a box filter, by interpolating the values within the region of mixtures linearly between  $c_1$  to  $c_2$ , the mean values for the two materials.

$$\begin{aligned}
f_{\text{double}}(v; c, s) &= \int \mathcal{R}(x) \delta(\rho_{\text{double}}(x) - v) dx \\
&= \int \mathcal{R}(x) \delta(\ell_{\text{double}}(x; c_1, c_2) + n(x; s) - v) dx \\
&= k_n(v; s) * \int \mathcal{R}(x) \delta(\ell_{\text{double}}(x; c_1, c_2) - v) dx \\
&= \int_0^1 k_n(v; s) * \delta((1-t)c_1 + tc_2 - v) dt \\
&= \int_0^1 k_n((1-t)c_1 + tc_2 - v; s) dt
\end{aligned} \tag{4.13}$$

## 4.11 Derivation of Classification Parameter Estimation

In this section we derive the equations that we optimize to find material PDF parameters and to classify voxel regions. We use Bayesian probability theory [Loredo, 1989] to derive an expression for the probability that a given histogram was produced by a particular set of parameter values in our model. We maximize an approximation to this “posterior probability” to estimate the best fit parameters:

$$\text{maximize } P(\text{parameters} \mid \text{histogram}) \tag{4.14}$$

We use this optimization procedure for two purposes:

- **Find material PDF parameters.** Initially, we find parameters of basis functions to fit histograms of the entire dataset  $h^{\text{all}}$ . This gives us a set of basis functions that describe the pure materials and mixtures.
- **Classify voxel regions.** We fit a weighted sum of the basis functions to the histogram of a voxel region  $h^{\text{vox}}$ . This gives us our classification in terms of the weights,  $\alpha$ .

The posterior probabilities  $P^{\text{all}}$  and  $P^{\text{vox}}$  share many common terms. In the following derivation we distinguish them only where necessary, using  $P$  where their definitions coincide.

### 4.11.1 Definitions

Tables 4.2 and 4.3 list definitions that we use in the following derivations.

Term	Dimensionality	Definition
$n_f$	scalar	number of materials and mixtures
$n_v$	scalar	dimensions of measurement (feature space)
$\alpha$	$n_f$	relative volume of each mixture and material within the region
$c$	$n_f \times n_v$	mean of material measurements for each material
$s$	$n_f \times n_v$	variance of material measurements for each material
$\bar{N}$	$n_v$	mean value of noise over the region
$p_{1..6}$	scalars	arbitrary constants
$h^{\text{all}}(v)$	$\mathbf{R}^{n_v} \rightarrow \mathbf{R}$	histogram of an entire dataset
$h^{\text{vox}}(v)$	$\mathbf{R}^{n_v} \rightarrow \mathbf{R}$	histogram of a tiny, voxel region

Table 4.2: Definitions used in derivations.  $\square$ 

Probabilities (using Bayesian terminology [Loredo, 1989]):	
$P(\alpha, c, s, \bar{N} h)$	posterior probability (we maximize this)
$P(\alpha, c, s, \bar{N})$	prior probability
$P(h \alpha, c, s, \bar{N})$	likelihood
$P(h)$	global likelihood

Table 4.3: Probabilities (using Bayesian probability terminology [Loredo, 1989])  $\square$ 

### 4.11.2 Optimization

We perform the following optimization to find the best fit parameters:

$$\text{maximize } P(\alpha, c, s, \bar{N}|h) \quad (4.15)$$

With  $P \equiv P^{\text{all}}$ , we fit material PDF parameters  $c, s, \alpha^{\text{all}}$  to the histogram of an entire dataset  $h^{\text{all}}(v)$ . With  $P \equiv P^{\text{vox}}$ , we fit  $\alpha^{\text{vox}}, \bar{N}$  to classify the histogram of a voxel region  $h^{\text{vox}}(v)$ .

### 4.11.3 Derivation of the posterior probability $P(\alpha, c, s, \bar{N}|h)$

We start with Bayes' Theorem, expressing the posterior probability in term of the likelihood, the prior probability, and the global likelihood.

$$P(\alpha, c, s, \bar{N}|h) = \frac{P(\alpha, c, s, \bar{N})P(h|\alpha, c, s, \bar{N})}{P(h)} \quad (4.16)$$

Each of the terms on the right-hand side is approximated below, using  $p_{1...6}$  to denote constants (which can be ignored during the optimization process).

**Prior Probabilities.** We assume that  $\alpha$ ,  $c$ ,  $s$  and  $\bar{N}$  are independent, so

$$P(\alpha, c, s, \bar{N}) = P(\alpha)P(c, s)P(\bar{N}) \quad (4.17)$$

Because the elements of  $\alpha$  represent relative volumes, we require that they sum to 1 and are positive.

$$P(\alpha) = \begin{cases} 0 & \text{if } \sum_{j=1}^{n_f} \alpha_j \neq 1 \\ 0 & \text{if } \alpha_j < 0 \text{ or } \alpha_j > 1 \\ p_1 & \text{(constant) otherwise} \end{cases} \quad (4.18)$$

We use a different assumption for  $P(c, s)$  depending on whether we are fitting  $h^{\text{all}}$  or  $h^{\text{vox}}$ . For fitting  $h^{\text{all}}(v)$ , we consider all values of  $c, s$  equally likely

$$P^{\text{all}}(c, s) = p_6 \quad (4.19)$$

For fitting  $h^{\text{vox}}$ ,  $c, s$  are fixed at  $c^0, s^0$  (the values determined by the earlier fit to the entire data set).

$$P^{\text{vox}}(c, s) = \delta(c - c^0, s - s^0) \quad (4.20)$$

For a small region, we assume that the noise vector,  $\bar{N}$ , has normal distribution with variance  $\sigma$ .

$$P^{\text{vox}}(\bar{N}) = p_2 e^{-\sum_{i=1}^{n_v} (\frac{\bar{N}_i}{\sigma_i})^2} \quad (4.21)$$

For a large region, the mean noise  $\bar{N}$  should be very close to zero and hence  $P^{\text{all}}(\bar{N})$  will be a delta

function at  $\bar{N} = 0$ .

$$P^{\text{all}}(\bar{N}) = \delta(0) \quad (4.22)$$

**Likelihood.** We approximate the likelihood  $P(h|\alpha, c, s, \bar{N})$  by analogy to a discrete normal distribution. We define  $q(v)$  to measure the difference between the expected histogram for particular  $\alpha, c, s, \bar{N}$  and a given histogram  $h(v)$

$$q(v; \alpha, c, s, \bar{N}) = h(v - \bar{N}) - \sum_{j=1}^{n_f} \alpha_j f_j(v; c, s) \quad (4.23)$$

Now we create a function by analogy to a normal distribution.  $w(v)$  is analogous to the variance of  $q$  at each point of feature space.

$$P(h|\alpha, c, s, \bar{N}) = p_3 e^{-\frac{1}{2} \int \left( \frac{q(v; \alpha, c, s, \bar{N})}{w(v)} \right)^2 dv} \quad (4.24)$$

**Global Likelihood.** Note that the denominator of Equation 4.16,  $P(h)$  is constant. It normalizes the numerator.

### Assembly of Terms.

Using the approximations discussed above, we arrive at the following expression for the posterior probability:

$$P(\alpha, c, s, \bar{N}|h) = p_5 P(\alpha) P(c, s) \left( e^{-\sum_{i=1}^{n_v} \left( \frac{\bar{N}_i}{\sigma_i} \right)^2} \right) \left( e^{-\int \left( \frac{q(v; \alpha, c, s, \bar{N})}{w(v)} \right)^2 dv} \right) \quad (4.25)$$

For fitting  $h^{\text{all}}$ , the mean noise is assumed to be zero. The coefficient of the exponential are constant with respect to the parameters, so maximizing Equation 4.25 is equivalent to minimizing



the argument of the exponential to find the free parameters  $(\alpha^{\text{all}}, c, s)$ :

$$\mathcal{E}^{\text{all}}(\alpha^{\text{all}}, c, s) = \int \left( \frac{q(v; \alpha^{\text{all}}, c, s)}{w(v)} \right)^2 dv \quad (4.26)$$

subject to  $P(\alpha^{\text{all}}) \neq 0$ .

For fitting  $h^{\text{vox}}$ , the parameters  $c$  and  $s$  are fixed. Once again, the coefficients of the exponential are constant with respect to the parameters, so maximizing Equation 4.25 is equivalent to minimizing the argument of the exponential to find the free parameters  $(\alpha^{\text{vox}}, \bar{N})$ :

$$\mathcal{E}^{\text{vox}}(\alpha^{\text{vox}}, \bar{N}) = \sum_{i=1}^{n_v} \left( \frac{\bar{N}_i}{\sigma_i} \right)^2 + \int \left( \frac{q(v; \alpha^{\text{vox}}, \bar{N})}{w(v)} \right)^2 dv \quad (4.27)$$

subject to  $P(\alpha^{\text{vox}}) \neq 0$ .

As described in Equation 4.6, Section 4.6, Equation 4.27 is minimized to estimate volume ratio densities  $\alpha^{\text{vox}}$  and the mean noise vector  $\bar{N}$ .

## Chapter 5

---

# Bayesian Classification Algorithms B and C: Boundary Distance

---

In this chapter we describe two new classification techniques developed within the Bayesian framework of Chapter 3.

The techniques we develop here are similar to that of Chapter 4; as before, the voxel-info consists of histograms taken over voxel regions. The significant differences between the techniques are that we use new histogram basis functions and that the dataset parameters are estimated using a different algorithm.

The new histogram basis functions model voxels near boundaries between two materials. The histogram model has a single parameter: the distance from the center of the voxel to the boundary. The basis functions fit histograms of real datasets better than the partial volume mixtures algorithm, but at the cost of somewhat greater computational expense. The resulting distance parameter is particularly useful in making models of objects because it measures the distance from surface boundaries between materials. These boundaries are generally boundaries between parts of objects

or between objects and their surroundings.

We present the modified assumptions in Section 5.1, the new histogram basis functions in Section 5.2 and the dataset- and voxel parameter estimation in Sections 5.3 and 5.4. Section 5.5 shows results, Section 5.6 discusses them, and Section 5.7 concludes. Detailed derivations are in Section 5.8.

## 5.1 Assumptions

The first three and the fifth assumptions for this technique are identical to those in the previous chapter.

$e_{c1}$ : **Discrete materials.**

$e_{c2}$ : **Normally distributed noise.**

$e_{c3}$ : **Sampling theorem is satisfied.**

$e_{b5}$ : **Uniform tissue measurements.**

As outlined in Section 3.3.4, we replace assumptions  $e_{m4}$  and  $e_{m6}$  as follows.

$e_{b4}$ : **Pair-wise mixtures.** Rather than assuming that each voxel volume can contain some of every material, we assume that each voxel volume consists of either a pure material or of two pure materials separated by a boundary.

$e_{b6}$ : **Gaussian filtering.** The histogram basis function derivation uses the assumption that the sampling filter kernel is approximately Gaussian. This assumption helps us derive a tractable calculation for the new histogram model of boundary-parameterized mixtures and also models the actual collection process better than box filtering.

$e_{b7}$ : **Known materials.** We know the number of materials and can identify samples from each material and mixture within the data.

## 5.2 Histogram Basis Functions

Once again we use two types of histogram basis functions, one for pure materials and one for mixtures of materials. The basis function for pure materials remains a normal distribution. The basis function for a mixture now has an additional parameter that defines the distance from the center of a voxel to a boundary between materials (see Figure 5.1).

From the assumptions and Equation. 4.1 we derive the equation for a pure-material basis function. Because the data collection process band-limits the noise, and because we are looking at histograms over very small regions, the noise is not normally distributed. We divide the noise into two components, one that is constant over a voxel (with mean  $c$  and standard deviation  $\sigma$  over the dataset), and one that is normally distributed around the constant component (with mean 0 and standard deviation  $s$  over a voxel). The equation for a single material, then, is a normal distribution with center  $c + \bar{N}$  and variance  $\sigma^2$ :

$$f_{\text{single}}(v; \bar{N}, c, s) = \prod_{i=1}^{n_v} \frac{1}{s_i \sqrt{2\pi}} \exp\left(-\frac{1}{2} \sum_{i=1}^{n_v} \left(\frac{v - (c + \bar{N})}{s_i}\right)^2\right) \quad (5.1)$$

Dataset parameters for this basis function are  $c$ ,  $s$ , and  $\sigma$ . Because  $\bar{N}$  is constant within a voxel, but varies over the dataset with a normal distribution,  $\sigma$  also becomes a dataset parameter.

From the assumptions and Equation. 4.1 we derive the equation for a mixture basis function. The function uses the same parameters for its pure materials components and adds two additional parameters  $d$  and  $k_w$ , as shown in Figure 5.1. See Figures 5.2 and 5.3 for examples.

$$f_{\text{boundary}}(v; d, \bar{N}, c, s, k_w) = k_n(v; s) * \left( \left( H\left(d + \frac{k_h}{2} - \frac{k_e(v)}{k_w}\right) - H\left(d - \frac{k_h}{2} - \frac{k_e(v)}{k_w}\right) \right) \left| \frac{e^{k_e(v)\sqrt{\pi}}}{(c_2 - c_1)k_w} \right| \right) \quad (5.2)$$

where  $k_e(v) = \text{erf}^{-1}\left(\frac{c_1 + c_2 - 2v}{c_1 - c_2}\right)$  and  $H(x)$  is the Heaviside, or step, function. The derivation follows from Equation. 4.1 evaluated over a region centered at distance  $d$  from a boundary between two materials. The boundary is assumed to be planar and the function low-pass filtered uniformly in all directions so that the sampling theorem is satisfied.  $k_w$  depends on the width of the sampling kernel

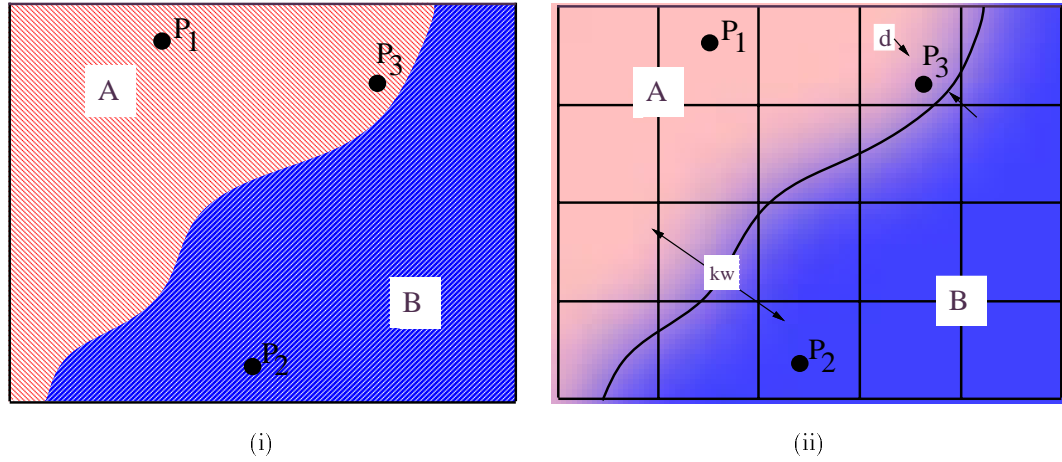


Figure 5.1: We start from the assumption that in a real-world object each point is exactly one material, as in (i). The measurement process creates samples that combine measurements of different materials. From the samples we reconstruct a continuous, band-limited measurement function  $\rho(x)$ . Points  $P_1$  and  $P_2$  lie inside regions of a single material. Point  $P_3$  lies near a boundary between materials in (i), and so in (ii)  $P_3$  is shown with a parameter  $d$  that indicates how far the center of the surrounding voxel is from the boundary. The parameter  $k_w$  shows the width of the region where the pure material measurements mix together and is dependent on the width of the sampling kernel. The grid lines show voxel boundaries and how they relate to the regions.  $\square$

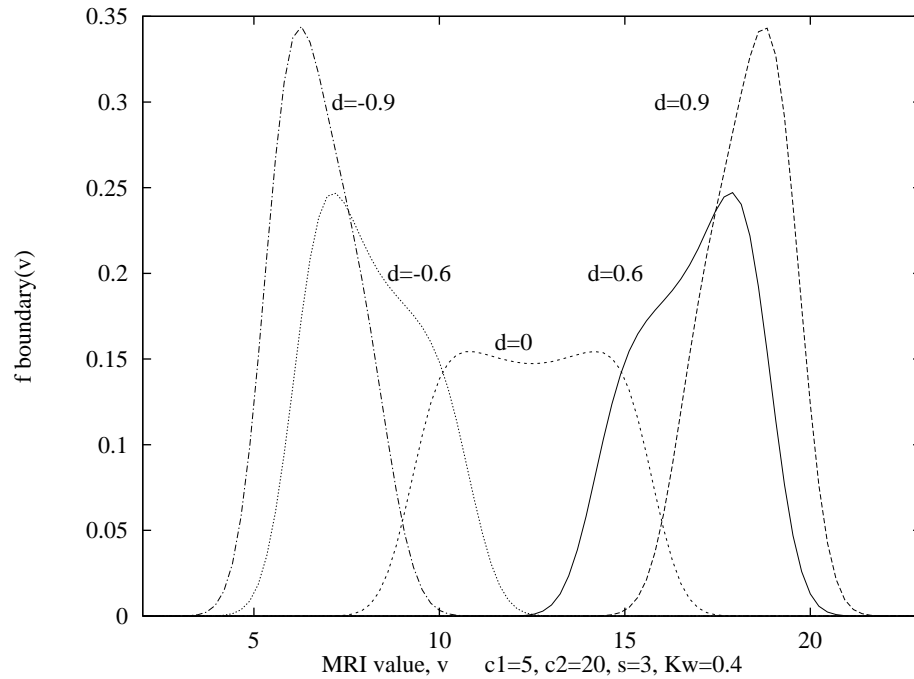


Figure 5.2: The shapes of histogram basis functions,  $f_{\text{boundary}}(v)$ , for different values of  $d$ , the distance from the boundary to a voxel center. Note that the shapes approach normal distributions as  $d$  moves away from 0. The histograms shown are for scalar data and are 1-dimensional. Figure 5.3 shows histogram basis functions for vector-valued data.  $\square$

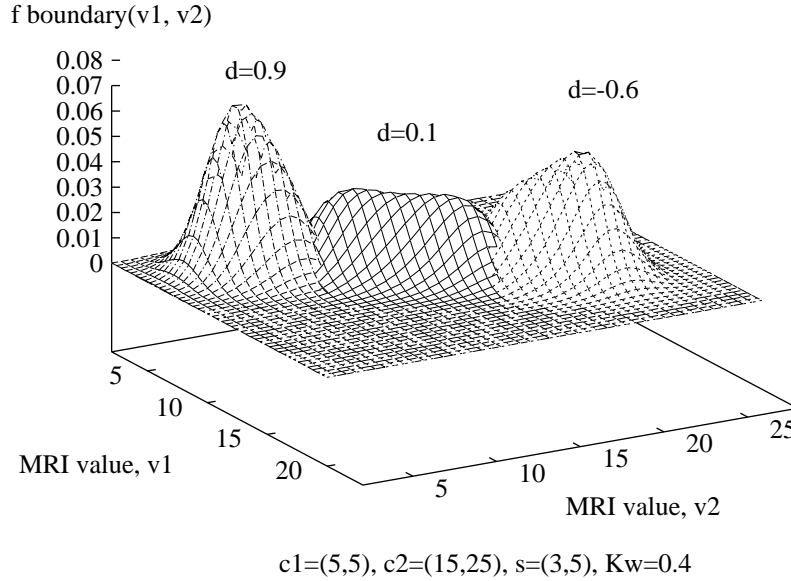


Figure 5.3: The shapes of  $f_{\text{boundary}}(v)$  histogram basis functions for vector-valued data. Three different values of  $d$ , the distance from the boundary to a voxel center, are represented. Figure 5.2 shows examples for scalar data.  $\square$

used to create the samples. Section 5.8 presents a more detailed derivation.

The parameter  $d$  is estimated individually for each voxel we classify as described in Section 5.4.  $k_w$  is estimated once for an entire dataset as described in Section 5.3.

### 5.3 Estimating Dataset Parameters

In this section we describe the process of estimating the material parameters that are constant throughout a dataset. For each pure material the dataset parameters include the expected center value of the voxel,  $c$ ; the expected deviation of  $c$  from voxel to voxel,  $s$ , the expected deviation from  $c$  of values within a voxel,  $\sigma$  and  $w(v)$ . For material mixtures the dataset parameters also include  $k_w$ , the sampling kernel width.  $w(v)$  is an analog of the standard deviation of a histogram from the expected value of the histogram. We discuss this further below.

We estimate these parameters from several interactively selected sets of voxels. Each set consists of voxels containing a single pure material or of voxels near a boundary between two known pure

materials.

For each voxel in a set representing one pure material, we calculate a mean and deviation of the values within the voxel. The mean value of all of the voxel means is  $c$ . The deviation of all the voxel mean values is  $s$ . The mean of all the voxel deviations is  $\sigma$ .

For each voxel in a set representing a mixture, we fit  $f_{\text{boundary}}()$  to the histogram over the voxel allowing  $d$  and  $k_w$  to vary. This gives us a value for  $k_w$ . We use the mean value of these voxel  $k_w$  values for classifying voxels over the entire dataset.

### 5.3.1 Non-uniform Material Signatures

Our third classification algorithm differs from the second only in the estimation of dataset parameters. For the third algorithm, the material parameter  $c$ , which measures the expected value of a material within a dataset, is defined as a function  $c(x)$  over the imaging volume. We model  $c(x)$  with a simple parameterized function of space according to our knowledge of the sources of intensity changes across an MRI dataset, and then fit that function to the interactively chosen points as described above.  $s$  and  $\sigma$  are calculated as for the second algorithm, but using  $c(x)$ .

When estimating the voxel parameters as described in the next section, we can evaluate  $c(x)$  for a given voxel and use that value in finding the voxel parameters.

## 5.4 Estimating Voxel Parameters

With estimates for dataset parameters we can estimate the voxel parameters for each voxel in a dataset. One voxel parameter,  $\alpha_b$ , is discrete and determines which material or pair of materials a voxel contains. We break the classification process up into one optimization over a continuous domain for each material or pair. We then choose the one that fits best.

The optimization process for a particular pure material minimizes the equation

$$\mathcal{E}_{\text{pure}}(\bar{N}) = \sum_{i=1}^{n_v} \left( \frac{\bar{N}_i}{\sigma_i} \right)^2 + \sum_{i=1}^{n_b} \left( \frac{h(v_i - \bar{N}_i) - f_{\text{pure}}(v_i)}{w(v_i)} \right)^2 \quad (5.3)$$

where  $n_b$  is the number of points in feature space over which we evaluate the difference between the histogram and its model. The remainder of the equation is a series of squares of ratios between differences and their expected values. The expected value of each term is 1, and so the expected value for  $\mathcal{E}$  is  $n_v + n_b$ , which gives us a measure of how well a basis function fits a voxel histogram.

We choose a set of feature space points on a regular grid with spacing smaller than the smallest  $\sigma$ . Any points on the grid with positive histogram values are used in the summation.

The optimization process for a particular mixture minimizes the equation

$$\mathcal{E}_{\text{boundary}}(\bar{N}, d) = \sum_{i=1}^{n_v} \left( \frac{\bar{N}_i}{\sigma_i} \right)^2 + \sum_{i=1}^{n_b} \left( \frac{h(v_i - \bar{N}_i) - f_{\text{boundary}}(v_i)}{w(v_i)} \right)^2 \quad (5.4)$$

The derivations of Equations 5.3 and 5.4 are described in more detail in Section 5.8.

Values from Equations 5.3 and 5.4 cannot be compared directly, as is shown in Section 5.8. Instead, we convert them to probabilities with the following equations and compare the results at the optimized points to choose the most likely material or combination.

$$\hat{P}_{\text{pure}}(\bar{N}) = \frac{1}{(2\pi)^{\frac{n_v+n_b}{2}} \prod_{i=1}^{n_v} \sigma_i \prod_{i=1}^{n_b} w(v_i)} e^{-\frac{1}{2} \mathcal{E}_{\text{pure}}(\bar{N})} \quad (5.5)$$

$$\hat{P}_{\text{boundary}}(\bar{N}, d) = \frac{1}{(2\pi)^{\frac{n_v+n_b}{2}} \prod_{i=1}^{n_v} \sigma_i \prod_{i=1}^{n_b} w(v_i)} e^{-\frac{1}{2} \mathcal{E}_{\text{boundary}}(\bar{N}, d)} \quad (5.6)$$

## 5.5 Results

We have classified simulated MRI data with the boundary distance algorithm and compare them with results from several other algorithms in Figure 5.4. The simulated data that we classified is shown in Figure 5.4(ii) with Figure 5.4(iii) illustrating what an ideal classification algorithm would produce. Discrete classification, using vector data, but only a single measurement point per voxel and assuming only pure materials, produces the results in Figure 5.4(iv). Note the jaggy edges and the band of misclassified data for material 3 along the boundary between materials 1 and 2.



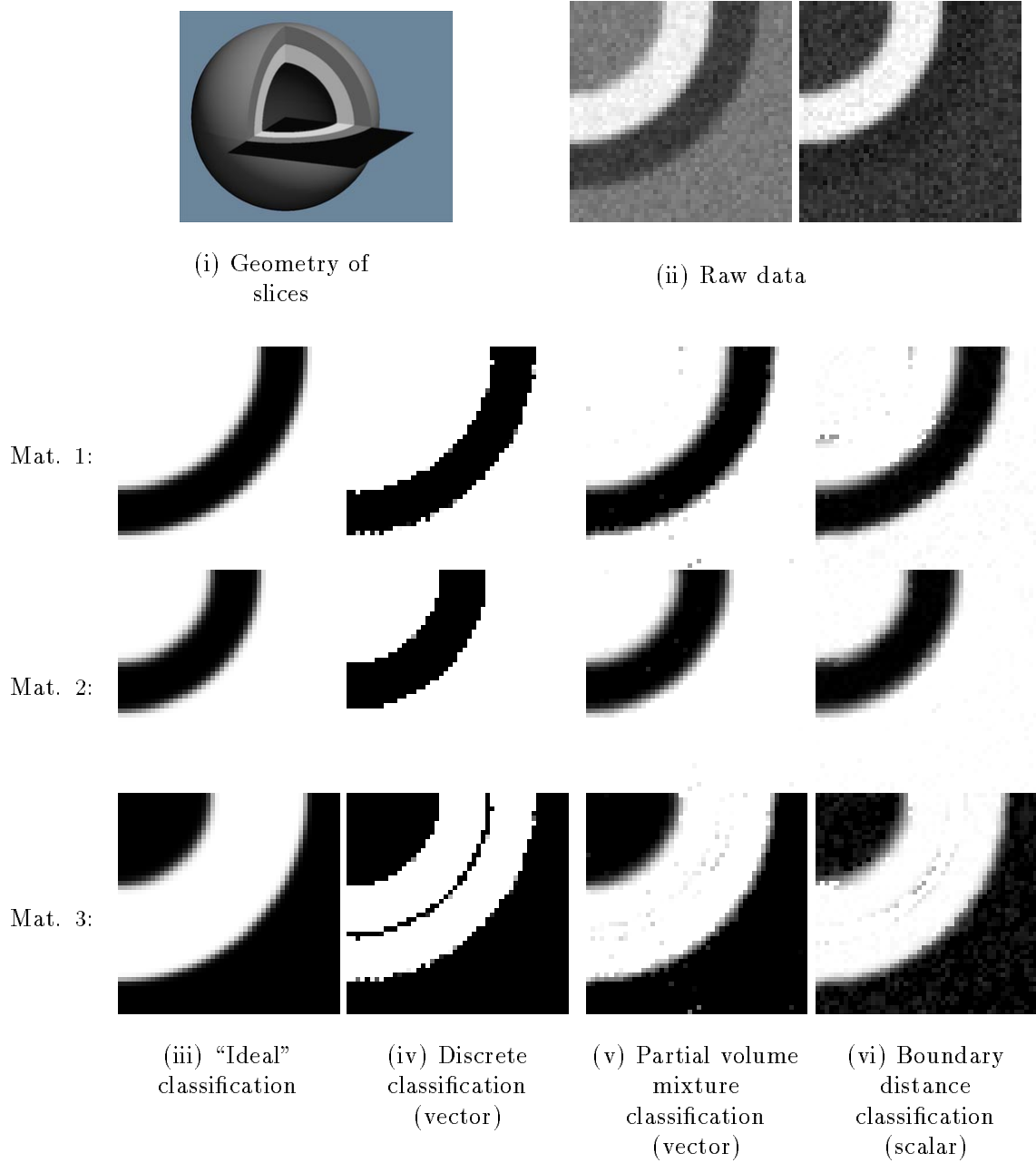


Figure 5.4: The boundary distance algorithm is compared to other algorithms in classifying simulated MRI data. (ii) shows the simulated data, which contains three different materials. The geometry that the data measures is shown in (i). (iii) shows what an "ideal" classification algorithm should produce and (iv)-(vi) show results from different algorithms. Note that the new algorithms (v) and (vi) produce results most similar to the ideal case, and that (vi) does so even with scalar data.  $\square$

Figure 5.4(v) and Figure 5.4(vi) show the partial volume mixtures algorithm from Chapter 4 and the boundary distance algorithm from this chapter. Note that even with scalar data, the boundary distance algorithm achieves results very close to the ideal case.

## 5.6 Discussion

**Ambiguous classification.** For a voxel that is well within a region of pure material  $A$ , the algorithm sometimes correctly classifies the voxel as pure material  $A$ , and sometimes classifies it as a mixture of  $A$  and a very small amount of some other material. Both solutions are physically reasonable because the mixture basis functions approach a normal distribution as the boundary distance parameter  $d$  moves away from zero.

Similarly, two different mixtures, each containing material  $A$ , can match a voxel that is within a region of pure material  $A$ . Again, the choice is not critical.

**Sensitivity to interactively selected material classes.** The results of the algorithm are highly dependent on the material points selected interactively to represent each pure material and each pair of materials. These points must be selected carefully, and should come from a set of points that actually represent a single consistent material. Representing points from two materials as one material can create a situation where the distributions of the sample values do not match a normal distribution, and the classification results are less accurate.

The algorithm could verify that the selected points are normally distributed to identify the problem and report it to the user.

**Sensitivity to contrast between materials.** The classification is sensitive to the contrast-to-noise ratio between different materials. If this ratio is too small, materials cannot be distinguished. This requirement is fed back to the data-collection process described in Chapter 2.

**Computational expense.** The implementations described in this chapter are computationally expensive. The optimization process must be run on each voxel in a dataset. At ten voxels per second, a medium-sized dataset of  $256 \times 256 \times 64$  voxels runs in about 5 days. Through approximations it may be possible to reduce this time significantly.

The algorithm processes each voxel independently, and so is highly amenable to a domain-decomposition parallel solution. In fact, we have run it on a network of ten HP 9000/700 and DEC Alpha workstations and gotten a speedup of almost ten in classifying medium to large datasets.

**More sophisticated geometric basis functions.** The basis functions that we have developed model the two most common geometric cases: samples within regions of pure material and samples near surface boundaries. Additional basis functions, however, could model other geometries and create more accurate models. Examples include samples near edges where three materials come together, or points near membranes that are thinner than the sample spacing, where, again, three materials would have an effect on the measurement.

**Incorporating additional global information.** Except for the interpolation of samples, we currently classify each voxel without regard to its neighbors and without directly using the interactively selected representative points for each material. Both types of information could be incorporated into the prior probability estimates to influence the classification process.

## 5.7 Conclusion

We have presented two new classification algorithms, one a variation on the other, built within the Bayesian framework we described in Chapter 3. The algorithms are based on a more accurate model of the MRI process than the algorithm of Chapter 4, and so produce better results, but are computationally more expensive.

---

## 5.8 Detailed Derivations

This section derives the boundary distance histogram basis functions for pure materials and for mixtures as well as the prior probability optimization equations used in Section 5.4.

### 5.8.1 Pure Histogram Basis Function

The derivation for pure material basis functions is identical to that of Ch. 4 and is in Section 4.10.1.

### 5.8.2 Mixture Histogram Basis Function

For a sample taken near a boundary between two pure materials we start with an object that spans all of 3-space and that has two materials separated by a planar boundary. Because we are going to use a rotationally symmetric Gaussian sampling kernel, we can perform a change of coordinates on our object to make the planar boundary pass through the origin and be perpendicular to the  $x_0$ -axis.

The object function is:

$$v(x) = \begin{cases} c_1 & \text{if } x_0 < 0 \\ c_2 & \text{if } x_0 > 0 \end{cases} \quad (5.7)$$

Our measurement function is:

$$\rho_{\text{boundary}}(x) = \int \int \int k(\hat{x}_0)k(\hat{x}_1)k(\hat{x}_2)v(x - \hat{x})d\hat{x}_2d\hat{x}_1d\hat{x}_0 + n(x; s) \quad (5.8)$$

where  $k(x)$  is the 1-D Gaussian sampling kernel. Its width is determined by an implicit parameter  $k_w$ .  $v(x - \hat{x})$  is independent of  $x_1$  and  $x_2$ , so

$$\rho_{\text{boundary}}(x) = \int k(\hat{x}_0)v(x - \hat{x}) \left( \int \int k(\hat{x}_1)k(\hat{x}_2)d\hat{x}_2d\hat{x}_1 \right) d\hat{x}_0 + n(x; s) \quad (5.9)$$

The term in parentheses is one, and so:

$$\rho_{\text{boundary}}(x) = \int_{-\infty}^{\infty} k(\hat{x}_0)v(x_0 - \hat{x}_0)d\hat{x}_0 + n(x; s) \quad (5.10)$$

We assume a Gaussian kernel function:

$$k(x) = \frac{1}{k_w\sqrt{\pi}}e^{-\left(\frac{x}{k_w}\right)^2} \quad (5.11)$$

By evaluating the integrals we find:

$$\begin{aligned} \rho_{\text{boundary}}(x) &= \int_{-\infty}^{\infty} k(\hat{x}_0)v(x_0 - \hat{x}_0)d\hat{x}_0 + n(x; s) \\ &= c_1 \int_{-\infty}^{x_0} k(\hat{x}_0)d\hat{x}_0 + c_2 \int_{x_0}^{\infty} k(\hat{x}_0)d\hat{x}_0 + n(x; s) \\ &= \frac{1}{2}(c_2 + c_1 + (c_2 - c_1)\text{erf}(k_w x_0)) + n(x; s) \end{aligned} \quad (5.12)$$

This measurement function can now be substituted into Equation. 4.1 to derive the boundary basis function:

$$\begin{aligned} f_{\text{boundary}}(v; d, \bar{N}, c, s, k_w) &= \int \mathcal{R}(x)\delta(f_{\text{boundary}}(x) - v)dx \\ &= \int \mathcal{R}(x)\delta\left(\frac{1}{2}(c_2 + c_1 + (c_2 - c_1)\text{erf}(k_w x_0)) + n(x; s) - v\right)dx \\ &= k_n(v; s) * \int \mathcal{R}(x)\delta\left(\frac{1}{2}(c_2 + c_1 + (c_2 - c_1)\text{erf}(k_w x_0)) - v\right)dx \end{aligned} \quad (5.13)$$

We define the region  $\mathcal{R}(x)$  as a rectangular solid  $k_h$  on a side and distance  $d$  from the boundary at 0. Because the integrand depends only on  $x_0$ , we can reduce this to a single integral

$$= k_n(v; s) * k_h^2 \int_{d-\frac{k_h}{2}}^{d+\frac{k_h}{2}} \delta\left(\frac{1}{2}(c_2 + c_1 + (c_2 - c_1)\text{erf}(k_w x_0)) - v\right)dx_0 \quad (5.14)$$

$$= k_n(v; s) * \left( \left( H\left(d + \frac{k_h}{2} - \frac{k_e(v)}{k_w}\right) - H\left(d - \frac{k_h}{2} - \frac{k_e(v)}{k_w}\right) \right) \left| \frac{e^{k_e(v)}\sqrt{\pi}}{(c_2 - c_1)k_w} \right| \right) \quad (5.15)$$

where  $k_e(v) = \text{erf}^{-1}\left(\frac{c_1+c_2-2v}{c_1-c_2}\right)$  and  $H(x)$  is the Heaviside, or step, function.

$$H(x) = \begin{cases} 0 & \text{if } x < 0 \\ 1 & \text{if } x > 0 \end{cases} \quad (5.16)$$

We refer to the right operand of the convolution as  $r(v)$

$$r(v) = \left( \left( H\left(d + \frac{k_h}{2} - \frac{k_e(v)}{k_w}\right) - H\left(d - \frac{k_h}{2} - \frac{k_e(v)}{k_w}\right) \right) \left| \frac{e^{k_e(v)\sqrt{\pi}}}{(c_2 - c_1)k_w} \right| \right) \quad (5.17)$$

$$f_{\text{boundary}}(v) = k_n(v) * r(v) \quad (5.18)$$

### Implementation Considerations

Our implementation evaluates this function by creating a piecewise-linear approximation to  $r(v)$  and summing the convolutions of the linear pieces.  $r(v)$  is non-zero only between

$$\frac{1}{2}(c_2 + c_1 + (c_2 - c_1)\text{erf}(k_w(d + \frac{k_h}{2}))) \quad (5.19)$$

and

$$\frac{1}{2}(c_2 + c_1 + (c_2 - c_1)\text{erf}(k_w(d - \frac{k_h}{2}))) \quad (5.20)$$

We evaluate  $r(v)$  at regularly spaced points between those endpoints, scale the resulting values to preserve the total integral, evaluate the convolution, and sum the results.

### 5.8.3 Pure Material Parameter Estimation

We wish to be able to evaluate

$$P(\bar{N}|h) = \frac{P(\bar{N})P(h|\bar{N})}{P(h)} \quad (5.21)$$

where  $h$  is the histogram over a voxel and  $\bar{N}$  is the voxel parameter for a pure material.

**Prior probability** is defined as

$$P(\bar{N}) = \frac{1}{(2\pi)^{\frac{n_v}{2}} \prod_{i=1}^{n_v} \sigma_i} e^{-\frac{1}{2} \sum_{i=1}^{n_v} \left(\frac{\bar{N}_i}{\sigma_i}\right)^2} \quad (5.22)$$

**Likelihood** is defined by analogy to a multi-dimensional normal distribution. We choose  $n_b$  points in feature space and calculate the difference between the histogram model and the histogram at those points.

$$P(h|\bar{N}) = \frac{1}{(2\pi)^{\frac{n_b}{2}} \prod_{i=1}^{n_b} w(v_i)} e^{-\frac{1}{2} \sum_{i=1}^{n_b} \left(\frac{h(v_i - \bar{N}_i) - f_{\text{pure}}(v_i)}{w(v_i)}\right)^2} \quad (5.23)$$

**Global likelihood** is a constant as in Section 4.11.3.

**Assembly of prior probability.**

$$P(\bar{N}|h) = \frac{1}{P(h)} \frac{1}{(2\pi)^{\frac{n_v+n_b}{2}} \prod_{i=1}^{n_v} \sigma_i \prod_{i=1}^{n_b} w(v_i)} e^{-\frac{1}{2} \left( \sum_{i=1}^{n_v} \left(\frac{\bar{N}_i}{\sigma_i}\right)^2 + \sum_{i=1}^{n_b} \left(\frac{h(v_i - \bar{N}_i) - f_{\text{pure}}(v_i)}{w(v_i)}\right)^2 \right)} \quad (5.24)$$

Because the coefficient of the exponential is constant with respect to the arguments of  $P(\bar{N}|h)$ , maximizing  $P(\bar{N}|h)$  is equivalent to minimizing:

$$\mathcal{E}_{\text{pure}}(\bar{N}) = \sum_{i=1}^{n_v} \left(\frac{\bar{N}_i}{\sigma_i}\right)^2 + \sum_{i=1}^{n_b} \left(\frac{h(v_i - \bar{N}_i) - f_{\text{pure}}(v_i)}{w(v_i)}\right)^2 \quad (5.25)$$

In comparing the optimization result among different materials, we convert to probabilities, neglecting the global likelihood, which is not a function of the material.

$$\hat{P}_{\text{pure}}(\bar{N}) = \frac{1}{(2\pi)^{\frac{n_v+n_b}{2}} \prod_{i=1}^{n_v} \sigma_i \prod_{i=1}^{n_b} w(v_i)} e^{-\frac{1}{2} \mathcal{E}_{\text{pure}}(\bar{N})} \quad (5.26)$$

#### 5.8.4 Material Mixture Parameter Estimation

We wish to be able to evaluate

$$P(\bar{N}, d|h) = \frac{P(\bar{N}, d)P(h|\bar{N}, d)}{P(h)} \quad (5.27)$$

where  $\bar{N}$  and  $d$  are voxel parameters and  $h$  is the histogram over a voxel.

The derivation follows that of the previous section.

**Prior probability** is defined as

$$P(\bar{N}, d) = P(\bar{N})P(d) \quad (5.28)$$

$P(\bar{N})$  is identical to Equation 5.22.

Effects from a boundary do not occur at significant distances from the boundary. We define significant distance as 3 times the width of the spatial sampling kernel and create a probability density function for  $P(d)$  that integrates to one:

$$P(d) = \begin{cases} \frac{1}{6} & \text{if } -3 < d < 3 \\ 0 & \text{otherwise} \end{cases} \quad (5.29)$$

**Likelihood** is defined in the same manner as Equation 5.23.

$$P(h|\bar{N}, d) = \frac{1}{(2\pi)^{\frac{n_b}{2}} \prod_{i=1}^{n_b} w(v_i)} e^{-\frac{1}{2} \sum_{i=1}^{n_b} \left( \frac{h(v_i - \bar{N}_i) - f_{\text{boundary}}(v_i)}{w(v_i)} \right)^2} \quad (5.30)$$

**Global likelihood** is a constant as in Chapter 4.

**Assembly of prior probability.**

$$P(\bar{N}, d|h) = \frac{1}{P(h)} \frac{1}{(2\pi)^{\frac{n_v+n_b}{2}} \prod_{i=1}^{n_v} \sigma_i \prod_{i=1}^{n_b} w(v_i)} e^{-\frac{1}{2} \sum_{i=1}^{n_v} \left( \frac{\bar{N}_i}{\sigma_i} \right)^2 + \sum_{i=1}^{n_b} \left( \frac{h(v_i - \bar{N}_i) - f_{\text{boundary}}(v_i)}{w(v_i)} \right)^2} \quad (5.31)$$

Because the coefficient of the exponential is constant with respect to the arguments of  $P(\bar{N}, d|h)$ , maximizing  $P(\bar{N}, d|h)$  is equivalent to minimizing:



$$\mathcal{E}_{\text{boundary}}(\bar{N}, d) = \sum_{i=1}^{n_v} \left( \frac{\bar{N}_i}{\sigma_i} \right)^2 + \sum_{i=1}^{n_b} \left( \frac{h(v_i - \bar{N}_i) - f_{\text{boundary}}(v_i)}{w(v_i)} \right)^2 \quad (5.32)$$

In comparing the optimization result among different materials, we convert to probabilities, neglecting the global likelihood, which is not a function of the material mixture.

$$\hat{P}_{\text{boundary}}(\bar{N}, d) = \frac{1}{(2\pi)^{\frac{n_v+n_b}{2}} \prod_{i=1}^{n_v} \sigma_i \prod_{i=1}^{n_b} w(v_i)} e^{-\frac{1}{2} \mathcal{E}_{\text{boundary}}(v, d)} \quad (5.33)$$

## **PART III**

# **Applications**

The following two chapters describe computer graphics applications that use the data collection and classification techniques of the earlier chapters. Chapter 6 describes a taxonomy of computer graphics models and Chapter 7 describes a new algorithm for directly volume-rendering deformed volume data.

## Chapter 6

---

# Model Building

---

A major unsolved problem in computer graphics is that of making high-quality models. Traditionally, models have consisted of interactively or algorithmically described collections of graphics primitives such as polygons or patches. The process of constructing these models is painstaking and often misses features and behavior that we wish to model.

In this chapter we present a taxonomy of computer graphics models that can be created from classified sampled MRI data. We use results from the earlier chapters to create examples of both static and dynamic models of objects from MRI measurements. These new results illustrate the utility of the data-collection and classification processes.

Many of the goals used in developing the data-collection and tissue-classification algorithms derive from requirements of the model-extraction process, providing feedback to those earlier stages of the pipeline.

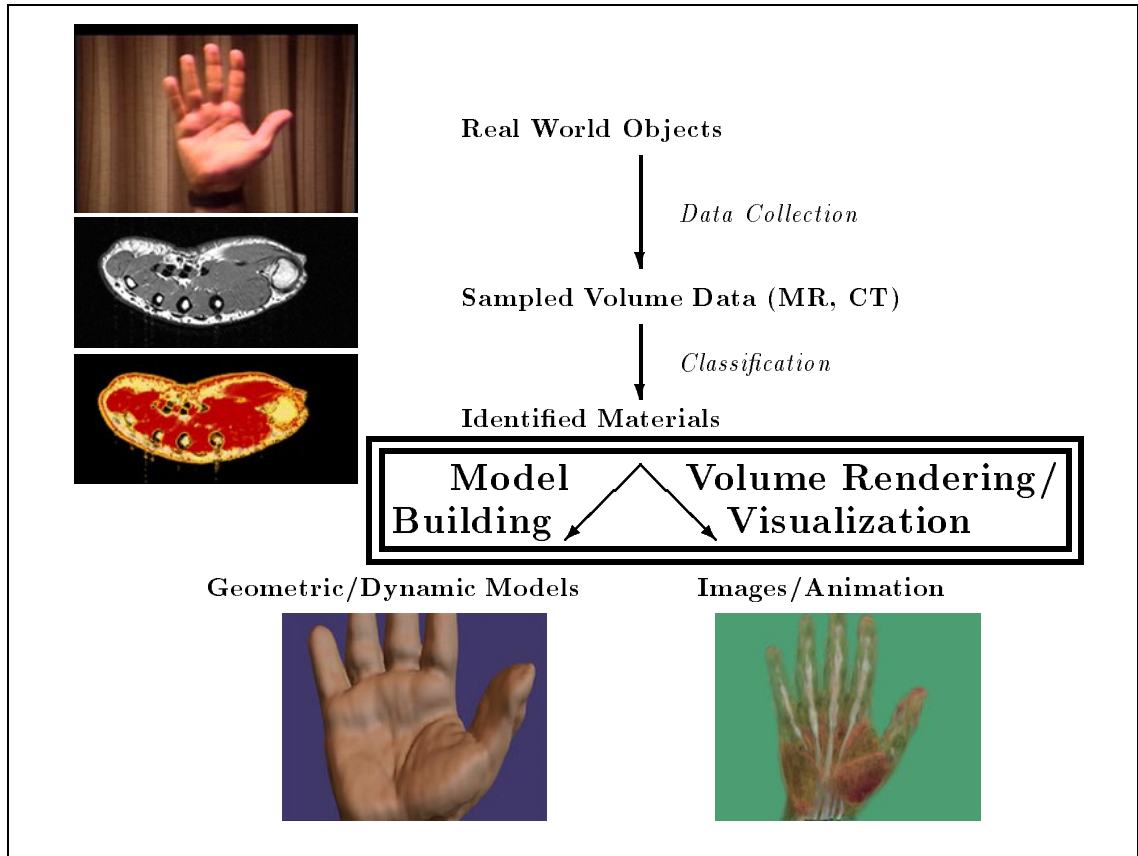


Figure 6.1: Model-building and visualization context. The model-building and visualization stages are the final stage in the pipeline for extracting computer graphics models from MRI data. □

## 6.1 Taxonomy of Computer Graphics Models

Our modeling taxonomy splits models into those with regions of constant material and those with materials that vary continuously. Constant-material models, from which our examples are taken, can be divided into static and dynamic.

Within each category we define both surface models and volume models. Surface models capture the shape of an object showing the boundaries where pairs of materials meet. Volume models incorporate information about the internal structure of each region. The volumes are solid regions of space that exhibit a common appearance and behavior.

Dynamic models capture not only the shape, but characteristics of the behavior of an object—how it moves and changes shape in the course of performing some task. For many objects, different

	Uniform-Material Models	
	Static	Dynamic
Surface	lobster (Figure 6.2) tooth (Figure 6.4) “bear” (Figure 6.6)	
Volume	bee (Figure 6.7)	jade plant (Figure 6.9) banana (Figure 6.10)

Table 6.1: Examples from within our taxonomy of computer graphics models of objects with regions of relatively uniform materials. □

materials within an object have a strong influence on their behavior. For example, a human hand modeled as only skin behaves differently than one modeled with bone, muscle, fat, and skin. MRI volume data provides us with internal measurements. Our dynamic models are all volume models, but surface models, representing cloth, for example, have also been developed [Weil, 1986].

Table 6.1 shows the part of the taxonomy from which we draw our examples and gives references to figures illustrating the different categories.

## 6.2 Modeling Examples

Our surface-based models are calculated as isosurfaces of continuous functions. Isosurfaces of a function over space are analogs to isocontours of a function over a plane. The functions from which we extract our surfaces are reconstructed from the sampled data produced by our classification algorithms, and so must satisfy the Nyquist sampling theorem.

By operating on classified data we can extract surface models where the surfaces define the boundaries between materials. Because the histogram basis functions from our classification techniques model the boundaries between materials, the parameters of the basis functions provides us with a physical basis for where the surfaces lie.

Classified data serves as a volume model. The relevant spatial information is encoded in that data, and can be extracted with rendering and simulation algorithms. Volume rendering is particularly useful because it integrates over an entire volume and tends to reduce image artifacts

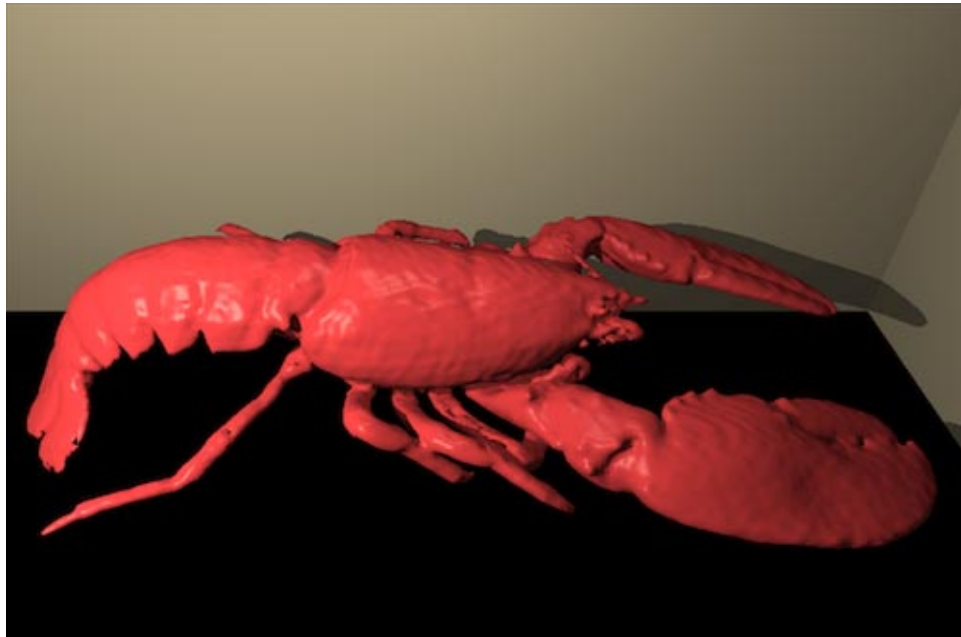


Figure 6.2: A rigid model of the external surface of a lobster. MRI data of a lobster was collected, each voxel classified using the partial volume mixtures algorithm, and then a polygonal isosurface of the surrounding material calculated. The underside of the lobster is shown in Figure 6.3. □

caused by noise in collected data.

We show a collection of models, beginning with static surface models and progressing through static volume models to dynamic volume models.

### 6.2.1 Static Surface Models

Surface models capture the shape of an object. Using data classified with the partial-volume mixtures algorithm (Chapter 4), we approximate the boundary for each material as the point where the local density function is 0.5. For data classified with the boundary distance algorithms (Chapter 5) we similarly approximate the boundary as the locus of points where the boundary-distance function is 0. The isosurface at these levels is the best approximation to the correct surface given the sampled data.

In either case, we use an algorithm such as marching-cubes [Lorensen and Cline, 1987], available in the visualization software product AVS [Upson et al., 1989], to produce a polygon mesh approximation to the boundary given sampled data. We also use standard polygon rendering algorithms to generate

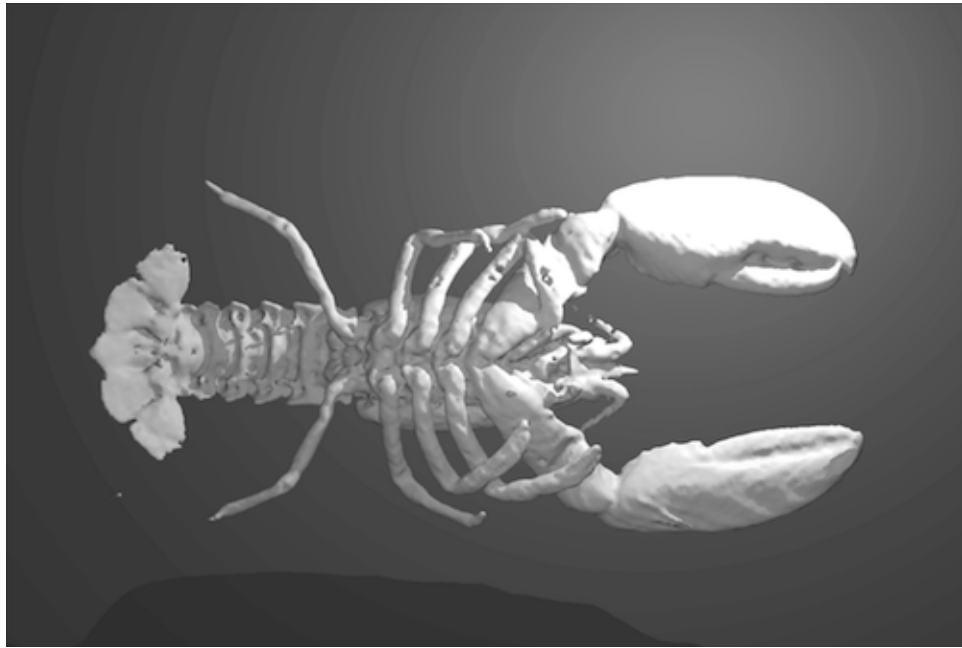


Figure 6.3: Underside of the rigid model shown in Figure 6.2. □

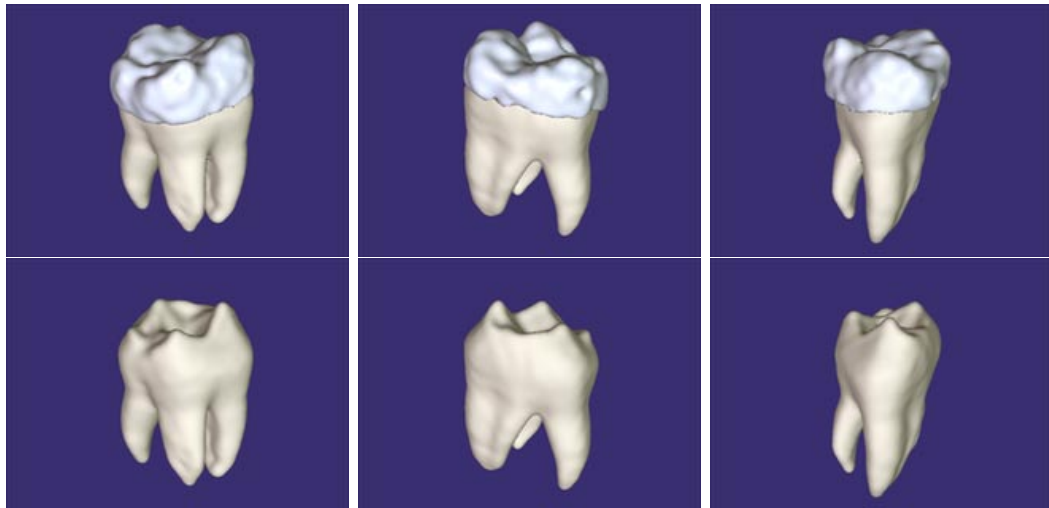


Figure 6.4: A geometric model of tooth dentine and enamel created by collecting MRI data using a technique that images hard solid materials, classifying dentine and enamel in the volume data with our new partial volume mixtures algorithm. Polygonal isosurfaces define the bounding surfaces of the dentine and enamel. □

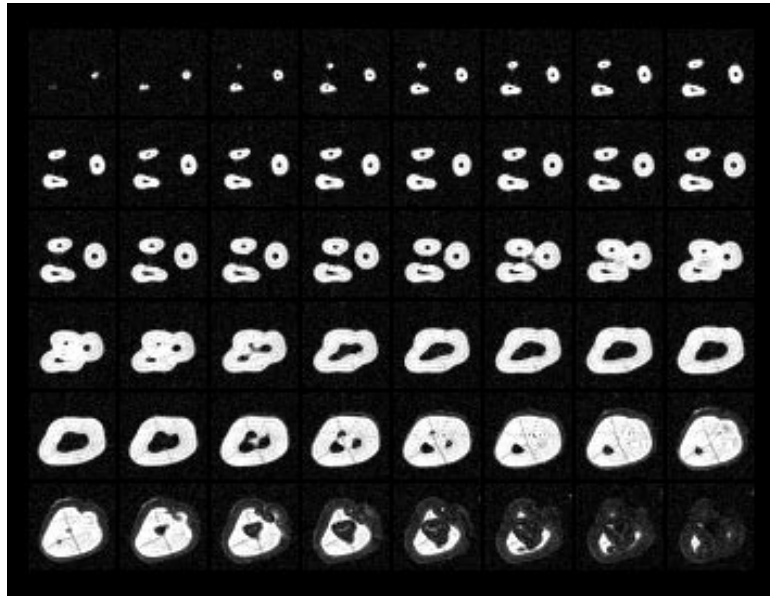


Figure 6.5: MRI data of a human molar collected using a new technique that images solid materials. □

images from polygon meshes.

Figures 6.2 and 6.3 show the top and underside of a lobster model extracted from classified MRI data. Three interleaved, multi-slice, two-echo acquisitions were combined to produce data satisfying the Nyquist sampling theorem. The data were classified with our partial volume mixtures algorithm, and an isosurface defining where the surrounding material ended was used to represent the surface of the animal. Note the detail in the model, particularly on the underside.

Figure 6.4 shows images of a surface model of a human molar tooth. The surface model was created from MRI data (Figure 6.5) collected using an MRI technique that is capable of imaging hard solids [Ghosh et al., 1995] [Gravina and Cory, 1994]. Our partial volume mixtures classification algorithm identifies three materials, enamel, dentine, and the surrounding air, despite the similar values for enamel and air in the sampled data. We calculated polygonal isosurfaces for the dentine and enamel and rendered both together, to show the entire tooth, and the dentine alone, to show the dentine/enamel boundary.

Figure 6.6 shows a surface model created from a plastic bear. The plastic bear was prepared for data acquisition by embedding it in agar to provide MRI contrast between it and its surroundings.





Figure 6.6: Polygonal model extracted from MRI data of a plastic bear. The plastic does not provide signal with conventional MRI acquisition techniques, so the bear was set in agar to provide contrast between it and its surroundings. A polygonal isosurface extraction captured the surface geometry directly from the data because only agar and plastic needed to be identified. The texture on the geometric model was specified using a new technique that spreads small patches across the surface maintaining orientation between neighbors to attain a combed appearance [Fleischer et al., 1995]. □

Three multi-slice datasets consisting of 3mm slices were collected, each offset by 1mm from the others, and the results interleaved to produce data satisfying the Nyquist sampling theorem. Only two materials are present in the dataset, so a polygonal isosurface was extracted directly from the data. A new algorithm to specify surface texture [Fleischer et al., 1995] spread patches of “fur” across the surface and maintained a consistent local orientation of the patches to produce a combed appearance.

### 6.2.2 Static Volume Models

Classified volume data serves as a model of the underlying objects, and can be rendered with volume-rendering algorithms [Drebin et al., 1988] [Levoy, 1988] [Upson and Keeler, 1988].

Figure 6.7 shows volume-rendered images of a model of a bee. The model consists of MRI data classified with the our partial volume mixtures algorithm. The image on the left shows primarily the surface by using opaque materials. The image on the right shows the materials in different, transparent colors.

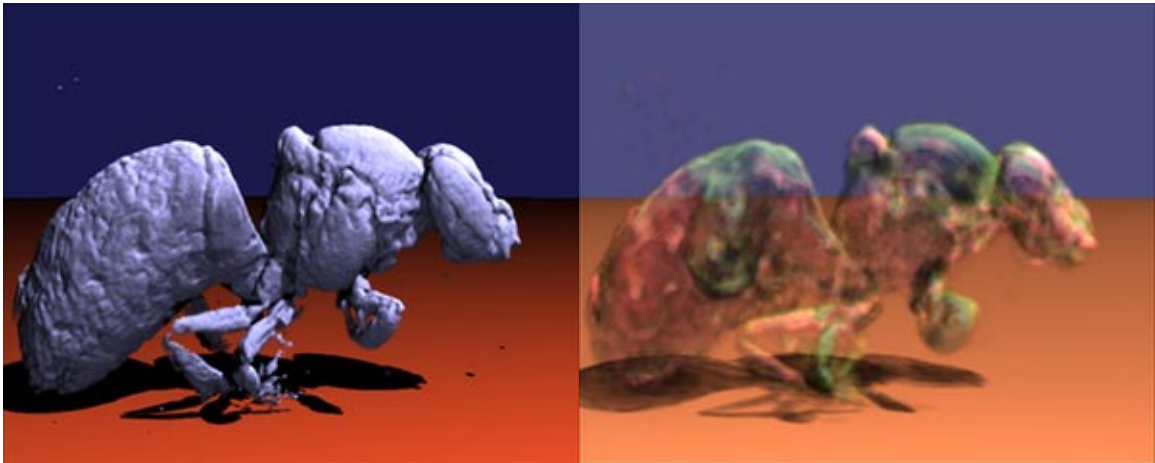


Figure 6.7: Classified MRI data of a bee rendered with opaque materials on the left and semi-transparent materials on the right. The volume data was classified with the partial volume mixtures algorithm. □

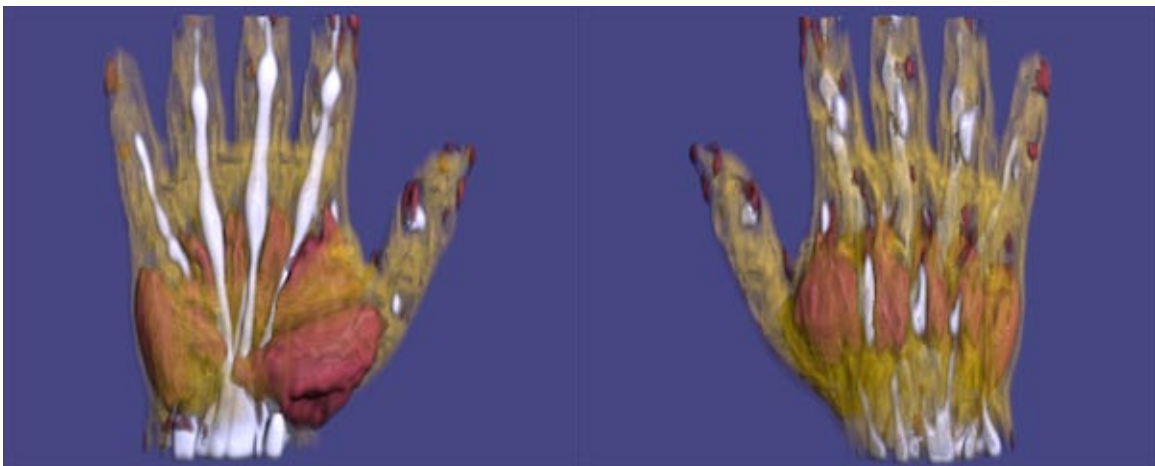


Figure 6.8: Volume-rendered images of human hand model from the front and back, with muscle in red, fat in yellow, and tendon in white. Multi-slice data was classified with the partial volume mixtures algorithm. □

Figure 6.8 shows volume-rendered images of a classified human hand dataset. Tendon is shown in opaque white, muscle in semi-opaque red, and fat in transparent yellow. To better show the internal structure, the skin has not been rendered.

### 6.2.3 Dynamic Models

We represent dynamic models in two different ways: physically-based deformations and kinematically-specified deformations. Much related work has been devoted to representing flexible bodies for computer graphics, e.g., [Platt and Barr, 1988],[Baraff and Witkin, 1992]. We have chosen



Figure 6.9: Results of collecting MRI data of a jade plant, classifying each voxel in the volume data with the partial volume mixtures algorithm, creating a flexible model, and simulating a twisting deformation of the model over time. □

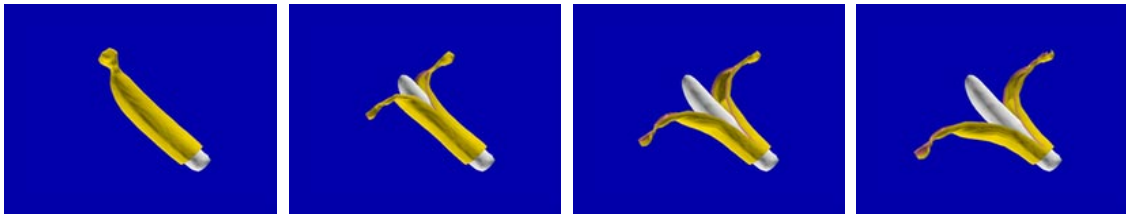


Figure 6.10: Results of collecting MRI data of a banana, identifying peel and flesh in the data, creating solid parts for each material information, and flexibly deforming the outer material to peel it. We used the partial volume mixtures classification algorithm. □

a simple mass points and springs representation, but more complex and accurate finite element method representations would also be possible.

Our physically-based deformations consist of a collection of mass points and springs connected in a regular, 3-D, rectangular grid surrounding the object. The strengths of the springs and mass values at the points are chosen based on the materials within each grid rectangle. By exerting forces on selected mass points, we cause deformations that simulate the behavior of the modeled materials. The deformations are specified via control points [Sederberg and Parry, 1986] that take on the positions of the simulated mass points.

Figures 6.9 and 6.10 show examples created with this technique. In Figure 6.9 we show three frames from an animation in which an initial twisting force was specified for all of the points. Frames were generated as the model returned to equilibrium. In Figure 6.10 forces were applied to points of the banana peel near its apex to pull the peel away from the flesh. The banana was measured with MRI and the data classified to distinguish peel from flesh. Four frames from the

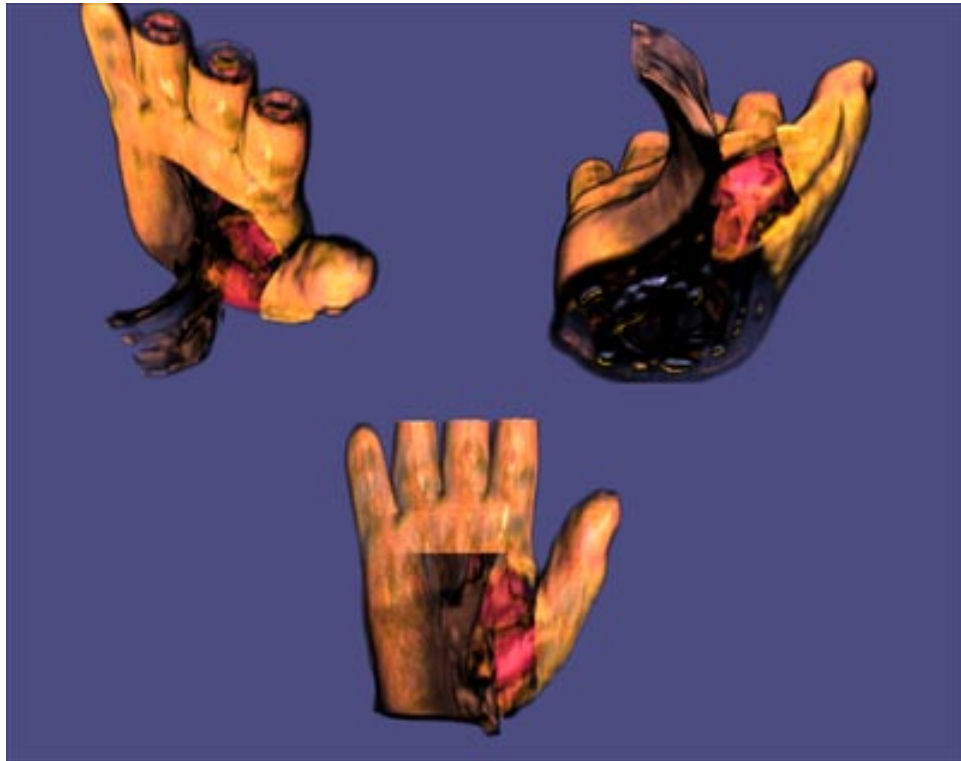


Figure 6.11: This figure shows the results of collecting MRI data, classifying each voxel in the volume data using the partial volume mixtures algorithm, and creating solid parts using the material information. We deform the outer layers to peel the skin back showing internal structure. Chapter 7 describes the rendering process used to create this image. □

animation are shown.

The kinematically-specified deformations are defined with the same type of rectangular control-point grid. Instead of using simulation output, however, we specify the control points kinematically. Figure 6.11 shows an example where the skin is peeled back from the palm of a human hand model to show internal anatomy. Internal materials are shown in different colors to differentiate them. The hand dataset was classified into air, tendon, muscle, fat and skin. These images were rendered directly from the volume dataset and the description of the deformation using a new algorithm detailed in Chapter 7.

## 6.3 Conclusion

Through a sequence of examples we have shown that classified MRI volume data can be used to create both static and dynamic models. While the resolution of conventional MRI data is somewhat less than that of surface measurement techniques, it is sufficient to create many types of models, and the internal measurements available make dynamics more accurate for models with interior structure.

By creating a series of geometric models we have determined a number of requirements for the earlier steps in our computational framework. First, because real-world objects contain more than one material, we need to be able to identify and separate the multiple different materials in our sampled datasets. Isosurfaces do this in unclassified MRI data only for exactly two materials, and only if the boundary between them is at a consistent and known value. Through classification we can define isosurfaces for each material. Together the surfaces combine to represent all of the material-material boundaries. Our classification process also provides a physical interpretation for the data that defines a choice of isovalue for calculating a surface.

While many classification algorithms work well at identifying materials within regions of pure materials, they do not produce accurate results where materials meet one another. Our investigations have motivated the need for classification algorithms that are accurate at these boundaries. The boundaries are where surface models are defined, and errors there cause artifacts in the extracted models. Our new classification techniques reduce these artifacts significantly.

Third, there must be sufficient information in the collected data for our classification algorithms to identify boundaries. We have translated this requirement into a contrast-to-noise goal in the goal-based collection process.

Fourth, our model-extraction techniques find isosurfaces in continuous functions. If collected data does not satisfy the Nyquist sampling theorem, then any continuous function that we reconstruct from the samples will have aliasing and hence lead to artifacts in the extracted model.

## Chapter 7

---

# Deformed Volume Rendering

---

In this chapter we present a method for directly rendering deformed volume data. Deformations are a technique for simulating the behavior of flexible bodies, as we outlined in the previous chapter. The new rendering method gives us a way to create images showing the simulated behavior. Figure 7.1 shows an example of volume data of a human hand with the skin peeled back to show internal structure.

### 7.1 Introduction

We describe a rendering algorithm that is applicable to volume rendering algorithms that use ray tracing techniques. Our approach extends these algorithms by directly ray tracing deformed volumes. We inversely transform each ray into the undeformed coordinate system of the dataset and then perform the volume ray tracing integration along that curved path. Figure 7.3 illustrates this process with a ray on the right and its inverse image on the left.

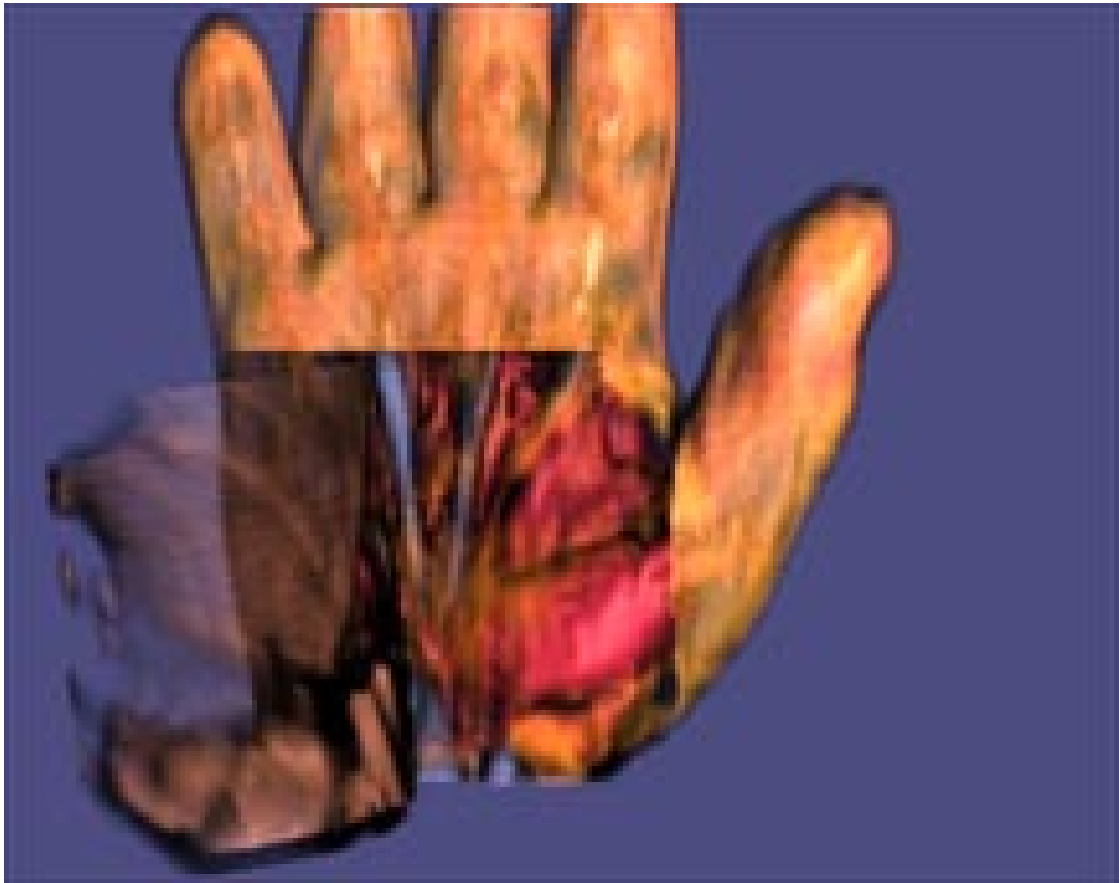


Figure 7.1: Volume-rendering of a three-dimensional MRI dataset of a human hand with the “skin” kinematically peeled away from the rest of the hand. Figure 7.6 shows a slice through the dataset with different materials identified, and a rendered image of the undeformed data. □

### 7.1.1 Related Work

**Volume rendering.** Computer graphics rendering has historically dealt with surfaces and a large body of research has concentrated on rendering surfaces [Foley et al., 1990] [Kajiya, 1986]. As computational and storage capacity have increased and volume imaging technologies have been developed, volume datasets have become practical. As a consequence, techniques for rendering these volumes directly have been developed [Drebin et al., 1988] [Upson and Keeler, 1988] [Sabella, 1988] to replace those that converted the volume data to surface, curve, or point primitives.

Some of these volume rendering techniques operate much like traditional ray tracing: by intersecting rays with the volume and accumulating contributions into each pixel. While slower

than some other techniques, ray tracing often has the advantage of producing more informative results with sophisticated lighting models that include visual cues such as shadows.

**Deformations.** Deformations are a powerful tool for manipulating volume datasets. Deformations generalize rigid body (affine) transformations and can model flexible behavior. They can be produced from flexible body simulations of models representing objects in a volume dataset [Laidlaw, 1992a]. They can also be created as part of a modeling system and applied to synthetically generated volume data produced by a sculpting system [Sederberg and Parry, 1986] [Coquillart, 1990] [Galyean and Hughes, 1991] [True and Hughes, 1992] or other modeling methods.

### 7.1.2 Our Approach

We augment volume ray tracing techniques by introducing a method to directly render deformed volumes. Our algorithm can be incorporated into a volume ray tracer as a modification of the data sampling step.

Our technique is an alternative to resampling the deformed dataset and then rendering the resampled, undeformed version. For a deformation that changes over time our technique may be advantageous because it does not require creating a resampled dataset for each time step. This can be a significant advantage for rendering an animation, especially if motion blur is used. It can also be an advantage for adjusting deformations interactively because a separate, resampled dataset is not required for each modification of the deformation. Finally, because our algorithm scales in computation time with the number of pixels rendered, and resampling scales in time with the size of a volume dataset, our algorithm is more efficient for small images or large datasets.

Uniform resampling of a deformed dataset causes either oversampling where the data is expanded or undersampling where it is compressed. Oversampling requires more storage space for the resulting dataset, and undersampling may lose information. Our algorithm avoids these potential problems by using the original data, saving the storage and maintaining the original information. We do not address the sampling issues involved in the volume rendering algorithms, but instead



provide all of the original information in the dataset for those algorithms to operate on.

Our technique may perform more slowly than a resampling approach in cases where a small number of deformations of a dataset are rendered many times. In this case, the storage and time needed to resample the dataset are probably worthwhile. Our implementation is also likely to be more complex than resampling a dataset, although resampling a deformed dataset without introducing artifacts is non-trivial.

Our work is similar to [Barr, 1984] and [Barr, 1986] because it operates in the coordinate system of an undeformed object. It differs by calculating the path through the undeformed space rather than finding a single surface intersection between an inversely deformed ray and an object.

### 7.1.3 Overview

Section 7.2 defines terms and presents notation that we use to describe our algorithm. In Section 7.3 we present the algorithm, which uses interval methods [Moore, 1979] [Snyder, 1992] to find intersections with the boundary of a deformation, and then numerically solves a differential equation to find the rest of the inverse ray path through the undeformed dataset. Section 7.3.3 discusses some implementation considerations. In Section 7.4 we illustrate the technique with volume rendered images of deformed datasets and summarize our results.

## 7.2 Terms and Definitions

This section defines terms and notation that we will use to describe our algorithm.

### 7.2.1 Interval Methods

We give a brief review here of interval terminology. For more details see [Moore, 1979]. An *interval* is a range over the real numbers. We use a bar, ‘ $\bar{\phantom{x}}$ ’, over a variable to indicate an interval.

Given a function  $f(x) : R \Rightarrow R$ , an *inclusion function*,  $\square f(\bar{x})$ , of  $f$  returns an interval guaranteed to contain the image of the interval  $\bar{x}$ . An inclusion function must also have the property that the

output interval can be made arbitrarily small for some input interval around a given point. Inclusion functions generalize in a straightforward way to higher dimensions.

*Interval methods* use inclusion functions for solving problems robustly [Snyder, 1992]. Inclusion functions provide bounds for mathematical operations and so can be used to guarantee that some property of an algorithm is true.

### 7.2.2 Volume Rendering

We model a dataset as a function

$$v(\vec{x}_{body}) : R_{body}^3 \Rightarrow R^m \quad (7.1)$$

where  $m$  is the dimensionality of the dataset.

An affine transformation is often employed to place, scale and orient a dataset. We define this as a function

$$\vec{M}(\vec{x}_{body}) : R_{body}^3 \Rightarrow R_{world}^3 \quad (7.2)$$

Note that this can be implemented as a matrix operation using homogeneous coordinates [Foley et al., 1990].

We define a ray as

$$r(\hat{s}) : R \Rightarrow R_{world}^3 \quad (7.3)$$

The inverse of the affine transformation applied to that ray gives another ray in the coordinate system of the dataset

$$\vec{P}(s) = \vec{M}^{-1}(r(s)) \quad (7.4)$$

We use the following volume rendering equation to model the operation of most ray tracing volume renderers.

$$I(s) = \int_0^s e^{-\int_0^{\hat{s}} f(\vec{P}(\hat{s}), v(\hat{s})) d\hat{s}} g(\vec{P}(\hat{s}), v(\hat{s})) d\hat{s} \quad (7.5)$$

where  $f(\hat{s})$  and  $g(\hat{s})$  are functions that model light interacting with material at a point in space. See

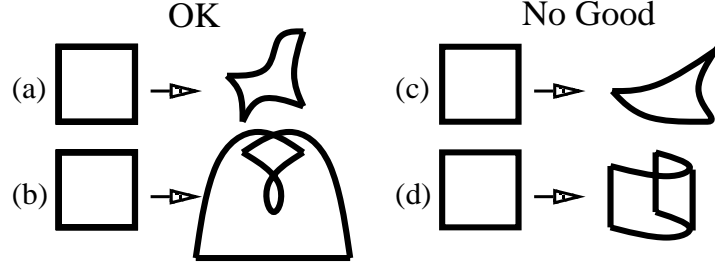


Figure 7.2: Examples of deformations from  $R^2 \Rightarrow R^2$ . Note that these deformations lie completely within the plane. Examples (a) and (b) satisfy the derivative existence and invertibility condition. (c) maps a line segment to a point creating a non-invertible Jacobian, and (d) has a singular Jacobian along the silhouette edge of its fold.  $\square$

[Danskin and Hanrahan, 1992] for more details on this equation. We do not discuss this equation further, except to describe how we modify  $\vec{P}$  to integrate through deformed datasets.

### 7.2.3 Deformations

A deformation generalizes the affine transformation  $\vec{M}(\vec{x}_{body})$ . A deformation can be defined globally, over the entire range of  $R^3_{body}$ , or over only a portion. Currently, we use deformations defined over finite regions.

$S_{body} \subset R^3_{body}$  is the region over which a deformation is defined. The deformation

$$D(\vec{x}_{body}) : S_{body} \subset R^3_{body} \Rightarrow R^3_{world} \quad (7.6)$$

maps the undeformed space containing the dataset into world coordinates. We define  $b_{body}$  as the boundary of  $S_{body}$ .  $S_{world} = \vec{D}(S_{body})$  is the image of the volume of the deformation and  $b_{world} = \vec{D}(b_{body})$  is the image of the boundary of the deformation under  $\vec{D}(\vec{x}_{body})$ . Figure 7.3 shows these relationships for a simple two-dimensional deformation.

We define  $\mathbf{J}(\vec{x}_{body})$  as the Jacobian of  $\vec{D}(\vec{x}_{body})$ , i.e.:

$$\mathbf{J}_{ij}(\vec{x}_{body}) = \frac{d}{dx_j} D_i(\vec{x}_{body}) \quad (7.7)$$

We require that two conditions be met by the deformation. First, the derivative of  $\vec{D}(\vec{x}_{body})$ ,

$\mathbf{J}(\vec{x}_{body})$ , must exist and be invertible and continuous in  $S_{body}$ . This rules out deformations that squeeze a line or area into a single point, as well as deformations that switch handedness, or “fold over” on themselves. Figure 7.2 gives some examples of two-dimensional deformations that satisfy and violate this constraint. Second, we must have an inclusion function  $\square \vec{D}(\vec{x}_{body})$  for  $\vec{x}_{body} \subset b_{body}$ .

The path through the dataset is now redefined, using the deformation in place of the affine transformation:

$$\vec{P}(s) = \vec{D}^{-1}(r(s)) \quad (7.8)$$

We have implemented our algorithm using deformations specified as tricubic B-splines [Bartels et al., 1987] over rectangular solid regions of  $R^3_{body}$ . These rectangular solids can be chosen to surround the data, and can abut with one another to generate more complex deformations than can be specified over a single rectangular solid. Each rectangular solid has 64 control points, and shares 48 with each neighbor in order to enforce  $C^2$  continuity across the boundary.  $b_{body}$ , the boundary of the deformation, is the set of rectangular faces that are not shared. In Figure 7.3 and Figure 7.4 a single rectangle is used to define each deformation. For Figure 7.1 a  $4 \times 4$  grid of 48 rectangular solids and an additional three separate rectangular solids define the deformation.

We have implemented an inclusion function for these deformations using interval arithmetic and the mean-value form [Moore, 1979].

### 7.3 Algorithm

In this section we describe how to find the inversely deformed path through  $R^3_{body}$  of a ray in  $R^3_{world}$ . Figure 7.3 shows a simple, two-dimensional example. There are a few potential complications in finding the path. First, parts of the inversely deformed path may not lie within any part of the deformation. In the figure, the segment  $VW$  is an example. Second, different parts of a ray may map to separated curve segments within  $R^3_{body}$ , as with segments  $UV$  and  $WX$ . And finally, for a deformation like case (b) in Figure 7.2, parts of a ray can lie in more than one segment

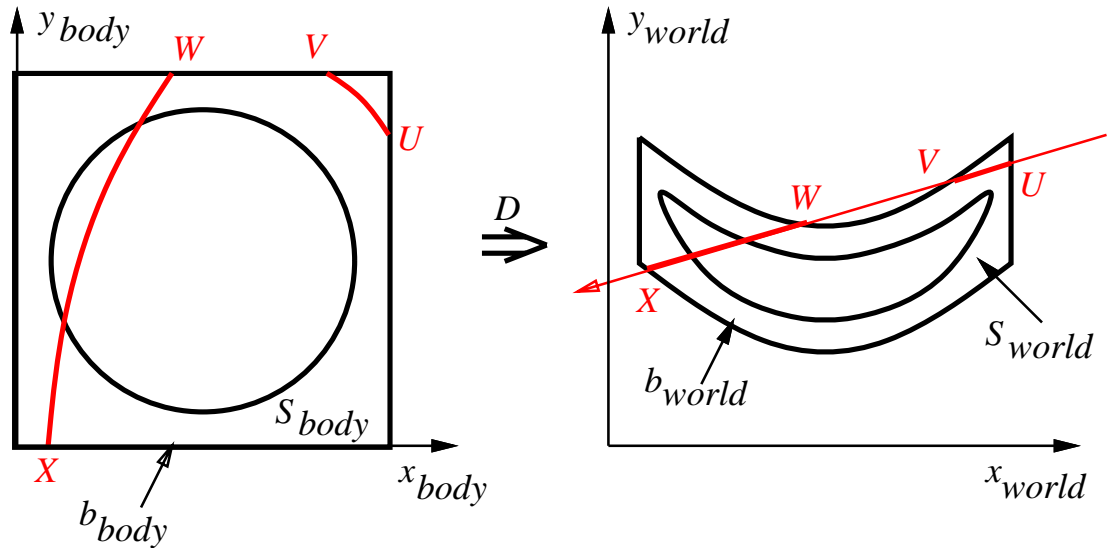


Figure 7.3: A simple two-dimensional deformation. On the left, a circle is enclosed by a square, which is the portion of  $R^2_{body}$  that will be deformed. On the right, that square and its contents have been deformed to flatten and bend the circle. A ray is shown on the right with the corresponding segments  $UV$  and  $WX$  mapped back onto the undeformed volume. A similar deformation produced the three-dimensional object in Figure 7.4 by flattening and bending a cube containing a spherically symmetric sampled dataset.  $\square$

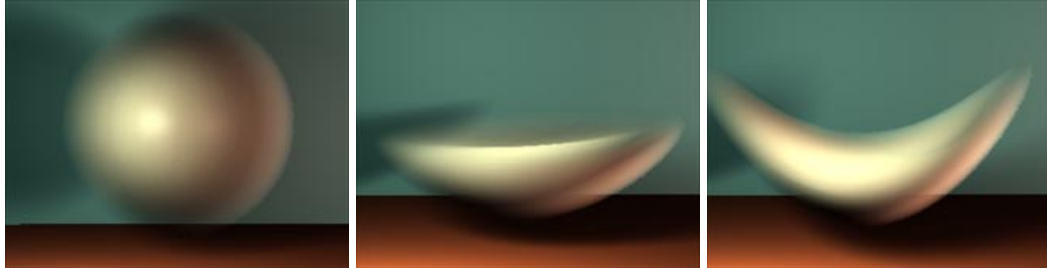


Figure 7.4: Volume-rendered images of an undeformed, spherically symmetric dataset on the left and two deformations of that dataset in the center and on the right. A two-dimensional analog of the deformation is shown in Figure 7.3.  $\square$

simultaneously.

To solve the problem we first find all intersections of the ray with  $b_{world}$ , the image of the boundary of the deformation. Section 7.3.1 describes this process in detail. In Figure 7.3 this step finds all four points,  $U$ ,  $V$ ,  $W$ , and  $X$  on the top edge of the deformation. We pair the intersections into “segments,” where each segment represent a contiguous piece of a ray within the deformation. Each segment contains a starting and ending distance,  $s$ , along the ray and a starting point in  $S_{body}$  for the segment.

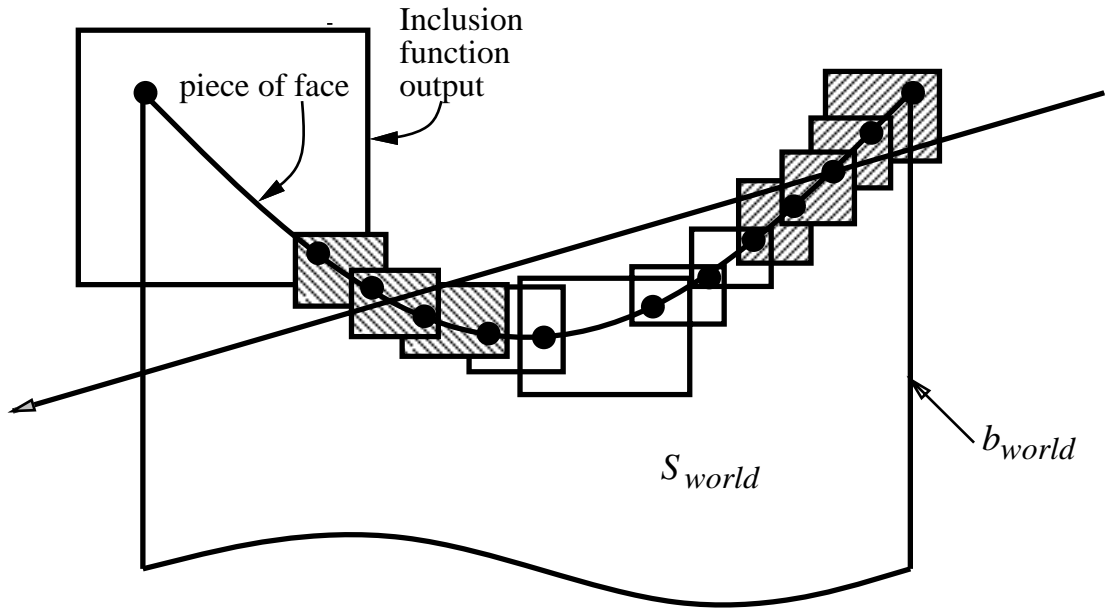


Figure 7.5: Inclusion function example for Figure 7.3. The curve along the top of  $S_{world}$  is a *face* of the deformation. We recursively divide that face into pieces to find the intersection of a ray with the face. The pieces of the face are shown separated by dots in the diagram. For each piece we calculate an inclusion function, shown as a rectangle around each piece, guaranteed to contain the portion of the face. We intersect the ray with the rectangle and subdivide further if there is an intersection. Otherwise we can ignore that piece of the face. Gray rectangles intersect the ray, and white ones do not. Note that unshaded portions of the face do not need to be subdivided as finely as others, since the inclusion function guarantees there is no intersection.  $\square$

For each of these segments we set up a differential equation for  $\vec{P}(s)$ . Section 7.3.2 describes this process. As we increment  $s$  along a ray for the volume-rendering integral, we check to see if  $s$  is within the segments along the ray. If so, we look up the data value  $v(\vec{P}(s))$  using the solution to the differential equation for that segment. If more than one segment is active, then the data values can be added, averaged, or otherwise combined. If  $s$  is not within any segment, then we are outside the deformation, and we return the value that  $v(\vec{x}_{body})$  returns outside of the dataset.

### 7.3.1 Finding All Boundary Intersections

In this section we describe how to find all intersections of a ray with the boundary  $b_{world}$  in  $R_{world}^3$  and how to group them together into segments. Figure 7.5 shows a two-dimensional example for a single face of a deformation.

We use the inclusion function  $\square \vec{D}(\vec{x}_{body})$  to find all intersections. We evaluate the inclusion function for each rectangular face of the boundary in  $R_{world}^3$ . The interval result is a three-dimensional interval in  $R_{world}^3$ . For example,  $\square \vec{D}([x_0, x_1], [y_1, y_1], [z_0, z_1])$  returns an interval in  $R_{world}^3$  containing the image of the face where  $y = y_1$ . If the ray  $\vec{r}(s)$  intersects the interval in  $R_{world}^3$ , we save the intersection and boundary information in a priority queue indexed by the nearest value of  $s$  within the  $R_{world}^3$  interval.

Once all the faces that the ray might intersect are in the priority queue, we remove them one at a time. If the current candidate is sufficiently small, we save it in a list of potential intersections. If not, we subdivide it in half in each direction, repeat the interval evaluation for the smaller range, and repeat the ray intersection test for the smaller  $R_{world}^3$  interval. The new, smaller intervals may or may not intersect the ray, so we save the intersection and boundary information only for those  $R_{world}^3$  intervals that do. Figure 7.5 shows an example of the lowest-level intervals that are tested by this procedure. The large interval in the upper left is discarded early, because it does not overlap the ray. The final list of potential intersections is represented by the shaded boxes.

We repeat until the priority queue is empty, and then construct segments from the list of potential intersections. We are interested in pairing together each entrance with an exit, and we start by identifying each potential intersection as one or the other. We use the surface normal in  $R_{world}^3$  and compare it with the ray direction. For the  $y = y_1$  face,

$$\vec{N}(x, y_1, z) = \frac{\partial \vec{D}}{\partial x}(x, y_1, z) \wedge \frac{\partial \vec{D}}{\partial z}(x, y_1, z) \quad (7.9)$$

$$\vec{N}(x, y_1, z) \cdot r_d < 0 \Rightarrow \text{entering} \quad (7.10)$$

and similarly for the other faces.

Each intersection can be represented by more than one potential intersection in the list because the inclusion functions are always larger than the actual function values. Once we have subdivided so that the size of the intervals is smaller than the error tolerance threshold of our renderer, we coalesce potential intersections that are all entering or exiting and that have overlapping  $R_{world}^3$

intervals into a single potential intersection. Finally, we pair together entrances and exits into segments. For each segment we save the start value,  $s_0$ , the end value,  $s_1$ , and the initial point,  $\vec{P}(s_0) \in R_{body}^3$ , where the ray first intersects the deformation.

### 7.3.2 Calculating the Path Through the Dataset

In Section 7.6 we derive the following differential equation to solve for the path  $\vec{P}(s)$  through  $R_{body}^3$ :

$$\frac{d\vec{P}}{ds}(s) = [\mathbf{J}(\vec{P}(s))]^{-1} \frac{d\vec{r}}{ds}(s)k. \quad (7.11)$$

We set this up as an initial value problem (IVP) rather than as a boundary value problem (BVP) for several reasons. First, solving a BVP is more complex and slower. Second, a BVP solver must solve for the entire path to evaluate any of it. We often only need to integrate part of the way along the ray, since further points may be occluded by material, and using an IVP allows us to do this incrementally. We find that it is reasonable to trade these advantages off against the loss in accuracy as we move along the ray. By adjusting the accuracy of the IVP solution, we can limit this loss to an acceptable amount.

We start the solution at  $s_0$  with value  $\vec{P}(s_0)$ , using the values from the segment we saved in Section 7.3.1.

We solve this equation with a Runge Kutta [Press et al., 1992] and Adam's method [NAG, 1993] differential equation integrators.

### 7.3.3 Implementation Considerations

We discuss a few implementation details in this section.

First, because of inaccuracies in numerical integration, and because many numerical integrators evaluate a derivative function slightly outside the range of its solution, the Jacobian for our deformations must be defined slightly outside of  $S_{world}$ . In order to maintain a continuous, invertible Jacobian we project any evaluation point outside of  $S_{body}$  into the nearest deformation domain



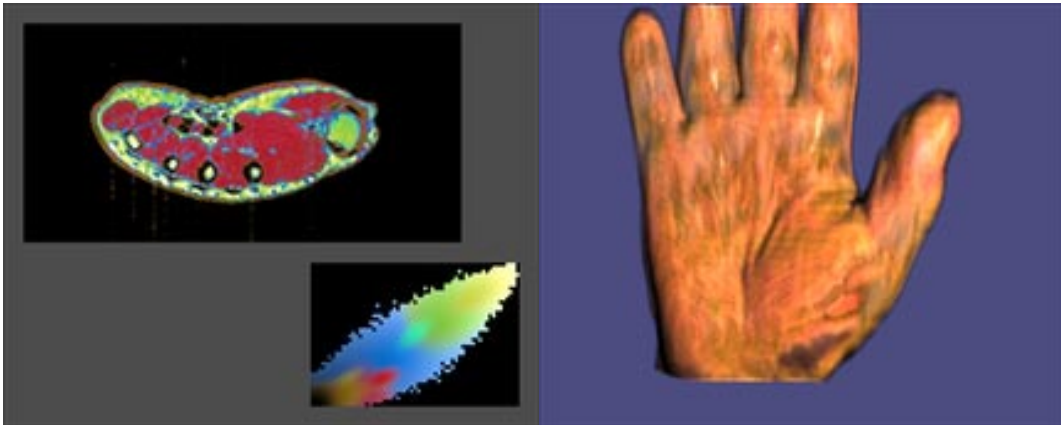


Figure 7.6: Classified data, colored histogram, and image of undeformed hand dataset shown deformed in Figure 7.1. The top left image shows one slice from a three-dimensional MRI dataset of a human hand. At each spatial point we have two data values. The plot in the lower left shows a top view of the 2-dimensional histogram of that data, with MRI values along the left and bottom axes and values for different materials given different colors. The slice has those colors applied to it, with skin orange, muscle red, fat and bone marrow yellow/green, and tendon black. The right image shows the same dataset volume-rendered.  $\square$



Figure 7.7: A photograph of a jade plant, a volume rendering of undeformed data collected from the jade plant, and a volume rendering of that data deformed. The right-hand image is one frame from those shown in Figure 6.9  $\square$

boundary point and use the Jacobian value there.

Second, we have found that the interval evaluation for finding intersections is the most costly part of our implementation. We have significantly increased performance by caching the interval calculations for the first three levels of the subdivision hierarchy.

Third, our initial rays must start outside of a deformation in order to find their initial intersection points. The interval methods could be extended to find an initial point within the deformation, but our implementation does not do this. Rays created within a volume must start with “pseudo-entrance” intersections for each segment active at the point the new ray was spawned. The intersection-finding algorithm will then pair them up with exiting intersections to create segments for the new ray.

## 7.4 Results

We have shown several examples of volume datasets directly rendered with deformations. Figure 7.1 shows MRI volume data classified to identify skin, fat, muscle, tendon, and bone. The skin is deformed to peel it back from the other materials, showing the interior structure of the dataset. Figure 7.6 shows a single slice through the dataset with materials identified by their colors, and a rendering of the hand with no deformation. The dataset was classified using the partial volume mixtures algorithm.

Figure 7.4 illustrates a rendering of simple deformations applied to a simulated MRI dataset of a solid ball.

Figure 7.7 shows a photograph of a living jade plant, an undeformed rendering of MRI data collected from the jade plant, and a deformed version of the jade plant rendered with our algorithm. The deformation was calculated as one frame of an animation showing how a jade plant might move (see Figure 6.9).

## 7.5 Conclusion

We have described an algorithm for directly ray tracing deformed volume data. The algorithm inversely deforms each ray and traces its curved path through the undeformed data. We have shown several examples of images rendered using our implementation.

There are several advantages to directly ray tracing deformed volumes. As an alternative to creating a new regularly sampled dataset by resampling the deformed one, our technique provides a more concise representation for a deformed volume. This conciseness is particularly useful for multiple deformations, or for deformations that vary over time. The space savings is also a benefit when rendering small images of large datasets, because it is proportional to the size of the dataset, while the run-time cost is proportional to the size of the image. Our technique also avoids the oversampling or undersampling that is implied by resampling a deformed dataset.

While the implementation increases rendering time in our volume ray tracer by a factor of two

to three, we have several avenues to explore for speeding the calculation. Because most of the cost is in finding intersections, we propose implementing tighter inclusion functions, using an interval Newton method to converge on a solution more quickly. We could also exploit coherence more in the interval evaluations by adaptively caching them in addition to the static caching of the first three subdivision levels.

---

## 7.6 Derivation of Deformed Path

We derive the differential equation in Section 7.3.2 here. The derivation is in Einstein Summation Notation (ESN) [Blinn, 1992].

$\vec{P}(s) = \vec{D}^{-1}(\vec{r}(s))$  is a portion of the path in  $R_{body}^3$ . It is only defined where  $\vec{D}^{-1}(\vec{r}(s))$ . This is where the ray is within  $S_{world}$ . In those regions, by definition:

$$\vec{P}_i(s) = \int_0^s \frac{d\vec{P}_i}{ds}(s) ds + \vec{P}_i(s_0) \quad (7.12)$$

Differentiating and rewriting the integrand using the definition of  $\vec{P}$  and the chain rule,

$$\frac{d\vec{P}_i}{ds}(s) = (D^{-1})_{i,j}(r(s)) r_{j,s}(s) \quad (7.13)$$

Because we restrict the Jacobian of the deformation to be invertible at all points, the derivative of the inverse deformation is the matrix inverse of the Jacobian of the deformation.

$$(D^{-1})_{i,j}(\vec{x}_{world}) = \left( [\mathbf{J}(\vec{x}_{body})]^{-1} \right)_{ij} \quad (7.14)$$

so Equation 7.13 becomes:

$$\frac{d\vec{P}_i}{ds}(s) = \left( [\mathbf{J}(P(s))]^{-1} \right)_{ij} r_{j,s}(s) \quad (7.15)$$

Note that the argument of  $\mathbf{J}$  is the path location in  $R_{body}^3$ ,  $P(s)$  and that we have a known initial condition at  $P_i(s_0)$ .

## Chapter 8

---

# Conclusions and Future Work

---

This chapter summarizes our work and presents conclusions in the first section and then discusses some future research directions that our work suggests may be fruitful.

### 8.1 Conclusions

We have addressed the problem of creating geometric models of real-world objects. This is a major problem in computer graphics, and our results have applications in scientific research, education, and entertainment. We have chosen to use MRI as our measurement modality because it is relatively non-invasive, measures chemical properties of living subjects very well, and provides us with measurements of internal structure.

We have presented a computational framework for creating geometric models and images from MRI data. The framework consists of three main steps. The first is data collection; the second, tissue classification; and the third, model-building and visualization. Within the stages of the framework we have implemented a number of new algorithms that help to make models and images. We outline

the results of our new algorithms and the interactions between them in this section.

### 8.1.1 Goal-based Data Collection

The novel contributions of our new paradigm for choosing MRI collection parameters are in its goal-based framework, in the choice of goals for the optimization procedure, and in the use of the optimization step to steer the acquisition process during acquisitions. Our framework provides a methodology for adding goals and new protocols to the set that we have implemented. The goals we implement are motivated by our desire to distinguish adjacent materials sufficiently well to be able to produce geometric models from the data. Many of the objectives are also generally applicable to applications such as medical or biological imaging. These goals differ from other work in that they do not find parameters yielding the most contrast or highest contrast-to-noise ratio, but rather find parameters yielding *sufficient* contrast in the least amount of time. Any number of materials can be specified by a user from low-resolution test datasets, and optimal collection parameters are generated taking into account inherent machine limitations and fixed parameters such as field of view and resolution. Finally, because values of the function we optimize are consistent from protocol to protocol, we can compare them and choose the most appropriate protocol or combination, independent of whether it produces scalar or vector-valued data.

### 8.1.2 Bayesian Classification

In the second stage of our computational framework we have developed a new methodology for creating Bayesian classification algorithms from assumptions about the data-collection process. Using the methodology we have created three new algorithms for classifying scalar and vector-valued volume data. Our algorithms use a continuous reconstruction of the dataset and calculate a continuous histogram of the data over regions representing each voxel. We derive intensity probability density basis functions for both pure materials and mixtures of materials due to the band-limiting effects of the data-collection process. Our classification process models histograms over voxel regions using the material and mixture basis functions and uses a probabilistic approach

to fit the parameterized models to a histogram over each voxel.

In the partial volume mixtures approach, we modeled each voxel as a linear combination of pure materials and mixtures of two materials. In the two boundary distance approaches we formulated a more accurate model of voxels near boundaries between pure materials. The boundary distance approaches classify voxels near boundaries more accurately, but at a larger computational cost.

We demonstrated the success of our techniques on simulated and real data by classifying datasets of a human hand, human brains, and a bee, among others.

### **8.1.3 Model-Building and Visualization**

Through a sequence of examples we have shown that classified MRI volume data can be used to create both static and dynamic models. The level of detail in the models is somewhat less than can be produced with surface scanning techniques, but the inclusion of internal structure adds significantly more information to volume models and makes dynamic simulations more accurate. With the internal structure, the behavior of different internal materials such as bone, muscle, and fat can be taken into account.

We have also presented a new algorithm for directly rendering deformed volume data. This is particularly useful for creating images of flexible-body simulations because it avoids the storage cost and resampling difficulties inherent in creating a new sampled dataset for each step in a time-varying deformation of volumetric data.

### **8.1.4 Interaction of Framework Stages**

Throughout our investigations we have discovered that each stage of the framework mandates certain conditions on the results of earlier stages. Starting with the model-extraction and visualization stage of our pipeline, requirements feed back and influence earlier stages. This stage requires that its input volume data identify different materials and the boundaries between them.

We infer from this requirement a need to classify the data that we collect, and to use an algorithm that works well at boundaries between materials. Our new algorithms address this problem with

more accuracy than previous methods.

The classification algorithms also place requirements on the data that we collect. The materials and boundaries between them must be distinguishable in the data. We translate this into a contrast-to-noise ratio goal within our goal-based data-collection process.

The model extraction and classification algorithms also require that we reconstruct a continuous function from datasets, and so we require that the data we collect satisfy the Nyquist sampling theorem.

The feedback of these requirements to the earlier stages of the framework helps tailor results to the geometric modeling problem, providing us with tools that create more accurate geometric models.

## 8.2 Extensions

Our work suggests a number of directions to consider for future research. We organize them here in the context of our model-building framework.

### 8.2.1 Goal-based Data Collection

Within the goal-directed data-collection domain, we would like to extend the repertoire of collection protocols and goals. Extending the protocols includes incorporating more collection parameters, such as tip angle and sweep width (see Table 2.1), into the optimization process, as well as adding to the list of protocols that can be supported. Using the technique on a wider variety of examples will give us more feedback on its efficacy in providing us with data that will be useful for studying anatomy and development.

Extending the goals includes formulating more goals for disparate uses of MRI data. The imaging goal of achieving a particular contrast-to-noise ratio serves our classification algorithms well, but might not be the best goal for other applications.

Our framework should also prove useful in choosing concentrations of MRI contrast agents to



enhance particular materials. By modeling the effect of various concentrations of a contrast agent on materials and incorporating that model into our goal-based framework, we can tailor the contrast agent concentration to achieve better-quality data in less time.

The model of the MRI process we used is somewhat limited. It does not take into account the mixing of multiple materials within a single voxel measurement, and would be somewhat difficult to derive for a new protocol. Extending the model to include multiple materials might be a useful project. The implementation of this should be straightforward, using the same Levenburg-Marquardt non-linear parameter estimation technique.

We could also model the MRI process by numerically solving the Bloch equations [Bloch, 1948] to predict data values as a function of protocol parameters. This would have the advantage of working for an arbitrary protocol, as long as we can define the protocol in terms of a pulse-program whose behavior is modeled well by the Bloch equations.

Through the numerical solution of the Bloch equations, it might be possible to generate new pulse-programs via a genetic algorithm that evolved pulse programs and evaluated their effectiveness via our objective function.

### 8.2.2 Artifacts in MRI Data

While we have addressed some of the artifacts that occur in MRI data, there are a number that we have chosen to ignore. Different materials have different magnetic properties and boundaries between them that cause *susceptibility* artifacts in MRI images. These artifacts occur primarily at boundaries between materials or near accidental air bubbles, which tend to stick to these boundaries. The artifacts are bright and dark patterns with a characteristic appearance within the data.

We could compensate for effects near boundaries with an extension to our boundary distance classification algorithm, since information about the boundary is calculated as part of the algorithm. The characteristic appearance of the artifacts caused by bubbles could be mitigated as a pre-processing step or as part of the classification process.

Nonlinearities in the gradient coils used to encode spatial information in MRI data can lead to

datasets with geometric distortions. We have not addressed geometric distortion in this work, except to avoid its manifestations through judicious size and placement of the objects that we measure. In principle, however, we should be able to compensate for these distortions through calibration of a particular MRI machine. By understanding the errors in the underlying static magnetic field and the gradients superimposed on it, we can model the geometric distortion created by those errors and compensate for it.

### 8.2.3 Classification

Our classification algorithms have proven useful on the examples that we have applied them to, but we would like to try them on more types of data in order to learn more about their characteristics and breadth of applicability. Classifying data in an atlas of MRI datasets of a particular animal could provide interesting results, both in the classified data itself and in feedback about the algorithms. Our algorithms also should prove accurate at estimating volumes, especially for small regions where errors near boundaries are significant compared to the entire volume.

There are a number of extensions to the classification algorithms we would like to suggest. We have interpolated neighboring samples in classifying voxels, but would like to take further advantage of this local geometric information. Incorporating the geometric information into the prior probabilities for each voxel should help to avoid single misclassified voxels without losing detail information that post-classification filtering processes destroy.

Another possible method for incorporating more geometric information into the classification process would be to define a new type of voxel-info with that information and to derive a classification algorithm based on that data. Combining the histogram voxel-info that we have implemented with new voxel-info should produce better results than either alone.

Deriving new histogram basis functions would enable the algorithms to better classify data by explicitly handling more situations. We would like to relax the assumption that objects consist of regions of uniform materials. We can parameterize the histogram basis functions by the relative content of each material, and anticipate a more continuous classification that would introduce fewer

artifacts. We would also like to derive basis functions for geometries other than the pure and surface-boundary cases that we have implemented. While these are the two most common geometries, edges where three materials come together, points where four materials meet, and features like membranes that are thinner than our sampling rate also occur and are important within the context of geometric models.

Finally, two future directions for research include implementation of the boundary distance algorithm to incorporate non-uniform response of materials within the sampled volume and acceleration of our classification algorithms.

#### **8.2.4 Model Building and Simulation**

Our model-building and simulation work also implies a number of directions for augmentation. One particularly interesting direction is in modeling and simulating the behavior of complicated flexible bodies. This goal has inspired much of the work in this thesis, particularly the use of MRI data to measure the internal structure of objects in addition to their external structure.

Future research could include a testbed for flexible-body simulations that incorporates new types of constraints for sliding flexible bodies over one another without interpenetration and for making structural connections between both flexible and rigid bodies. This type of simulation environment would provide a predictive tool with medical, and scientific applications, and could be used for entertainment purposes as well.

#### **8.2.5 Volume Rendering**

Volume rendering is a relatively new technique and holds a lot of promise for generating images with visual information and cues that can improve understanding of the objects being rendered. New techniques that generate different types of images through new, more general models of light propagation through materials have solid research potential. Textures and translucency within volumes of materials hold promise in generating these new looks.

**8.3 Summary**

Our work on a computational framework for creating geometric models from MRI volume data has demonstrated the utility of the framework, led to a number of algorithmic results, and indicated many avenues for future research.

# Bibliography

- [Baraff and Witkin, 1992] Baraff, D. and Witkin, A. (1992). Dynamic simulation of non-penetrating flexible bodies. In Catmull, E. E., editor, *Computer Graphics (SIGGRAPH '92 Proceedings)*, volume 26, pages 303–308.
- [Barr, 1984] Barr, A. H. (1984). Global and local deformations of solid primitives. In Christiansen, H., editor, *Computer Graphics (SIGGRAPH '84 Proceedings)*, volume 18, pages 21–30.
- [Barr, 1986] Barr, A. H. (1986). Ray tracing deformed surfaces. In Evans, D. C. and Athay, R. J., editors, *Computer Graphics (SIGGRAPH '86 Proceedings)*, volume 20, pages 287–296.
- [Bartels et al., 1987] Bartels, R., Beatty, J., and Barsky, B. (1987). *An Introduction to Splines for Use in Computer Graphics and Geometric Modeling*. Morgan Kaufmann Publishers, Palo Alto, CA.
- [Blinn, 1992] Blinn, J. F. (1992). Uppers and downers. *IEEE Computer Graphics and Applications*, 12(3).
- [Bloch, 1948] Bloch, F. (1948). *Physical Review*, 70.
- [Choi et al., 1991] Choi, H. S., Haynor, D. R., and Kim, Y. M. (1991). Partial volume tissue classification of multichannel magnetic resonance images - a mixel model. *IEEE Transactions on Medical Images*, 10(3):395–407.

- [Clarke et al., 1995] Clarke, L. P., Velthuizen, R. P., Camacho, M. A., Neine, J. J., Vaidyanathan, M., Hall, L. O., Thatcher, R. W., and Silbiger, M. L. (1995). Mri segmentation: Methods and applications. *Magnetic Resonance Imaging*, 13(3):343–368.
- [Cline et al., 1990] Cline, H. E., Lorensen, W. E., Kikinis, R., and Jolesz, F. (1990). Three-dimensional segmentation of mr images of the head using probability and connectivity. *Journal of Computer Assisted Tomography*, 14(6):1037–1045.
- [Coquillart, 1990] Coquillart, S. (1990). Extended free-form deformation: A sculpturing tool for 3D geometric modeling. In Baskett, F., editor, *Computer Graphics (SIGGRAPH '90 Proceedings)*, volume 24, pages 187–196.
- [Danskin and Hanrahan, 1992] Danskin, J. and Hanrahan, P. (1992). Fast algorithms for volume ray tracing. *1992 Workshop on Volume Visualization*, pages 91–98.
- [Drebin et al., 1988] Drebin, R. A., Carpenter, L., and Hanrahan, P. (1988). Volume rendering. In Dill, J., editor, *Computer Graphics (SIGGRAPH '88 Proceedings)*, volume 22, pages 65–74.
- [Dreher and Bornert, 1988] Dreher, W. and Bornert, P. (1988). Pulse sequence and parameter choice in nmr imaging as a problem of constrained multidimensional nonlinear optimization. *Magnetic Resonance in Medicine*, 8:16–24.
- [Duda and Hart, 1973] Duda, R. P. and Hart, P. E. (1973). *Pattern Classification and Scene Analysis*. John Wiley and Sons, New York.
- [Dufour et al., 1993] Dufour, I., Bittoun, J., Idy-Peretti, I., Jolivet, O., Darrasse, L., and Paola, R. D. (1993). Implementation and optimization by the simplex method of a 3d double echo sequence in steady-state free precession. *Magnetic Resonance Imaging*, 11:87–93.
- [Epstein et al., 1994] Epstein, F. H., III, J. P. M., and Brookeman, J. R. (1994). Optimization of parameter values for complex pulse sequences by simulated annealing: Application to 3d mp-rage imaging of the brain. *Magnetic Resonance in Medicine*, 31(2):164–177.

- [Farrar and Becker, 1971] Farrar, T. C. and Becker, E. D. (1971). *Pulse and Fourier Transform NMR Introduction to Theory and Methods. The Bloch Equations*. Academic Press, New York.
- [Fleischer et al., 1995] Fleischer, K., Laidlaw, D., Currin, B., and Barr, A. H. (1995). Cellular texture generation. *Proceedings of Siggraph '95, Los Angeles, CA*. to appear.
- [Foley et al., 1990] Foley, J. D., van Dam, A., Feiner, S. K., and Hughes, J. F. (1990). *Computer Graphics: Principles and Practices (2nd Edition)*. Addison Wesley.
- [Fox and Henson, 1986] Fox, R. A. and Henson, P. W. (1986). A general method for optimizing tissue discrimination in magnetic resonance imaging. *Medical Physics*, 13(5):635–643.
- [Galyean and Hughes, 1991] Galyean, T. A. and Hughes, J. F. (1991). Sculpting: An interactive volumetric modeling technique. In Sederberg, T. W., editor, *Computer Graphics (SIGGRAPH '91 Proceedings)*, volume 25, pages 267–274.
- [Ghosh et al., 1995] Ghosh, P. R., Laidlaw, D. H., Fleischer, K. W., Barr, A. H., and Jacobs, R. E. (1995). Pure phase-encoded mri and classification of solids. *IEEE Transactions on Medical Imaging*, 14(3). (in press).
- [Gravina and Cory, 1994] Gravina, S. and Cory, D. G. (1994). Sensitivity and resolution of constant-time imaging. *J. Magn. Reson., Series B*, 104:53–61.
- [Hendrick et al., 1984] Hendrick, R. E., Nelson, T. R., and Hendee, W. R. (1984). Optimizing tissue contrast in magnetic resonance imaging. *Magnetic Resonance Imaging*, 2:193–204.
- [Kajiya, 1986] Kajiya, J. T. (1986). The rendering equation. In Evans, D. C. and Athay, R. J., editors, *Computer Graphics (SIGGRAPH '86 Proceedings)*, volume 20, pages 143–150.
- [Kanal and Wehrli, 1986] Kanal, E. and Wehrli, F. (1986). *Principles, Methodology and Applications of Biomedical Magnetic Resonance Imaging*, chapter 2. VCH Publishers.
- [Laidlaw, 1992a] Laidlaw, D. H. (1992a). Material classification of magnetic resonance volume data. Technical Report CS-TR-92-21, Caltech.

- [Laidlaw, 1992b] Laidlaw, D. H. (1992b). Tissue classification of magnetic resonance volume data. Master's project, California Institute of Technology.
- [Levoy, 1988] Levoy, M. (1988). Display of surfaces from volume data. *IEEE Computer Graphics and Applications*, 8(3):29–37.
- [Loredo, 1989] Loredo, T. J. (1989). From laplace to supernova sn1987a: Bayesian inference in astrophysics. In Fougere, P., editor, *Maximum Entropy and Bayesian Methods*. Kluwer Academic Publishers, Denmark.
- [Lorensen and Cline, 1987] Lorensen, W. E. and Cline, H. E. (1987). Marching cubes: A high resolution 3D surface construction algorithm. In Stone, M. C., editor, *Computer Graphics (SIGGRAPH '87 Proceedings)*, volume 21, pages 163–169.
- [Mitchell et al., 1984] Mitchell, M. R., Conturo, T. E., Gruber, T. J., and Jones, J. P. (1984). Two computer models for selection of optimal magnetic resonance imaging (mri) pulse sequence timing. *Investigative Radiology*, 19(5).
- [Moore, 1979] Moore, R. E. (1979). *Methods and Applications of Interval Analysis*. SIAM, Philadelphia, Pennsylvania.
- [NAG, 1993] NAG (1993). *NAG Fortran Library*. Numerical Algorithms Group, 1400 Opus Place, Suite 200, Downers Grove, Illinois 60515.
- [Oppenheim et al., 1983] Oppenheim, A. V., Willsky, A. S., and Young, I. T. (1983). *Signals and Systems*. Prentice-Hall, Inc., New Jersey.
- [Pelc, 1993] Pelc, N. J. (1993). Optimization of flip angle for t1 dependent contrast in mri. *Magnetic Resonance in Medicine*, 29(5):695–699.
- [Platt and Barr, 1988] Platt, J. C. and Barr, A. H. (1988). Constraint methods for flexible models. In Dill, J., editor, *Computer Graphics (SIGGRAPH '88 Proceedings)*, volume 22, pages 279–288.



- [Press et al., 1992] Press, W. H., Teukolsky, S. A., Vetterling, W. T., and Flannery, B. P. (1992). *Numerical Recipes in C: The Art of Scientific Computing*. Cambridge University Press, New York, New York, second edition.
- [Rosen et al., 1984] Rosen, B. R., Pykett, I. L., and Brady, T. J. (1984). Spin lattice relaxation time measurements in two-dimensional nuclear magnetic resonance imaging: Corrections for plane selection and pulse sequence. *Journal of Computer Assisted Tomography*, 8(6):195–199.
- [Sabella, 1988] Sabella, P. (1988). A rendering algorithm for visualizing 3D scalar fields. In Dill, J., editor, *Computer Graphics (SIGGRAPH '88 Proceedings)*, volume 22, pages 51–58.
- [Sederberg and Parry, 1986] Sederberg, T. W. and Parry, S. R. (1986). Free-form deformation of solid geometric models. In Evans, D. C. and Athay, R. J., editors, *Computer Graphics (SIGGRAPH '86 Proceedings)*, volume 20, pages 151–160.
- [Snyder, 1992] Snyder, J. M. (1992). Interval analysis for computer graphics. In Catmull, E. E., editor, *Computer Graphics (SIGGRAPH '92 Proceedings)*, volume 26, pages 121–130.
- [True and Hughes, 1992] True, T. J. and Hughes, J. F. (1992). Volume warping. In *Proceedings Visualization '92*, pages 308–315. IEEE Computer Society Press.
- [Turk and Levoy, 1994] Turk, G. and Levoy, M. (1994). Zippered polygon meshes from range images. In Glassner, A., editor, *Proceedings of SIGGRAPH '94 (Orlando, Florida, July 24–29, 1994)*, Computer Graphics Proceedings, Annual Conference Series, pages 311–318. ACM SIGGRAPH, ACM Press. ISBN 0-89791-667-0.
- [Upson et al., 1989] Upson, C., Faulhaber, Jr., T., Kamins, D., Laidlaw, D., Schlegel, D., Vroom, J., Gurwitz, R., and van Dam, A. (1989). The application visualization system: A computational environment for scientific visualization. *IEEE Computer Graphics and Applications*, 9(4):30–42.
- [Upson and Keeler, 1988] Upson, C. and Keeler, M. (1988). VBUFFER: Visible volume rendering. In Dill, J., editor, *Computer Graphics (SIGGRAPH '88 Proceedings)*, volume 22, pages 59–64.

- [Vannier et al., 1985] Vannier, M. W., Butterfield, R. L., Jordan, D., Murphy, W. A., Levitt, R. G., and Gado, M. (1985). Multispectral analysis of magnetic resonance images. *Radiology*, 154:221–224.
- [Vannier et al., 1988] Vannier, M. W., Speidel, C. M., and Rickman, D. L. (1988). Magnetic resonance imaging multispectral tissue classification. In *Proc. Neural Information Processing Systems (NIPS)*.
- [Weil, 1986] Weil, J. (1986). The synthesis of cloth objects. In Evans, D. C. and Athay, R. J., editors, *Computer Graphics (SIGGRAPH '86 Proceedings)*, volume 20, pages 49–54.